UNIVERSITÁ DEGLI STUDI DI TRIESTE

XXVI CICLO DEL DOTTORATO DI RICERCA IN FISICA

The mass distribution in galaxy clusters from their internal dynamics

SETTORE SCIENTIFICO-DISCIPLINARE: FIS/05

Coordinatore:
PROF. PAOLO CAMERINI

Dottorando:
EMILIANO MUNARI

Supervisore:
DR. ANDREA BIVIANO

Co-Supervisore:
PROF. STEFANO BORGANI

Anno Accademico 2012/13

E lo stupore nei tuoi occhi
salí dalle tue mani
che vuote intorno alle sue spalle,
si colmarono ai fianchi
della forma precisa
d'una vita recente,
di quel segreto che si svela
quando lievita il ventre.

Fabrizio De André

Contents

1

Introduction

In the last two decades a self–consistent theoretical description of the Universe has been established. It describes the Universe by means of a relatively small number of parameters: $\Omega_m, \Omega_\Lambda, w(z), \Omega_k, \sigma_8, h, n_s$. This scenario relies on the assumption of the existence of two components whose nature is still totally unknown. In fact the last results by Planck (Planck Collaboration et al., 2013) confirm that $\sim 70\%$ of the overall mass–energy content is in the form of *Dark Energy*. This energy causes the Universe to expand accelerating at the present time. A deep revision of physics laws may be needed to explain the origin of the dark energy, making this issue one of the most interesting in modern physics. Another $\sim 25\%$ is in the form of non baryonic *Dark Matter* (DM hereafter), that interacts gravitationally but does not absorb or emit light.

Galaxy clusters are a source of information that can be used to shed light on these issues. Clusters are the largest virialized objects in the Universe, a collection of dark and baryonic matter gathered in galaxies or as a diffuse component. The number and mass of galaxy clusters has been demonstrated to be a powerful tool to constrain the cosmological parameters that describe our Universe (e.g. Allen et al., 2011). A crucial aspect in the cosmological application of galaxy clusters concerns the reliability of mass estimates. Mass is not a directly observable quantity but can be inferred in several ways, e.g. by assuming the condition of equilibrium of the intracluster plasma (e.g. Ettori et al., 2002a) or galaxies (e.g. Katgert et al., 2004) within the cluster potential well, or by measuring the gravitational lensing distortion of the images of background galaxies by the cluster gravitational field (e.g. Hoekstra, 2003, 2013).

These methods of mass measurement can only be applied to clusters for which a substantial amount of high quality data is available (like, e.g., in the clusters observed in the ongoing CLASH-VLT project, Postman et al., 2012; Biviano et al., 2013). When these are not available, it is still possible to infer cluster mass from other observed quantities, the so-called mass proxies, which are at the same time relatively easy to measure and characterised by tight scaling relations with cluster mass (e.g. Kravtsov and Borgani, 2012). The proxy that is considered in this Thesis is the velocity dispersion of member galaxies. In fact, the potential well of the cluster is the main driver of the orbital motion of the galaxies which, in the absence of mutual interactions, can be treated as test particles in the gravitational potential of the cluster. Therefore the kinematics of galaxies carries the information about the mass content of the cluster. The use of velocity dispersion as a proxy for cluster mass is particularly interesting in view of ongoing (BOSS, White et al., 2011) and future (Euclid, see Laureijs et al., 2011) large field galaxy surveys, in which thousands of clusters will be discovered, but each one with limited spectroscopic information only. The relation between such proxy and the mass must be calibrated and the systematic effects well understood. For this purpose numerical simulations are a powerful tool, which is exploited in the work presented in this Thesis.

Along with the cluster mass estimates, the dynamics of member galaxies provides important information on the build–up of galaxy clusters. In the very early Universe the cosmological inflation sets small initial density fluctuations resulting from Gaussian quantum fluctuations in a scalar field. In the hierarchical scenario of structure formation such fluctuations grow by gravitational instability. Structures form via merging of smaller systems, and the signature of the infall process is imprinted in the structure and dynamics of these objects. The dynamics is, however, influenced also by other processes, e.g. dynamical friction or ram pressure. In order to understand how clusters are assembled and how galaxies trace their internal dynamics, these processes must be taken into account, and their effect well understood.

In the late 90s, the mass density profile of galaxy clusters was found to be of a universal parametric shape for all such objects, the so–called NFW profile (Navarro et al., 1996). This universality might be due to a fundamental process still to be understood. On the other hand, with the advent of numerical simulations with increasingly higher resolution, such universality has been questioned, and a new quantity has been proposed as candidate for being a *universal profile*: the pseudo phase space density (Taylor and Navarro, 2001) (PPSD hereafter), although some doubts on its universality have been also raised (Ludlow et al., 2011). A direct comparison with real clusters might shed light on this issue, suggesting new

directions for theoretical studies.

The aim of this Thesis is to understand how clusters can be used as tracers of the past history of cosmic structure formation and which are the physical processes which determine their internal structure and dynamics. This objective is pursued by following three lines of attack, which combine the exploitation of both numerical simulations and observational data: a) study of the influence of the baryonic physics implemented in simulations and choice of the tracer of the gravitational potential in the scaling relation linking the velocity dispersion of cluster member galaxies and the cluster mass; b) derivation of the mass and velocity anisotropy profiles of a real, observed cluster; c) study of the pseudo phase space density profile of a real cluster and comparison with theoretical predictions. More in detail, the Thesis is structured as follows:

Chapter 2 provides an overview on the formation of cosmic structures. After discussing the statistical tools used to study the evolution of the Universe, the linear regime of the structure growth is presented. When this regime is not applicable anymore, the approaches to study the mildly non linear and fully non linear regimes are discussed. Numerical simulations are a powerful tool for studying the non linear regime and an overview on the main aspects of this kind of tool is presented in the final part of this chapter.

Chapter 3 presents the theoretical framework describing the dynamics of collapsed structures made of collisionless matter and the mechanisms through which equilibrium is established in such systems. A way to characterize the dynamical state of collapsed halos is by means of the so–called *pseudo phase–space density*. The properties of this quantity are still matter of discussion in the scientific community, and a review of the literature relevant for this subject is presented. The information carried by the internal dynamics of galaxy clusters, presented in the first part of this chapter, is used to infer the mass content of such systems. In particular, three methods are presented: the Dispersion–Kurtosis, MAMPOSSt, and the Caustic techniques.

Chapter 4 presents an overview of observations of galaxy clusters. The first step of an observational study consists in the detection of clusters. The main techniques for the detection in optical bands are presented. Once clusters are identified, it is possible to study the mass distribution of these objects. The main techniques for this purpose are based on gravitational lensing studies, on observations of the hot intra–cluster plasma through its X–ray emission or through the Sunyaev–Zeldovich (e.g., Carlstrom et al., 2002) effect. The use of

the kinematics of galaxy members is not discussed here as it is presented in more detail in chapter 3, being the main topic of this Thesis. These techniques are presented and compared to each other. When these techniques are not applicable, the use of proxies for the mass becomes a fundamental tool, and the description of the most commonly used proxies for the mass are presented. In the second part of this chapter, the properties of the population of cluster galaxies are discussed, along with the environmental processes determining its evolution.

Chapter 5 presents the results of a dynamical analysis of Abell 2142, a galaxy cluster at $z = 0.09$. Different methods are applied to derive the mass profile of this system by means of the information provided by the line–of–sight velocities of member galaxies. The velocity anisotropy profiles are obtained through the inversion of the Jeans equation, after assuming a mass profile obtained by combining results from the kinematics and the results coming from weak lensing and X-ray analyses. With these results it is possible to investigate the pseudo phase space density of this system, comparing it with theoretical predictions. We find an excellent agreement between our estimate of the PPSD profile and the theoretical relation, when using the sample made of red galaxies. The sample made of blue galaxies does not provide an agreement as good as the red sample's one. This is consistent with the scenario of blue galaxies being recently accreted and not having undergone violent relaxation yet. I discuss the possible reasons for the deviations from theoretical relations, highlighting the importance of baryonic physics still lacking in theoretical studies. The results obtained in this chapter are presented in Munari et al. (2013b).

Chapter 6 presents the results of an analysis of cosmological N-body and hydrodynamical simulations of galaxy clusters, aimed at calibrating the scaling relation between the internal velocity dispersion of clusters and their mass. In particular we have investigated the role of the baryonic physics implemented in the simulations used for such calibration, and how the choice of the tracers of the gravitational potential affects the scaling relation. In order to test and quantify the impact of the baryonic physics we made use of four sets of cosmological simulations: one DM-only simulation, one with non-radiative gas, and another two with gas cooling, star formation and galactic ejecta triggered by SN winds, one of the two also including the effect of AGN feedback. We determined the relation between the 1D velocity dispersion σ_{1D} and the

virial mass M_{200} of clusters when using as tracers DM particles, subhalos, and galaxies in cluster- and group-sized halos. This relation appears to be slightly different, according to the tracer and the baryonic physics implemented. We provide an interpretation of these differences, based on the role played by dynamical processes taking place in clusters, namely dynamical friction and tidal stripping. This study has been performed by considering the entire 6D phase space. Observationally it is possible to access to only three dimensions of the phase space, namely two for the position of a source in the plane of the sky and one for the line–of–sight velocity. The results of this study show that good knowledge of the $\sigma_{1D} - M_{200}$ relation in 6D phase space is fundamental before one could apply this relation to observational samples applying the corrections for the projection effects. The results obtained in this chapter are presented in Munari et al. (2013a)

Chapter 7 is the conclusion chapter, where I summarize the results presented in the Thesis, and discuss possible future directions of development.

2

The formation of cosmic structures

The WMAP[1] and Planck[2] missions (Komatsu et al., 2011; Planck collaboration et al., 2013), have shown a $\sim$ 400000 year young Universe. The cosmic microwave background appears on average homogeneous with small fluctuations of the order of $\Delta T/T \sim 10^{-5}$. This picture reflects the distribution of matter of the primordial Universe. The observed homogeneity and isotropy lead to the so–called *Cosmological Principle*, stating that the Universe looks the same in all directions. This implies that our location in the Universe is typical, not different in any fundamental way from any other.

However, the Universe we observe nowadays at small scales is highly inhomogeneous. How did stars, galaxies and clusters of galaxies form starting from the initial homogeneous conditions? The standard cosmological scenario describes the evolution of the small initial density fluctuations, that are set by the cosmological inflation occurred in the very early Universe, as a result of Gaussian quantum fluctuations in a scalar field. If $\rho(\vec{x})$ is a density field on average homogeneous and isotropic, small perturbations $\delta\rho(\vec{x})$ create instabilities that can grow as time goes by. We can build a toy model to estimate the time scales on which the dynamical processes occur. Let us consider a fluid that undergoes only its own gravity, and focus on a spherical region having radius λ. In this region let the density of the fluid be slightly greater than the average density of the fluid ρ. Because of gravity such fluctuation $\delta\rho/\rho$ grows. Pressure forces will oppose to the gravitational

[1] http://map.gsfc.nasa.gov/

[2] http://www.esa.int/Our_Activities/Space_Science/Planck

collapse. Instability, and therefore collapse, will occur if the gravitational force per mass unit F_g is greater than the pressure force per mass unit F_p, that is:

$$F_g \simeq \frac{GM}{\lambda^2} \simeq \frac{G\rho\lambda^3}{\lambda^2} > F_p \simeq \frac{p\lambda^2}{\rho\lambda^3} \simeq \frac{v_s^2}{\lambda} \tag{2.1}$$

where v_s is the sound velocity in the medium and p the pressure. The scale on which the collapse will take place is roughly

$$\lambda > \lambda_J = \frac{v_s}{(G\rho)^{1/2}} \tag{2.2}$$

where λ_J is called *Jeans length*. We can define the *dynamical time*

$$t_{dyn} = (G\rho)^{-1/2} \tag{2.3}$$

as the time a test particle takes to reach the center of an homogeneous mass distribution, subject to the gravitational force only. Equation 2.2 can be also read as follows: the system is unstable on a scale λ if the dynamical time is smaller than the time a sound wave takes to travel such a distance ($t_s \simeq \lambda / v_s$). This means that pressure is not able to set off against gravitational collapse.

Despite its simplicity, this model gives a first qualitative idea of the collapse process. A more detailed analysis is the topic of this chapter. The tools for studying the fluctuations and the first phase of the collapse, the so–called *linear regime*, are presented. The limitations of the linear regime are shown as well as a brief overview of the techniques to deal with the non–linear phase of the structure formation.

We address the reader to more comprehensive books for a detailed treatment of the topics discussed in next sections Binney and Tremaine (1987, 2011); Mo et al. (2010).

2.1 The Newtonian approximation

The overall Universe can be described by means of general relativity. In particular, the *Robertson – Walker* metric provides us with the description of the space-time of the Universe:

$$ds^2 = (c\ dt)^2 - a(t)^2 \left[\frac{dr^2}{1 - Kr^2} + r^2(d\theta^2 + sin^2\theta d\varphi^2) \right] \tag{2.4}$$

where K is the curvature parameter, $a(t)$ is the expansion factor and (r, θ, ϕ) are the spherical coordinates. The time dependence of the spatial part of the metric has been factorized in the latter term.

The Birkhoff theorem states that spherically symmetric gravitational field in an empty space is static and described by the Schwarzschild metric, that is the metric generated by a mass point in the empty space.

$$ds^2 = \left(1 - \frac{r_0}{r}\right)(c\ dt)^2 - \left[\frac{dr^2}{1 - \frac{r^2}{r_0^2}} + r^2(d\theta^2 + sin^2\theta d\varphi^2)\right] \tag{2.5}$$

with $r_0 = 2GM/c^2$. Let us consider a spheric homogeneous mass–energy distribution at the center of an empty cavity. Even if such distribution is not static, the metric in the empty region will be static. Therefore, provided that the spherical symmetry is maintained, the external and the internal regions do not interact. Let the internal distribution be a sphere with mass m and radius l. If l is such that $\frac{Gm}{lc^2} \ll 1$ then the metric will tend to the Minkowski metric, and if the velocities are much smaller than c it is possible to use the Newtonian mechanics.

Since $M \sim \rho l^3$, the Newtonian approximation holds on a scale $l \ll c \cdot (G\rho)^{-1/2}$. From the first Friedmann's equation we obtain $(G\rho)^{-1/2} \sim H$, where $H = \dot{a}/a$ is the Hubble parameter, hence the above mentioned scale is $l \ll \frac{c}{H} \simeq R_H$. This means that inside the horizon the Newtonian approximation holds.

The Birkhoff theorem is still valid if the empty region is substituted with a mass–density distribution having a smaller density than the inner sphere and the background.

2.2 The statistics of the density field

Let $\rho(\vec{x})$ be the density field of the Universe and $\overline{\rho}$ its mean density. The *density contrast* is defined as follows:

$$\delta(\vec{x}) = \frac{\rho(\vec{x}) - \overline{\rho}}{\overline{\rho}} \tag{2.6}$$

The density contrast can be recast in the following way:

$$\delta(\vec{x}) = \frac{V}{(2\pi)^3} \int \hat{\delta}_{\vec{k}} e^{i\vec{k}\cdot\vec{x}} d^3k \tag{2.7}$$

where $\hat{\delta}_{\vec{k}}$ are the Fourier coefficients and V is the volume within which the Universe can be considered periodic. Changing such volume results in different Fourier coefficients, hence a different realization of the Universe. Therefore a cosmological model can predict only statistical properties of the fields. Such properties must be thought as the probability of having a particular realization of the Universe given the cosmological model. A cosmological model therefore provides us with an *ensemble* of models, at odds with the unique realization that can be observed in reality. The *Ergodic Principle* allows to overcome this issue, as it states that the mean over the ensembles translates into a spatial mean on portions of Universe.

2.2.1 The power spectrum

Although the mean value of $\delta(\vec{x})$ is null, so is not the variance:

$$\sigma^2 \equiv \langle \delta^2 \rangle = \sum_{\vec{k}} \langle |\delta_{\vec{k}}|^2 \rangle = \frac{1}{V} \sum_{\vec{k}} \delta_{\vec{k}}^2 \tag{2.8}$$

where the mean is performed on an ensemble of realizations. Taking the limit $V \to \infty$ and assuming the density field to be statistically homogeneous and isotropic (in this way there is no dependence on the direction of $\vec{k}$ but only on its module $k = |\vec{k}|$), we obtain the following expression:

$$\sigma^2 \equiv \langle \delta^2 \rangle = \frac{1}{V} \sum_{\vec{k}} \delta_{\vec{k}}^2 \to \frac{1}{2\pi^2} \int_0^\infty P(k) k^2 dk \tag{2.9}$$

where, for the sake of simplicity, we define $P(k) = \delta_k^2 = |\delta_k|^2$. The quantity $P(k)$ is called *power spectrum*. It is worth noting that the variance does not have a spatial dependence, therefore σ^2 gives information only on the amplitude of perturbations.

The power spectrum is commonly parametrized with a power law:

$$P(k) = Ak^n \tag{2.10}$$

where n is called *spectral index*. The following conditions must be satisfied so as the integral of equation 2.9 converges:

$$n > -3 \qquad \text{for } k \to 0 \tag{2.11a}$$

$$n < -3 \qquad \text{for } k \to \infty \tag{2.11b}$$

2.2.2 Filtering scales

The variance as defined in the previous section is not an observable quantity. The scale R on which the measurement is performed must be specified. The fluctuation on such scale is

$$\delta_R(\vec{x}) = \delta_M(\vec{x}) = \int \delta(\vec{y}) W_R(|\vec{x} - \vec{y}|) d^3y \tag{2.12}$$

where W is a *window function* that depends on the shape of the considered volume. The variance then becomes

$$\boxed{\sigma_R^2 = \sigma_M^2 = \langle \delta_R^2 \rangle = \frac{1}{2\pi^2} \int k^2 P(k) \hat{W}_R^2(k) dk} \tag{2.13}$$

where $\hat{W}_R(k)$ is the Fourier transform of the window function. For dimensional reasons the following equivalence holds: $W_R(k) = W(kR)$. In case of $n > -3$, substituting the expression for the power spectrum $P(k)$ (equation (2.10)) in this equation returns a variance that is a decreasing function of radius. This means that the power of the fluctuations is greater on small scales. The latter therefore correspond to the first structures to become non linear. Small objects are the first to form, and successively the bigger ones form. This is the so-called *hierarchical scenario*.

2.3 Linear evolution of the density field

In this section we shall see how initially small perturbations of the density field evolve. As long as the perturbations are small ($\delta < 1$), their evolution can be studied in the linear approximation. The equations describing a self–gravitating fluid are:

$$\frac{\partial \rho}{\partial t} + \vec{\nabla}(\rho \vec{v}) = 0 \qquad \textit{Continuity Equation} \tag{2.14a}$$

$$\frac{\partial \vec{v}}{\partial t} + (\vec{v} \cdot \vec{\nabla})\vec{v} = -\frac{\vec{\nabla} p}{\rho} - \vec{\nabla}\phi \qquad \textit{Euler Equation} \tag{2.14b}$$

$$\nabla^2 \phi = 4\pi G \rho \qquad \textit{Poisson Equation} \tag{2.14c}$$

where p is the pressure, ϕ the gravitational potential and ρ the mass density. The continuity equation describes the conservation of mass, the Euler equation provides the relation between the acceleration of a fluid element and the forces (gravitational

and pressure) causing it and finally the Poisson equation specifies the Newtonian nature of the gravitational force. These equations can be recast in comoving coordinates, Fourier transformed and linearised, providing the following equation that describes the evolution of the density contrast of perturbations in an expanding background.

$$\ddot{\hat{\delta}}_{\vec{k}}(t) + 2H\dot{\hat{\delta}}_{\vec{k}}(t) + \left(\frac{v_s^2 k^2}{a^2} - 4\pi G\overline{\rho}\right)\hat{\delta}_{\vec{k}}(t) = 0 \tag{2.15}$$

with $v_s^2 = \partial P/\partial\rho$ and $\hat{\delta}_{\vec{k}}$ are the Fourier coefficients.

DM is the dominant component in mass in the Universe. The dynamics of the collapse of density perturbations and the following structure formation is therefore led by the behaviour of such component, which is non–collisional. If the pressure term in equation (2.15) is neglected we obtain the following relation:

$$\ddot{\hat{\delta}}_{\vec{k}}(t) + 2H\dot{\hat{\delta}}_{\vec{k}}(t) - 4\pi G\overline{\rho}\hat{\delta}_{\vec{k}}(t) = 0 \tag{2.16}$$

This equation shows an important property of the perturbation theory in linear regime: different Fourier modes evolve independently of one another. The *central limit theorem* states that an infinite number of independent modes generates a Gaussian field. Initially independent modes that evolve decoupled means that the perturbations keep being Gaussian.

It is possible to demonstrate that the solution to eq. (2.16) is made of a *growing mode* D_+ and a *decaying mode* D_-: $\hat{\delta}_{\vec{k}} = A_{\vec{k}}D_+(t) + B_{\vec{k}}D_-(t)$. The former leads to an increase in the density contrast and consequently to denser and denser objects. For a collisionless fluid in a Universe with $\Omega_m < 1$ and $\Omega_{DE} = 1 - \Omega_m$ like the ΛCDM one, the expression for the growing mode of perturbations is given by:

$$D_+(z) = E(z)G(z) \tag{2.17}$$

with

$$E(z) = \frac{H(z)}{H_0} = [\Omega_{0m}(1+z)^3 + \Omega_{0k}(1+z)^2 + \Omega_\Lambda]^{1/2} \tag{2.18}$$

$$G(z) = \frac{5}{2}\Omega_{0m}\int_z^{+\infty}\frac{1+z'}{E(z')^3}dz' \tag{2.19}$$

Note that this last equation does not hold for a dark energy model with equation of state $w \neq -1$. In Figure 2.1 the growth factor as a function of redshift for different cosmologies is shown.

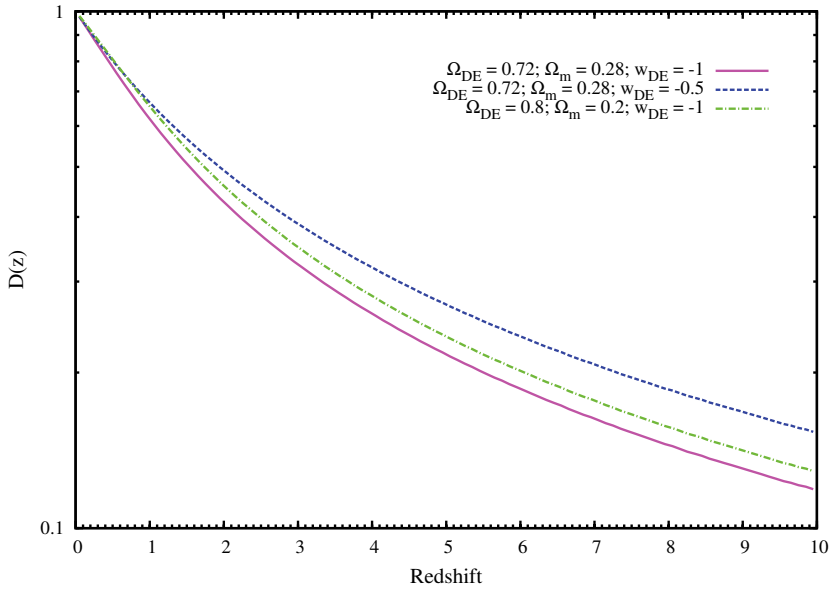

Figure 2.1: Different curves represent the growth factor $D_+(z)$ normalized at 1 for $z = 0$ for three different set of cosmological parameters, as indicated in the legend. [After Sartoris (2012)].

A matter dominated Universe can be described with an *Einstein – de Sitter* model, in which $\Omega_m = 1$ and $\Omega_\Lambda = 0$. In this case the following relations hold:

$$a(t) \sim t^{2/3} \quad ; \quad 4\pi G\bar{\rho} = \frac{2}{3t^2} \quad ; \quad H = \frac{2}{3t} \tag{2.20}$$

and the growing mode becomes

$$D_+(t) \sim t^{2/3} \sim a \tag{2.21}$$

This means that the density contrast increases, independently of the mode, at the same rate of the expansion of the Universe.

In more qualitative, but also more intuitive, way this result can be understood by considering the time scales on which the collapse process takes place. From the first Friedmann's equation we have

$$H^2 = \frac{8\pi G}{3}\bar{\rho} \sim t^{-2} \tag{2.22}$$

The characteristic time of the expansion, t_{exp}, will therefore be

$$t_{exp} \sim (G\overline{\rho})^{-1/2} \tag{2.23}$$

where $\overline{\rho}$ is the mean density of the Universe. In the linear regime the density of the perturbation is very close to the mean density of the Universe, therefore

$$\rho \simeq \overline{\rho} \quad \Longrightarrow \quad t_{dyn} \simeq t_{exp} \tag{2.24}$$

that means that the rate of growth of the perturbation is similar to the one of the expansion of the Universe.

As seen in Sect. 2.3, different modes of the perturbation field evolve independently one another, and the evolution is therefore a linear function of the initial conditions. The growing mode is expected to dominate after some time, and the resulting power spectrum at redshift z reads:

$$P(k,z) = T^2(k)D^2(z)P_{in}(k) \tag{2.25}$$

where $D(z)$ is given by eq. (2.17), $P_{in}(k)$ is the initial power spectrum described by $P(k) = Ak^n$, and T(k) is the *transfer function* (Eisenstein and Hu, 1998). Such function bears the imprint of evolutionary effects (*Meszaros effect, Silk damping, baryonic acoustic oscillations, neutrino free streaming*) that alter the original linear form of the initial power spectrum. In Figure 2.2 the transfer function for different models is shown.

2.4 The Zel'dovich approximation

In 1970, Zel'dovich developed a theory (Zel'dovich, 1970) to follow the formation of DM structures that strictly holds in a Universe dominated by Hot Dark Matter. Nevertheless, as long as we consider the phase in which the linear approximation holds, such theory can still be applied and gives us information on the overall distribution of the perturbations and the objects that will then form. This method has a Lagrangian approach, following the fluid elements along their trajectories.

Let d^3q be the initial volume of the fluid element (see Figure 2.3) and $\vec{q}$ its Lagrangian coordinate, that coincides with the Eulerian coordinate. This fluid element has density $\rho_0(\vec{q})$ and is moving (dashed line in the figure) changing shape, but still conserving its mass. Let the final volume and density be d^3r and $\rho(\vec{r},t)$, respectively. Without any perturbation the position vector would be $\vec{r}(t) = a(t) \cdot \vec{x}$,

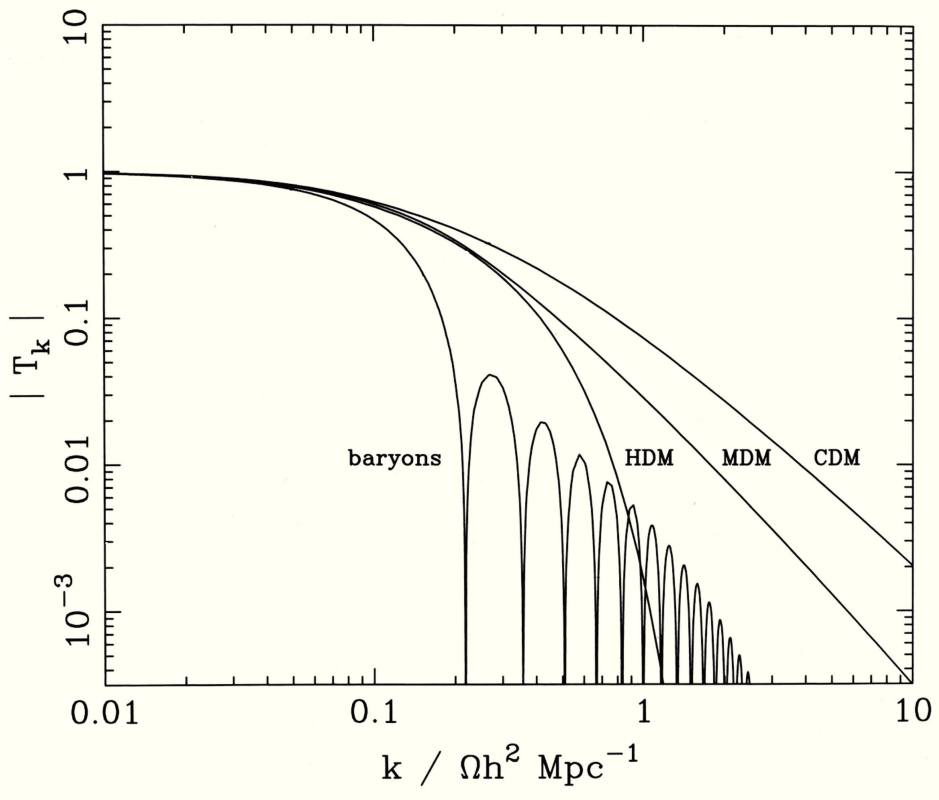

Figure 2.2: A plot of transfer functions for various models. A number of possible matter contents are illustrated: pure baryons, pure CDM, pure HDM, M(ixed)DM (30% HDM, 70% CDM). [Modified from Peacock (1999)].

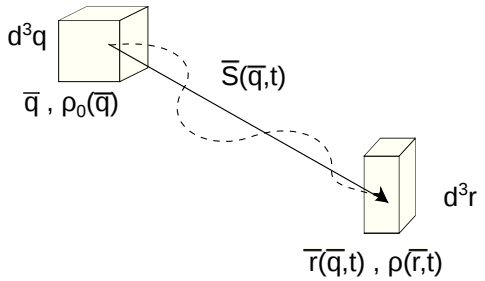

Figure 2.3: Lagrangian scheme of the Zel'dovich approximation.

with $\vec{x}$ being the comoving coordinate. Because of the perturbations, the position vector takes the following form:

$$\vec{r}(\vec{q},t) = a(t)\cdot\vec{x}(\vec{q},t) = a(t)[\vec{q}+\vec{S}(\vec{q},t)] \tag{2.26}$$

The Zel'dovich theory is based on the following *ansaz*: for small displacements, the displacement vector $\vec{S}$ is factorizable in a term depending only on time and in one depending only on the position $\vec{q}$.

$$\vec{S}(\vec{q},t) = g(t)\cdot\vec{p}(\vec{q}) \tag{2.27}$$

By imposing the conservation of mass, we obtain the following equation:

$$\rho(\vec{x},t) = \frac{\rho_b}{det\left(\delta_{ij}+g(t)\frac{\partial p_j}{\partial q_i}\right)} \tag{2.28}$$

where $\rho_b = \rho/a^3$ is the background density. The density contrast in the Lagrangian theory reads as follows:

$$\delta(\vec{x},t) = \frac{\rho(\vec{x},t)}{\rho_b} - 1 \simeq \left[1 - g(t)\frac{\partial p_j}{\partial q_i}\right] - 1 = -g(t)\vec{\nabla}_q\vec{p} \tag{2.29}$$

while in Eulerian theory is:

$$\delta(\vec{x},t) = D(t)\delta_i(\vec{x}) = D(t)\sum_{\vec{k}}\hat{\delta}_{\vec{k},i}\exp[i\vec{k}\cdot(\vec{q}+g(t_i)\vec{p}(\vec{q}))] = D(t)\sum_{\vec{k}}\hat{\delta}_{\vec{k},i}\exp[i\vec{k}\cdot\vec{q}] \tag{2.30}$$

By imposing that the evolution obtained with the Lagrangian and Eulerian descriptions must coincide, the following relations are obtained:

$$\begin{cases} g(t) \propto D(t) \\ \vec{\nabla}_q\vec{p} \propto \delta(\vec{q}) \end{cases} \tag{2.31}$$

and the displacement vector becomes

$$\vec{p}(\vec{q}) = \frac{D(t)}{g(t)}\sum_{\vec{k}}\frac{i\vec{k}}{k^2}\hat{\delta}_{\vec{k}}e^{i\vec{k}\cdot\vec{q}} \equiv -\vec{\nabla}\Phi_0 \tag{2.32}$$

It is possible to demonstrate that Φ_0 is proportional to the gravitational potential. By substituting this relation in (2.29) we obtain the Zel'dovich relation:

$$\boxed{\delta(\vec{x},t) = D(t)\nabla^2\Phi_0(\vec{q})} \tag{2.33}$$

The position vectors $\vec{q}$ and $\vec{x}$ are linked via the *Zel'dovich map*

$$\vec{x}(\vec{q},t) = \vec{q} + g(t)\vec{p}(\vec{q}) = \vec{q} - D(t)\vec{\nabla}\phi_0 \tag{2.34}$$

Deriving such relation we can compute the velocity at the time t_0:

$$\vec{v}_0 = a(t_0)\dot{D}(t_0)\vec{\nabla}\Phi_0 \tag{2.35}$$

that, substituted in equation (2.34) returns

$$\vec{x}(\vec{q},t) = \vec{q} + D(t)\frac{\vec{v}_0}{a(t_0)\dot{D}(t_0)} = \vec{q} + \vec{cost}\cdot D(t) \tag{2.36}$$

that resembles the equation of the linear motion $\vec{x} = \vec{q} + \vec{v}_0 \cdot t$. The Zel'dovich approximation consists in giving to a fluid element an acceleration proportional to the gradient of the potential in that position. The fluid element will move with linear motion with time variable $D(t)$, instead of t, because the background is expanding.

From this "pictorial" description it is easy to understand the limit of such approximation. The fluid elements feel the gravity only at the beginning, in fact the acceleration is proportional to Φ_0 and not to $\Phi(t)$. Therefore two elements instead of hitting one another, they pass through each other. This phenomenon is called *shell crossing*. When this happens the Zel'dovich map (equation (2.34)) is no longer univocal and the approximation is not applicable anymore.

A further refinement (Coles et al., 1993) in the theory consists in setting Fourier amplitudes of the density field equal to zero for all wavenumbers greater than k_{nl}, where k_{nl} marks the transition to the nonlinear regime. In fact, as we have seen, the Zel'dovich approximation works well at recovering the large scale structure, but it does not work on small scales where the highly non linear effects occur. This is the so–called *Truncated Zel'dovich Approximation*. A comparison between an exact N–body solution and the solution provided by both the Zel'dovich (ZA) and the truncated Zel'dovich (TZA) approximations starting from the same initial conditions is shown in Figure 2.4. It is possible to notice that the rough structure is recovered with the ZA, and even better with the TZE. In both cases, it is possible to recover the position of the formation of structures, but not their internal structure, as this is due to the highly non linear effects.

The theory developed by Zel'dovich allows to understand the first stages of structure formation. The matrix in equation (2.28) is real and symmetric, because

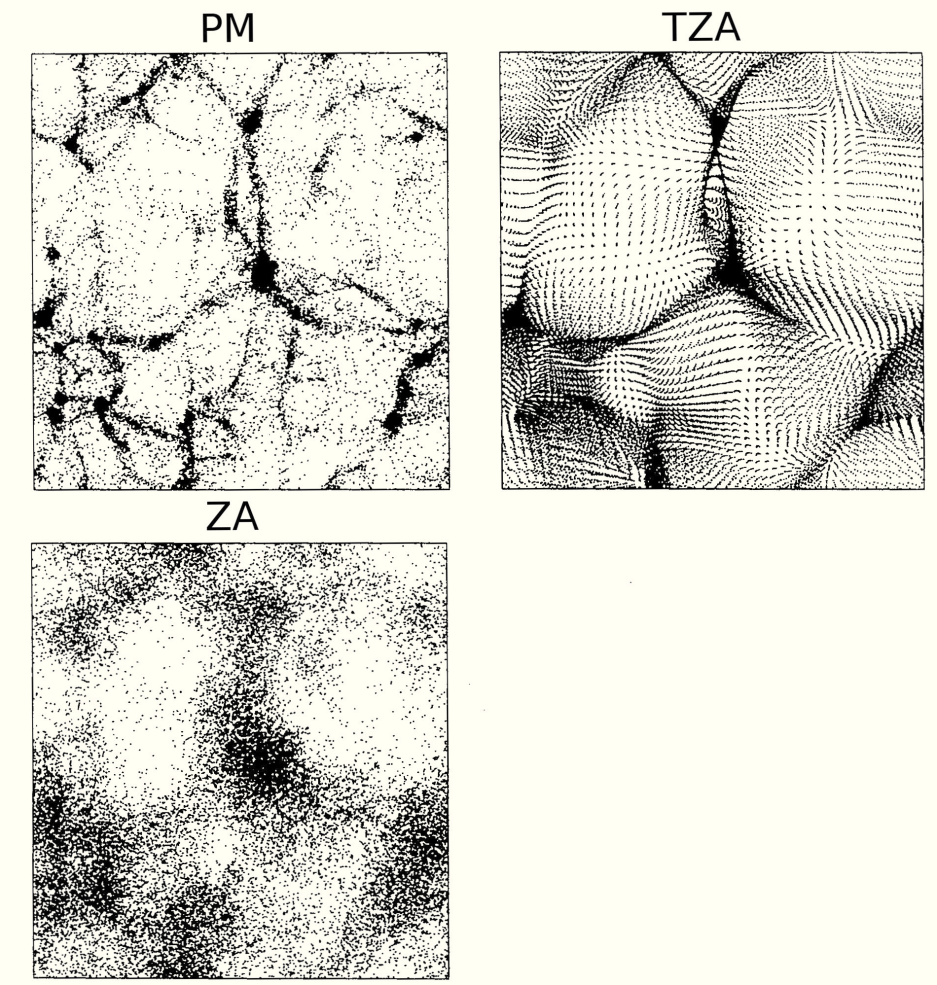

Figure 2.4: Structures simulated starting from the same initial comditions, using a PM algorithm (see Sect. 2.7.2) (*top left panel*), the Zel'dovich approximation (ZA - *bottom left panel*) and the truncated Zel'dovich approximation (TZA - *top right panel*). [Courtesy S. Borgani].

$\vec{p}(\vec{q})$ is the gradient of a scalar quantity. It is then possible to find a reference frame in which the matrix is diagonal. Let $-\lambda_1(\vec{q}), -\lambda_2(\vec{q}), -\lambda_3(\vec{q})$ be the three

eigenvalues, such that $\lambda_1 \geq \lambda_2 \geq \lambda_3$:

$$\rho(\vec{x}, t) = \frac{\rho_b(t)}{[1 - D(t)\lambda_1(\vec{q})] \cdot [1 - D(t)\lambda_2(\vec{q})] \cdot [1 - D(t)\lambda_3(\vec{q})]} \tag{2.37}$$

Assume that at an initial moment $D(t)\lambda_i \ll 1, \quad \forall i$. As time goes by $D(t)$ grows, and there will be a moment in which $D(t) = \lambda_1^{-1}$. The density field diverges, and the collapse happens in one direction, the one of the eigenvector corresponding to the eigenvalue λ_1. These sheet–like structures are called *pancakes*, and are the first non–linear structures to be formed. If the eigenvalues are such that $\lambda_1 = \lambda_2$ the collapse takes place in two perpendicular directions and the resulting structure is called *filament*. Finally if the three eigenvalues are equal the collapse takes place in three dimension, and a point–like structure is formed.

When the collapse takes place, regions where the density diverges are formed. These regions are called *caustics*. But because of the shell–crossing issue, particles do not gather forming high density structures. The Zel'dovich theory is therefore able to reproduce the large wavelength structures, but is not able to catch the high frequency structures. This is the reason why it does not work properly in a CDM scenario, where the first structures that form are the small ones. Nevertheless, provided that one stops at the non linear regime, it allows to describe the general behaviour of the structure formation, identifying and locating the regions where matter is collapsing and, later on, clusters of galaxies will form.

2.5 The spherical collapse

So far we have dealt with small perturbations of the density field, for which the linear approximation could be applied. Such approximation allows to locate the high density regions where the cosmic structures nowadays we observe are going to form. As time goes by, the fluctuations grow in amplitude, with density contrasts that become much bigger than $\delta \simeq 1$. The linear approximation is no longer applicable and a more detailed analysis is required. An analytical approach is possible only for very simple and idealised systems, as first introduced by Gunn and Gott (1972). They described the assembly of the Coma cluster as bound shells of matter accreting onto a collapsed object.

For more complex objects, like the real cosmic structures we want to describe, we need to directly integrate the equations of motions of the DM fluid particles. This approach will be described in Sect. 2.7, where numerical simulations are described.

In this section we describe the collapse of a system that, although very idealised, provides us with information about the behaviour we expect too see in a real, more complex collapsed system, with high density contrast.

Consider a spheric perturbation of an initial density field, having constant density and a positive, although small, amplitude. Let t_i be this initial moment in a matter dominated Universe. The perturbation is expanding along with the Universe, therefore at the edges the peculiar velocity u_i will be null. Given the symmetry of the system, such fluctuation of the density field can be treated as a stand–alone Universe, that evolves according to its own cosmological model. A density parameter of the perturbation can be introduced:

$$\Omega_p(t_i) = \frac{\rho(t_i)(1+\delta(t_i))}{\rho_{cr}(t_i)} = \Omega(t_i)(1+\delta(t_i)) \tag{2.38}$$

where the subscript p denotes a quantity referred to the perturbation, and $\rho_{cr} = 3H^2(z)/8\pi G$ is the *critical density*. For a structure to form it is necessary that the perturbation detaches from the Hubble flow and collapses. This means that the perturbation must behave as a closed Universe:

$$\Omega_p(t_i) > 1 \tag{2.39}$$

Recalling the definition of the density parameter

$$\Omega(z) = \frac{\rho(z)}{\rho_{cr}(z)} = \frac{\rho(z)}{\frac{3H^2(z)}{8\pi G}} = \frac{\Omega_0(1+z)}{(1-\Omega_0)+\Omega_0(1+z)} \tag{2.40}$$

where Ω_0 is the present value of the density contrast, the condition $\Omega_p(t_i) > 1$ translates in a condition on the initial value of the density contrast. If such condition is satisfied, the perturbation grows as a separate Universe, reaching the maximum of the expansion at the time t_m and then collapses. The expansion is described by the Friedmann equation

$$\left(\frac{\dot{a}}{a_i}\right)^2 = H_i^2\left[\Omega_p(t_i)\frac{a_i}{a} + (1-\Omega_p(t_i))\right] \tag{2.41}$$

It is possible to demonstrate that for a closed Universe the following relation holds

$$t_m = \left(\frac{3\pi}{32G\rho_p(tm)}\right)^{1/2} \tag{2.42}$$

where $\rho_p(t_m)$ is the density of the perturbation at the moment of maximum expansion, and it can be derived by imposing $\dot{a}(t_m) = 0$. This moment is also the moment at which the perturbation detaches from the Hubble flow. From this moment the background keeps expanding while the perturbation collapses. Its final fate is not becoming a singularity. In a high density environment small anisotropies form pressure gradients and shocks. The gravitational energy is converted in thermal energy that heats the gas. If we consider a DM only system, instead of the pressure, not present since DM is non–collisional, the system is supported by velocity dispersion. The system reaches an equilibrium configuration, with a dimension R_{vir} and mass M described by the virial theorem (see Sect. 3.4):

$$E_{vir} = \frac{U}{2} = -\frac{1}{2}\frac{GM^2}{R_{vir}} \tag{2.43}$$

where U is the potential energy of the system. In order to obtain an estimate of the overdensity of the system at the virialization, let us impose that the system does not lose neither mass due to shocks nor energy because of radiation. The mass and the energy the perturbation had at the time t_m are equal at the time t_{vir}. From this we obtain the following relation:

$$R_{vir} = \frac{R_m}{2} \tag{2.44}$$

During the collapse of the perturbation the Universe has kept expanding, its density being $\rho \simeq a^{-3} \simeq t^{-2}$. The density contrast at the virialization therefore is

$$\delta(t_{vir}) = \frac{\rho_p(t_{vir})}{\rho(t_{vir})} = \frac{2^3\rho_p(t_m)}{\rho(t_m)\left(\frac{t_{vir}}{t_m}\right)^{-2}} \simeq 178 \tag{2.45}$$

A generalization of this relation has been derived in Bryan and Norman (1998), still in an idealised case of a spherically symmetric DM only system:

$$\delta(t_{vir}) = 18\pi^2 + 82x - 39x^2 \tag{2.46}$$

where $x = \Omega_m(t_{vir}) - 1$. At $z = 0$ it is $\delta(t_{vir}) \simeq 100$, reaching asymptotically the value 178 for high redshifts.

It is worth noting that the density contrast predicted by the linear theory is

$$\delta(t_{vir}) = \delta(t_m)\left(\frac{t_{vir}}{t_m}\right)^{2/3} = 1.69 \tag{2.47}$$

where $\delta(t_m)$ has been extrapolated according to the linear theory and has a value $\simeq 1$. It appears clear that as soon as the density contrast is comparable to the unity the linear theory is no longer applicable.

In Figure 2.5 the critical threshold for collapse and the virial density of collapsed objects as a function of the matter density parameter are shown.

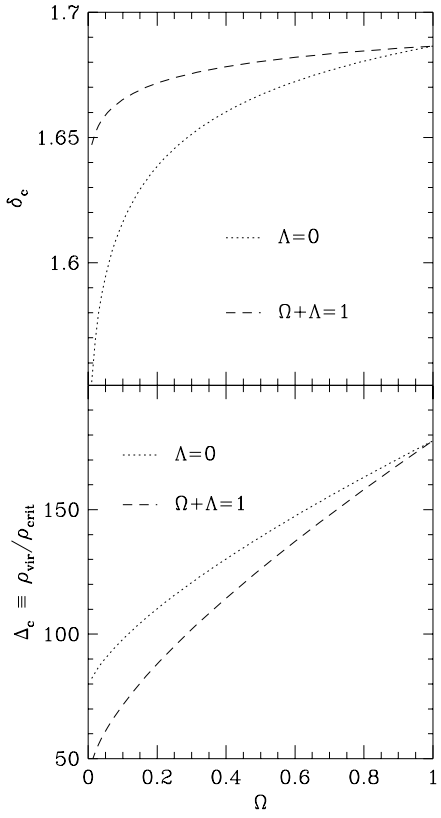

Figure 2.5: *Upper panel:* critical threshold for collapse, δ_c, as a function of the matter density parameter Ω. *Lower panel:* virial density of collapsed objects in units of critical density. [After Eke et al. (1996)].

2.6 The mass function

The scenario so far painted consists of a Universe made of (cold) DM particles that gather together in a hierarchical fashion, giving rise to cosmological structures. This picture, although it is a simplification of the real Universe as it is lacking the baryonic physics, is able to provide us with an estimate of the number of cosmological objects of a given mass at a given redshift, an information that can be compared with observation, allowing us to test the theoretical framework. In fact it is possible to derive a relation that describes the number of DM halos of a given mass present in the Universe at a certain time. This is the so-called *mass function*. The number of such halos strongly depends on the history of the Universe, in particular on the rate of the assembly of DM structures. Therefore the mass function is strongly related to the cosmological parameters describing the evolution of the Universe.

We now derive the analytical expression for the mass function using the approach adopted by Press and Schechter (1974) (PS hereafter). The number N of objects per unit volume with mass between M and $M + dM$ is $dN = n(M)dM$, where $n(M)$ is the mass function. In the PS approach, the fraction of matter that will form objects with mass at least M is assumed to be given by the portion of the initial density field, smoothed on the mass scale M, lying at an overdensity exceeding a given critical threshold value, δ_c. If the density field is assumed to be Gaussian, the probability that at some point the linearly evolved smoothed field δ_M exceeds the critical density contrast δ_c is given by:

$$p_{>\delta_c}(M,z) = \frac{1}{\sqrt{2\pi}\sigma_M(z)} \int_{\delta_c}^{\infty} exp\left(-\frac{\delta_M^2}{2\sigma_M(z)^2}\right) d\delta_M \tag{2.48}$$

The time dependence enters through the variance σ_M at the mass scale M linearly extrapolated at redshift z.

Notice that if we take the limit $M \to 0$ (this means considering objects of any mass) then the probability $p_{>\delta_c}(M,z)$ should be 1. The integral of eq. 2.48 returns instead the value $1/2$. By the PS approach, in fact, a point with $\delta_M < \delta_c$, for a given filtering mass scale M has zero probability to reach $\delta_{M'} > \delta_c$ for some larger filtering scale $M' > M$. This means that the PS approach neglects the possibility for that point to end up in a collapsed halo of larger mass. A proper derivation of the mass function accounting for the missing factor 2 is provided in Bond et al. (1991).

Since Eq. 2.48 provides the fraction of volume in objects of a given mass, the number density of such objects will be obtained by dividing it by the Lagrangian

volume occupied by each object. Taking into account also the missing factor 2, the PS mass function is as follows:

$$\begin{aligned}\frac{dn(M,z)}{dM} &= \frac{2}{V_M}\frac{\partial p_{>\delta_c}(M,z)}{\partial M} = \\ &= \sqrt{\frac{2}{\pi}}\frac{\bar{\rho}}{M^2}\frac{\delta_c}{\sigma_M(z)}\left|\frac{d\log\sigma_M(z)}{d\log M}\right|\exp\left(-\frac{\delta_c^2}{2\sigma_M(z)^2}\right)\end{aligned} \tag{2.49}$$

From this expression it is possible to understand how the mass function can be used to constrain cosmological parameters. If we restrict to massive objects only, the mass function is dominated by the exponential term. This means that it is exponentially sensitive to the cosmological parameters. The latter $(\Omega_m, \Omega_\Lambda, w(z), \Omega_k, \sigma_8, h, n_s)$ enter the mass function through σ_M (eq. (2.9)), which depends on the power spectrum (eq. (2.25)), and on the linear perturbation growth factor (eq. (2.17)). Fig. 2.6 shows to plots illustrating the sensitivity of the cluster mass function to redshift and cosmological models.

In the potential wells of the halos, galaxies and clusters of galaxies form. Counting such objects provides tight constraints on cosmological parameters.

With the advent of N-body numerical simulations, that cover a wide dynamical range, more precise expressions for the mass function have been computed but still preserving the meaning and the power in constraining cosmological parameters. Of course the mass function strongly depends on how the cluster mass is defined in simulations. The most commonly used definition is the spherical overdensity one. The mass is considered to be the amount of matter within a spherical region of a virialized halo having a mean density Δ_c times the critical density, as described in Sect. 2.5. Sheth and Tormen (1999) calibrated the mass function using the simulations and Sheth et al. (2001) generalized the expression of the Press–Schechter mass function by considering a more physically realistic ellipsoidal collapse model.

A different approach is adopted in Jenkins et al. (2001), where a functional form of the mass function is obtained as the best fit to the results of a combination of different simulations.

Recently, many authors have focused on the redshift evolution (see,e.g. Reed et al., 2003, 2007; Lukić et al., 2007; Cohn and White, 2008; Tinker et al., 2008) and the impact of baryonic physics (Stanek et al., 2009; Cui et al., 2012).

Since mass is not a directly observable quantity, the mass of galaxy clusters must be inferred from the observations of other quantities. A statistical method, that is discussed in Chapter 6, for obtaining the mass distribution of a sample of clusters is the application of a scaling relation between the velocity dispersion

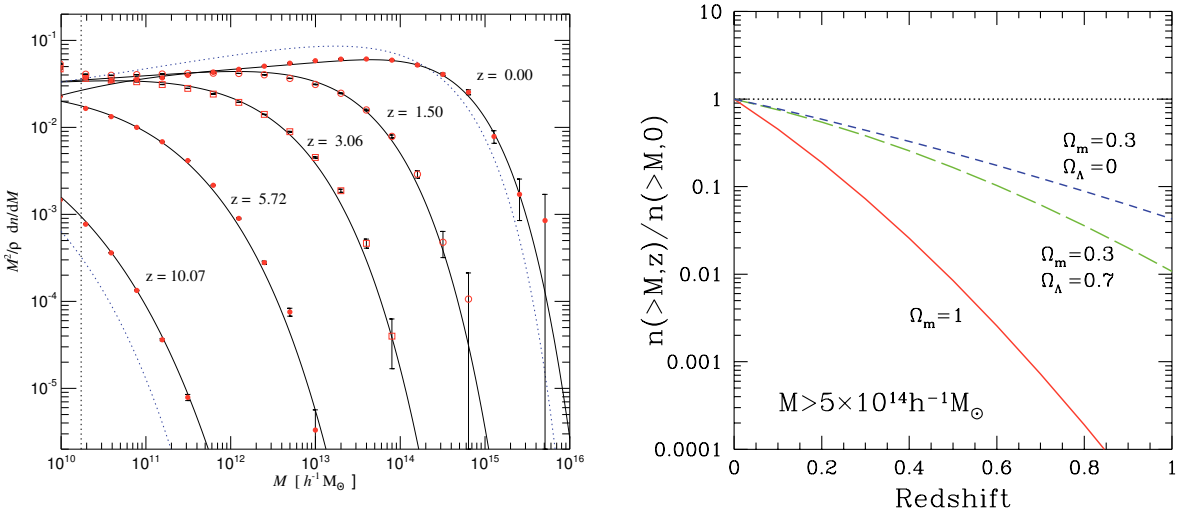

Figure 2.6: The sensitivity of the cluster mass function to redshift and cosmological models. *Left panel:* dots with errorbars identify the halo mass function at different redshift as obtained from the Millennium Run (Springel et al., 2005b), while the black solid and blue dotted lines are the predictions by Henry (2004) and Press and Schechter (1974). *Right panel:* evolution of the cluster mass function for $M > 5 \times 10^{14} h^{-1} M_{\odot}$ for three cosmologies, as indicated in the plot. [After Borgani (2008)].

of galaxies in clusters and the masses of clusters themselves. The scatter in this relation leads to a systematic error in the mass function. Since the mass function is steep, an observable proxy for cluster mass M_{obs} is biased high compared with the true mass M since it is more likely that one of the numerous low mass objects is up–scattered to higher values of mass than it is that a rare high mass object is down–scattered to lower values of mass. For the case of a lognormal mass–observable relation with rms $\sigma_{\ln M}$ that is small compared with the scale over which the local slope of the mass function changes, the distribution of masses must be corrected by applying the following relation between the true mass and its observational estimate (Mortonson et al., 2011):

$$\ln M = \ln M_{obs} + \frac{1}{2}\gamma\sigma^2_{\ln M} \tag{2.50}$$

where $dn/d\ln M \propto M^{\gamma}$. This shift in the mass function due to the scatter in the scaling relation is the so–called *Eddington bias*.

2.7 Numerical simulations

In the Sect. 2.5 we have seen that an analytical solution for the collapse of DM structures in the non linear regime is not possible for the general case. Also, although useful to capture some aspects of the general picture of structure formation, this kind of approach is way too simple to understand in detail the complex process of build-up of cosmic structures such as galaxy clusters.

Nowadays, a widely used approach consists in the use of numerical simulations, that have constituted a powerful tool since the late 70s. The idea beneath this technique is to discretize and sample the DM phase space by a number N of particles, the so called *"bodies"*. These particles are initially distributed so as to reproduce the initial density field with the statistical properties correct for the assumed cosmological model. These particles feel the mutual gravitational force, and the equations of motion are integrated to provide the trajectories. In this way it is possible to follow the evolution of cosmic structures through the non linear regime starting from the initial conditions set to reproduce the early stage of linear evolution. A further step consists in the inclusion of the baryonic physics. Baryons must in fact interact both gravitationally, with themselves and with DM particles, and hydrodynamically. There exist two approaches to deal with hydrodynamics: the Lagrangian and the Eulerian approach.

In the following section the main aspects of the DM only simulations and the techniques used to simulate the baryonic physics are briefly summarized.

2.7.1 Initial conditions

The first fundamental step in setting up a simulation is the generation of initial conditions, that must reflect the statistical properties of the initial conditions of the Universe, described at the beginning of Sect. 2. At this epoch the density fluctuations are small and the usual assumption is that such initial density field is random Gaussian, described by the power spectrum $P(k)$ (see Sect. 2.2.1). In order to reproduce such field, particles are located on a grid and are slightly moved so as the fluctuations in this way generated have the correct power spectrum.

Two random numbers, ϕ and A, are generated, both $\in (0,1]$, for each point of the k–space. The Fourier coefficients of the contrast density field then becomes:

$$\hat{\delta}_k = \sqrt{-2P(k)\ln(A)}e^{i2\pi\phi} \tag{2.51}$$

If $\vec{q}$ are the particle coordinates in the real space, the potential reads:

$$\Phi(\vec{q}) = \sum_k \frac{\widehat{\delta}_k}{k^2} e^{i\vec{q}\vec{k}} \tag{2.52}$$

Initial position and velocity are assigned to particles via a displacement in the phase space according to the Zel'dovich approximation (see Sect. 2.4):

$$\vec{x} = \vec{q} - D_+(z)\vec{\nabla}\phi(\vec{q}) \tag{2.53}$$

$$\vec{v} = \dot{D}_+(z)\vec{\nabla}\phi(\vec{q}) \tag{2.54}$$

2.7.2 N–body methods

There exist several approaches to compute the trajectories of the particles due to the mutual gravitational attraction. The first one is the simplest and consists in the direct computation of the gravitational force acting on each particle due to all the other particles:

$$\vec{F}_{ij} = \frac{G m_i m_j (\vec{x}_i - \vec{x}_j)}{(|\vec{x}_i - \vec{x}_j|^2 + \epsilon^2)^{3/2}} \tag{2.55}$$

where G is the gravitational constant, m_i and m_j are the particle masses, $\vec{x}_i$ and $\vec{x}_j$ are the particle positions and ϵ is the *softening parameter* . This is the so called *Particle–Particle* (PP) method. By this approach, particles do not have a dimension, therefore it might happen that particles get arbitrarily close to one another, causing the force to artificially diverge. To avoid this, the softening parameter is introduced, limiting the force in case of particles getting too close. This method is very accurate, as it is the direct computation of the equations of motions. The flip side is the high computational cost. The number of computations scales like $N(N-1)/2$, where N is the total number of particles. Nowadays this method is no longer applied to the entire cosmological box, but is still in use in the very high density regions, where a high precision is required.

The *Particle–Mesh* (PM) technique allows to reduce the computational cost. The idea beneath this method is the evaluation of the gravitational potential on a grid to compute the gravitational interactions. More precisely, the density field is evaluated in the mesh points, then the Poisson equation is solved in the Fourier space. In Fourier space also the potential is computed by means of the Green's theorem. Finally, the forces acting on the particles are obtained by interpolating the derivatives of the potential at the particle positions. The use of a regular grid with periodic

boundary conditions allows to easily solve the equations in the Fourier space, making the computation much faster than for the PP case. In fact the computational cost scales like $N \log N$, where N is the number of grid points. In this case the flip side is the low resolution of this technique. To overcome such problem, an hybrid method has been developed, the so called *Particle–Particle–Particle–Mesh*, or, briefly, P^3M. This approach makes use of the PP algorithm for the computation of short range interactions, and the PM for the long distance ones. A further improvement is the use of *Adaptive Mesh Refinements* (AMR) codes, where the grid step is set to different values according to the local density, in order to have higher resolution in the high density regions, and save computational cost in the low density regions.

The last technique we want to present here is the *Tree algorithm*. It performs a hierarchical subdivision that resembles the structure of a tree. The idea is to treat distant clumps of particles as a single massive particle. In order to locate these clumps of particles, the space is partitioned in cubic cells. This partitioning is carried out until each cell contains either 1 or 0 particles. The full mass distribution is the *root* and each further subdivision locates a *node*. The cells containing one paricle are called *leaves*. Each cell, small or large, is characterized by the enclosed total mass and the center-of-mass of the particles. To compute the force acting on a particle, its distance D from a node is computed. The cell is considered as a single particle if $l/D < \theta$, l being the length of the cell, and θ is an adjustable parameter usually taken ~ 1. If this condition is not satisfied, the condition is checked on the smaller node. This proceeds iteratively until a leaf is reached. In this way the effective number of particles used to perform the computation is decreased only where it is convenient. Although by this method the force is computed faster, at each timestep the tree must be stored, making this method the most memory consuming.

2.7.3 Hydrodynamical techniques

The methods so far discussed are suitable for dealing with the N-body issue. However, although DM is the most abundant component in mass, most of the observable phenomena comes from the baryonic matter. Such component must be reproduced in simulations taking into account thermodynamic and radiative processes, star formation, feedback from supernovae and active galactic nuclei (AGN hereafter) and chemical enrichment. A fluidynamic approach allows to deal with all the above mentioned processes. The two main approaches are the grid-based Eulerian and the gridless Lagrangian methods.

Eulerian schemes: by this kind of approach, the variations of physical quantities

(like velocity, pressure, internal energy, etc...) of the fluid are followed. Such properties of the fluid are evaluated on the cells of a grid. The latter can either be fixed or adaptive (*Adaptive Mesh Refinement* (AMR) schemes), but in both cases the main problem is the limited spatial resolution. Even though with the AMR schemes such issue is not critical, the Eulerian scheme is still not as efficient as an SPH code (see below) as far as the resolution is concerned. On the other hand, the main advantage is the intrinsic skill of dealing with shocks without adding any artificial term, as needed in the Lagrangian schemes.

Lagrangian schemes: in this case the fluid is discretized, and each fluid element, to which all the physical quantities are associated, is followed along its evolution through time. The main advantage lies in the high spatial resolution achievable. Furthermore, it is much easier to implement with respect to a grid based method, as it resembles the logic by which the DM is treated in the N-body codes. The flip side resides in the treatment of shocks, that can be captured only by adding an artificial viscosity. Another important disadvantage lies in the difficulty to reproduce arbitrarily high density gradients with a finite number of particles.

A particular implementation of the Lagrangian technique is the *Smoothed Particles Hydrodynamics* (SPH hereafter). Since this is the technique adopted in the set of simulations used in this thesis, we now briefly present the main features of this method. As previously described, in the Lagrangian techniques the fluid is discretized, and the fluid particles are evolved according to hydrodynamics laws. Physical quantities are smoothed among neighbour particles to avoid statistical fluctuations. Given a quantity $f(\vec{r})$, its mean value is:

$$\langle f(\vec{r})\rangle = \int W(|\vec{r}-\vec{r'}|,h) f(\vec{r'}) d^3\vec{r'} \tag{2.56}$$

where W is the *smoothing kernel* below described, and h is the spatial scale on which the mean is computed and therefore can be considered as the effective resolution.

To each fluid element is assigned a density ρ_i, a mass m_i ans a position $\vec{r}_i$. Let the value of the quantity f associated to the i–th particle be A_i. Eq. 2.56 can be recast as follows:

$$\langle f(\vec{r})\rangle = \int W(|\vec{r}-\vec{r'}|,h) \frac{f(\vec{r'})}{\rho(\vec{r'})} \rho(\vec{r'}) d^3\vec{r'} \tag{2.57}$$

and it can be discretized substituting the mass element $\rho(\vec{r'})d^3\vec{r'}$ with m_i. The integral becomes then a sum:

$$f(\vec{r'}) = \sum_j m_j \frac{A_j}{\rho_j} W(|\vec{r} - \vec{r}_j|, h) \tag{2.58}$$

In this way the hydrodynamical quantities are discretized and the fluid equations can be solved. The mass conservation is assured by the normalization imposed to the kernel ($\int W(\vec{r})d^3r = 1$), while in the adiabatic regime the Euler and the energy conservation equations become respectively:

$$\left(\frac{d\vec{v}}{dt}\right) = -\sum_{j=1}^{N} m_j \left[\frac{P}{\rho^2} + \frac{P_j}{\rho_j^2}\right] \vec{\nabla} W(|\vec{r} - \vec{r}_j|, h) \tag{2.59}$$

$$\left(\frac{d\epsilon}{dt}\right) = \frac{P}{\rho^2} \sum_{j=1}^{N} m_j (\vec{v} - \vec{v}_j) \vec{\nabla} W(|\vec{r} - \vec{r}_j|, h) \tag{2.60}$$

The kernel W represents the volume within which the mean is computed, assigning a different weight to the particles, weighting more the closer ones. In fact the interactions among particles decays like the distance. Weighting all particles in the simulation would require a prohibitive computational cost. Therefore a kernel with compact support is usually adopted, like the following one, adopted in the simulations used for this thesis:

$$W(r,h) = \frac{8}{\pi h^3} \begin{cases} 1 - 6(r/h)^2 + 6(r/h)^3 & 0 \leq r \leq h/2 \\ 2(1 - r/h)^3 & h/2 \leq r \leq h \\ 0 & r \geq h \end{cases} \tag{2.61}$$

2.7.4 The GADGET–3 code

The simulations used for this thesis have been carried out with the TreeePM–SPH GADGET-3 (**G**Alaxies with **D**ark matter and **G**as int**E**rac**T**) code, a more efficient version of the previous GADGET-2 code (Springel, 2005). As for the computation of the gravitational force, the Plummer-equivalent softening length is fixed to $\epsilon = 5\,h^{-1}$ kpc in physical units below z = 2, while being kept fixed in comoving units at higher redshift. Besides the DM–only simulation, we also carried out a set of non–radiative hydrodynamic simulations and two sets of radiative simulations, based on different models for the release of energy feedback. The astrophysical processes implemented in the SPH scheme used in our simulations are described below.

Radiative cooling

In our simulations radiative cooling rates are computed by following the same procedure presented by Wiersma et al. (2009). The code also includes a photo-ionising, time-dependent, uniform ultraviolet UV/X–ray background radiation expected from quasars and first stars Haardt and Madau (1996), which reionises the Universe at $z \simeq 6$. The effect of a photo-ionising background is that of significantly altering the cooling function and inhibiting gas collapse and subsequent star formation. The contributions to cooling from each one of eleven elements (H, He, C, N, O, Ne, Mg, Si, S, Ca, Fe) have been pre–computed using the publicly available CLOUDY photo–ionisation code (Ferland et al., 1998) for an optically thin gas in (photo–ionisation) equilibrium. Gas particles above a given threshold density are treated as multiphase, so as to provide a subresolution description of the interstellar medium, according to the model originally described by Springel and Hernquist (2003).

Star formation

The star formation in treated a sub–grid model for the InterStellar Medium (ISM) following Springel and Hernquist (2003). We refer the reader to this paper for a detailed description. The ISM is modelled as a hot medium inside which cold clouds reside. Such clouds form from the cooling of high density gas. From the collapse of the cold clouds stars can eventually form. In the code, a gas particle is allowed to produce stars if the density ρ_i is above a given threshold and the gas is Jeans unstable, that is:

$$\frac{h_i}{c_i} > \frac{1}{\sqrt{4\pi G \rho_i}} \tag{2.62}$$

where h_i is the SPH smoothing length and c_i is the local sound speed. In order to avoid that at high redshift gas particles exceed the density threshold, and form stars, in regions outside virialized halos, the density must exceed also a value that depends on the mean density of the Universe.

Once the criteria for star formation are satisfied, a gas particle forms star according to the following equation:

$$\frac{d\rho_*}{dt} = -\frac{d\rho_i}{dt} = \frac{c_* \rho_i}{t_*} \tag{2.63}$$

where c is a dimensionless star formation rate parameter and t the characteristic timescale for star formation. This process produces stars continuosly, but for

computational reasons a new star particle is created only after a significant part of the gas particle mass has turned into stars according to the above formula. This process takes place until the gas particle is entirely transformed into stars. From one gas particle few star particles are generated, typically 2-3. This is set to avoid spurious numerical effects due to gravitational interactions of particles with widely differing masses. The newly produced star particle constitue a Simple Stellar Population, that is a coeval population of stars characterised by a given assumed initial mass function (IMF) and same metallicity.

Some of the stars can explode as supernovae (SN). To model this, in the code all the stars more massive than $8M_{\odot}$ are assumed to end as SN type–II, releasing the energy (typically 10^{51} *erg* per SN) to the surrounding gas. This is done under the *instantaneous recycling approximation* (IRA), since the lifetime of a massive star can be considered shorter than the typical timestep of the simulation.

SNe are the responsible for the chemical enrichment of the ISM. There are three channels for the production and distribution of metals.

- Stars in the mass range $0.8 - 8M_{\odot}$ can give rise to a type–Ia SN. In fact a white dwarf in a binary system can accrete material from the companion. This causes the dwarf's core to reach the ignition temperature for carbon fusion triggering the explosion.

- A star more massive than $8M_{\odot}$ at the end of the hydrostatic core burning undergo an electron capture process, leading to a core collapse. The explosion that follows ejects the external layers, giving rise to a SN type–II that enriches the ISM with the elements produced by the star.

- a third way to eject matter in the ISM is the mass loss of intermediate and low mass star by stellar winds.

Stars of different mass have different lifetimes, therefore the release of metals is different and must taken into account. Many have been proposed, either independent (Padovani and Matteucci, 1993; Maeder and Meynet, 1989; Chiappini et al., 1997) or dependent on the metallicity (see e.g. Portinari et al., 1998).

Another important quantity to compute the metal release is the yield. It specifies the amount of different metal species which are released during the evolution of a SSP. For more details on the implementation of the yields we refer the reder to Tornatore et al. (2007).

One of the most important quantity in modelling the star formation process is the initial mass functon (IMF) $\Phi(m)$. It is defined as the number of stars of

a given mass per unit logarithmic mass interval. It determines the relative ratio between SNII and SNIa and, therefore, the relative abundance of α-elements and Fe-peak elements. The shape of the IMF also determines how many long-living stars will form with respect to massive short-living stars. This ratio affects the amount of energy released by SNe and the present luminosity of galaxies, which is dominated by low-mass stars.

There is no general agreement on whether the IMF at a given time is universal or dependent on the environment, or whether it is time dependent, meaning that local variations of the values of temperature, pressure and metallicity in star–forming regions affect the mass distribution of stars. The most commonly used are the IMFs proposed by Salpeter (Salpeter, 1955), Kroupa (Kroupa, 2001) and Chabrier (Chabrier, 2003). In our simulations stars of different mass are distributed according to a Chabrier IMF, releasing metals over the time-scale determined by the corresponding mass-dependent life-times taken from Padovani and Matteucci (1993)

Feedback from galactic winds

It is well known (e.g. Balogh et al., 2001; Borgani et al., 2004) that cooling causes the formation of too many stars. In order to regulate star formation and prevent overcooling, an efficient mechanism to thermalize the SNe energy feedback must be implemented. This is made by introducing a phenomenological description for galactic winds, which are triggered by the SNII energy release.

Galactic outflows are observed (e.g. Martin, 1999) and are thought to play a key role in transporting energy and metals produced by the stellar population into the IGM/ICM. The momentum and the kinetic energy of these winds are regulated by two parameters, η and χ. As suggested by Martin (1999), the wind mass loading is proportional to the star formation rate $\dot{M}_*$:

$$\dot{M}_W = \eta \dot{M}_* \tag{2.64}$$

Following Springel and Hernquist (2003), in the simulations used for this thesis it is assumed $\eta = 3$. The fraction of SNe energy that powers the wind is regulated by the parameter χ according to:

$$\frac{1}{2}\dot{M}_W v_W^2 = \chi \epsilon_{SNe} \dot{M}_* \tag{2.65}$$

where ϵ_{SNe} is the energy feedback provided by the SNe under the IRA for each solar mass of stars formed.

Winds are originated from gas particles which are stochastically selected among the multiphase particles, with a probability proportional to their local SFR. Therefore these particles come from star–forming regions and hence are heavily metal-enriched.

As described in Tornatore et al. (2007), in the simulations used for this thesis the scheme of kinetic feedback associated to wind galactic is left unchanged, using instead the value of the wind velocity, v_w, as a parameter to be fixed. In our simulations we used two different values: $500 km\, s^{-1}$ for the set without AGN feedback, and $350 km\, s^{-1}$ for the set with AGN feedback.

AGN feedback

Black hole (BH) growth and the associated energy release are responsible for a a number of phenomena in galaxies and galaxy clusters, first of all on the star formation in these systems. In Sect. 6 the effect of the feedback from BHs on the dynamics of galaxies in clusters is analyzed and discussed.

In particular during a major phase of BH accretion strong outflows are produced, which interact with the surrounding gas. These outflows constitute a feedback process, the so–called *AGN* (active galactic nulei) feedback, that must be taken into account when modelling galaxy and galaxy cluster formation.

The present simulations do not have enough resolution to follow the details of BH growth. We must therefore use a sub–resolution description of supermassive BH growth in galactic nuclei and the consequent feedback on the surrounding gas. Following the approach presented in Springel et al. (2005a), BHs are described as sink particles, which grow their mass by gas accretion and merging with other BHs. A detailed description on the BH feedback implemented in the simulations used in this thesis is presented in Hirschmann et al. (2013).

The accretion rate onto the black hole is parametrized by:

$$\dot{M}_{\rm B} = \frac{4\pi\, \alpha\, G^2 M_{\rm BH}^2\, \rho}{(c_s^2 + v^2)^{3/2}} \tag{2.66}$$

where ρ and c_s are the density and sound speed of the gas, respectively, α is a boost factor for the density set to $100 M_\odot$, and v is the velocity of the black hole relative to the gas. The accretion is limited to the Eddington rate

$$\dot{M}_{\rm Edd} \equiv \frac{4\pi\, G\, M_{\rm BH}\, m_{\rm p}}{\epsilon_{\rm r}\, \sigma_{\rm T}\, c} \tag{2.67}$$

where $m_{\rm p}$ is the proton mass, $\sigma_{\rm T}$ is the Thomson cross-section. $\epsilon_{\rm r}$ is the radiative efficiency which is related to the radiated luminosity $L_{\rm r}$ by:

$$L_{\rm r} = \frac{\epsilon_{\rm r}}{1-\epsilon_{\rm r}} \dot{M}_{\rm BH}\, c^2 \tag{2.68}$$

where $\dot{M}_{\rm BH}$ is the accretion rate. It sets the fraction of the rest-mass energy of the accreted gas converted into radiated energy. It is set to 0.1 in the simulations used for this thesis, and is increased to $\epsilon_f = 0.4$ whenever accretion enters in the quiescent "radio" mode and takes place at a rate smaller than one-hundredth of the Eddington limit (e.g. Sijacki et al., 2007; Fabjan et al., 2010).

The BH mass is correspondingly decreased:

$$\dot{M}_{\rm BH} = min(\dot{M}_{\rm Edd}, \dot{M}_{\rm B}) \tag{2.69}$$

with the further requirement that its mass changes because of the feedback:

$$\Delta M_{\rm BH} = (1-\epsilon_r)\dot{M}_{\rm BH}\Delta t \tag{2.70}$$

Some fraction $\epsilon_{\rm f} = 0.1$ of the radiated luminosity $L_{\rm r}$ is thermally coupled to the surrounding gas, providing the feedback mechanism.

A difference with the original prescription by Springel et al. (2005a) deals with the BH seeding. Since BH must be seeded only in halos with a sufficient star formation, a total stellar mass of $10^{11} M_\odot/h$ is required for a halo to be seeded with a black hole particle (starting with a seed mass of $10^6 M_\odot/h$). The position of the BH particle is taken as the potential minimum of the FoF group.

One of the technical issues one has to face with when implementing AGN feedback deals with BH particles wandering away from the centre of galaxies by numerical effects. In order to prevent this, a strict momentum conservation for the smooth accretion of the gas is imposed, without any momentum transfer when the gas is swallowed. Also, the conservation of momentum and centre of mass of two BH particles merging is implemented. Moreover the dynamical friction force acting on the BH particles is explicitly computed. In this way a black hole particle remains within the host galaxy, even when it becomes a satellite of a larger halo.

3

Dynamics of collisionless systems

In Chapter 2 the processes giving rise to cosmic structures are presented. Small fluctuations of an initial density field grow because of their own gravitational attraction. The regions where the density becomes large enough can detach from the Hubble flow and collapse to form the structures nowadays we observe. The collapse does not end up in a singularity. For a collisional fluid it is easy to understand that pressure can balance the gravitational attraction, providing a mechanism for stopping the collapse. Since most of the matter, $\sim 84\%$ according to latest result by Planck data analysis (Planck Collaboration et al., 2013), in the Universe is *dark matter*, which is non–collisional, this cannot be the reason why structures do not end up in singularities. In this chapter we present the theoretical framework that describes the equilibrium configurations that non–collisional matter can achieve thanks to its own velocity dispersion.

In the last part of this chapter we present three techniques that make use of the dynamics of some tracers of the dynamics to infer properties of the systems. The dynamics in fact carries information on the energy content ,the structure and the assembly history of the cosmological objects, providing information on quantities that cannot be directly observed.

3.1 The collisionless Boltzmann equation

A complete description of a non–collisional system is provided by the *distribution function* $f(\vec{x}, \vec{v}, t)$, which is the density in the phase space. The number of objects

lying in the volume d^3x centered in $\vec{x}$ and having the velocity vector lying inside the volume d^3v centered in $\vec{v}$ is given by the following relation:

$$dn = f(\vec{x}, \vec{v}, t) d^3x d^3v \tag{3.1}$$

By definition $f \geq 0$. If the distribution function is known at the time t_0, it is possible to recover the configuration of the system at any time. For convenience we shall introduce the position vector in the phase space:

$$(\vec{x}, \vec{v}) \equiv \vec{w} \tag{3.2a}$$

$$\dot{\vec{w}} = (\dot{\vec{x}}, \dot{\vec{v}}) = (\vec{v}, -\vec{\nabla}\Phi) \tag{3.2b}$$

where Φ is the gravitational potential. Since in a non–collisional fluid there are no sudden changes in the particle position in the phase space, as we would have in case of collisions, it is possible to introduce a *continuity equation* for f:

$$\frac{\partial f}{\partial t} + \sum_{\alpha=1}^{6} \frac{\partial (f \dot{w}_\alpha)}{\partial w_\alpha} = 0 \tag{3.3}$$

Since x_i and v_i are independent coordinates in the phase space, the following relation holds:

$$\sum_{\alpha=1}^{6} \frac{\partial \dot{w}_\alpha}{\partial w_\alpha} = \sum_{i=1}^{3} \left(\frac{\partial v_i}{\partial x_i} + \frac{\partial \dot{v}_i}{\partial v_i} \right) = - \sum_{i=1}^{3} \frac{\partial}{\partial v_i} \left(\frac{\partial \Phi}{\partial x_i} \right) = 0 \tag{3.4}$$

where the last equality is due to the fact that the gravitational potential does not depend on velocity. Using this relation in the eq. (3.3) we obtain the *non–collisional Boltzmann equation*:

$$\frac{\partial f}{\partial t} + \sum_{\alpha=1}^{6} \dot{w}_\alpha \frac{\partial f}{\partial w_\alpha} = 0 \tag{3.5}$$

To better understand the meaning of this equation, we now recast it in another form by making use of the Lagrangian derivative:

$$\frac{df}{dt} = \frac{\partial f}{\partial t} + \sum_{\alpha=1}^{6} \dot{w}_\alpha \frac{\partial f}{\partial w_\alpha} \tag{3.6}$$

The collisionless Boltzmann equation then reads:

$$\frac{df}{dt} = 0 \tag{3.7}$$

This means that the fluid is incompressible in the phase space.

3.2 The Jeans equations

The distribution function f depends on 7 variables, therefore it is usually quite difficult to solve the collisionless Boltzmann equation. Still, the moments of eq. (3.7) can provide useful information. Such equation can be recast as follows:

$$\frac{\partial f}{\partial t} + \sum_{i=1}^{3} \left(v_i \frac{\partial f}{\partial x_i} - \frac{\partial \Phi}{\partial x_i} \frac{\partial f}{\partial v_i} \right) = 0 \tag{3.8}$$

And integrating the velocities we obtain:

$$\int \frac{\partial f}{\partial t} d^3v + \int v_i \frac{\partial f}{\partial x_i} d^3v - \frac{\partial \Phi}{\partial x_i} \int \frac{\partial f}{\partial v_i} d^3v = 0 \tag{3.9}$$

where we have adopted the summation convention. The phase space volume within which we are integrating (this means all the velocities) does not depend on time and v_i does not depend on x_i. The time derivative and $\partial/\partial x_i$ can be taken out of the integrals. The surface of the integration volume is composed by the velocities with modulus ∞. The theorem of the divergence states that $\int_V \vec{\nabla} f d^3x = \int_S f \cdot \hat{n} d^2S$, where $\hat{n}$ is a versor perpendicular to the surface element d^2S. The last term of the equation vanishes, since there are no particles with infinite velocity. By defining the space density and the mean velocity as follows:

$$\nu \equiv \int f d^3v \qquad \overline{v}_i \equiv \int f v_i d^3v \tag{3.10}$$

eq. (3.9) reads:

$$\frac{\partial \nu}{\partial t} + \frac{\partial (\nu \overline{v}_i)}{\partial x_i} = 0 \tag{3.11}$$

Multiplying eq. (3.8) times v_j, integrating over the velocities and applying the divergence theorem we obtain:

$$\frac{\partial (\nu \overline{v}_j)}{\partial t} + \frac{\partial (\nu \, \overline{v_i v_j})}{\partial x_i} + \nu \frac{\partial \Phi}{\partial x_j} = 0 \tag{3.12}$$

where $\overline{v_i v_j} = \frac{1}{\nu} \int v_i v_j f d^3v$. We can rewrite this equation by performing the following operation: (3.12) $- \overline{v}_j$(3.11). We obtain:

$$\frac{\partial \overline{v}_j}{\partial t} + \overline{v}_i \frac{\partial \overline{v}_j}{\partial x_i} = -\frac{\partial \Phi}{\partial x_j} - \frac{1}{\nu} \frac{\partial (\nu \sigma_{ij}^2)}{\partial x_i} \tag{3.13}$$

where we have introduced the *stress tensor*, that describes an anisotropic pressure:

$$\sigma_{ij}^2 = \overline{(v_i - \overline{v}_i)(v_j - \overline{v}_j)} = \overline{v_i v_j} - \overline{v}_i \overline{v}_j \tag{3.14}$$

The last term of such equation is the equivalent of the pressure term of the Euler equation. The velocity field of the non–collisional matter provides a support to the system against the collapse in the same way the pressure does in a collisional system.

3.3 Equilibrium of spherical systems

As presented in detail in Binney and Tremaine (1987), considering eq. (3.5) in spherical coordinates, and taking its moments we obtain the equivalent of eq. (3.13) in spherical coordinates.

$$\frac{d(\nu\overline{v_r^2})}{dr} + \frac{\nu}{r}\left[2\overline{v_r^2} - \left(\overline{v_\theta^2} + \overline{v_\phi^2}\right)\right] = -\nu\frac{d\Phi}{dr} \tag{3.15}$$

Using the velocity dispersion σ instead of the velocity rms, we shall now impose a further condition: let the system be invariant under rotations about the center. This means that the system appears statistically isotropic. This implies that $\overline{\sigma_\theta^2} = \overline{\sigma_\phi^2}$. Let us define the *velocity anisotropy parameter*:

$$\beta = 1 - \frac{\sigma_t^2}{\sigma_r^2} \tag{3.16}$$

where $\sigma_t = [\frac{\sigma_\theta^2 + \sigma_\phi^2}{2}]^{1/2}$ is the tangential velocity dispersion. The anisotropy parameter quantifies the anisotropy of the orbits. Such anisotropy is due to many processes like dynamical friction, tidal processes, infall. The anisotropy parameter therefore provides important information about such processes.

Cosmic structures form by the collapse of perturbations, therefore we may expect the radial velocity dispersion to be greater than the tangential component. Substituting the expression for the gravitational potential $d\Phi/dr = GM(r)/r^2$, eq. (3.15) reads:

$$\boxed{M(r) = -\frac{r\sigma_r^2}{G}\left(\frac{d\ln\nu}{d\ln r} + \frac{d\ln\sigma_r^2}{d\ln r} + 2\beta\right)} \qquad \text{Jeans equation} \tag{3.17}$$

Although this equation is derived from the Jeans equations (3.11)-(3.12)-(3.13), hereafter we will refer to eq. (3.17) as *the Jeans equation*. The particles that satisfy this equation are in equilibrium. It is possible to read this equation in another way: particles in equilibrium are tracers of the potentials because with their kinematics it is possible to infer the potential.

3.4 The virial theorem

So far we have dealt with the information on the single particles, but we may want to have information on the global statistical properties of the systems. This resembles the thermodynamical approach, where macroscopical quantities like temperature or pressure are derived from the dynamics of particles.

In Sect. 3.1 we have defined f as the number of particles in the phase space volume. That was an arbitrary choice, and another definition could have been used, like the luminosity or the mass within that volume. We now use it as the mass, and the number density ν can therefore be replaced with the mass density ρ. From eq. (3.12) we obtain:

$$\int x_k \frac{\partial(\rho\overline{v}_j)}{\partial t} d^3x = -\int x_k \frac{\partial(\rho\overline{v_i v_j})}{\partial x_i} d^3x - \int \rho x_k \frac{\partial\Phi}{\partial x_j} d^3x \tag{3.18}$$

The last term is the so–called *potential energy tensor* W_{jk}. Assuming the density to be null at the infinite, and applying the divergence theorem to the first term on the right hand side gives:

$$\int x_k \frac{\partial(\rho\overline{v}_j)}{\partial t} d^3x = -\int \rho\overline{v_j v_k} d^3x = 2K_{jk} \tag{3.19}$$

where K_{jk} is the *kinetic energy tensor* and it can be decomposed in two terms by means of the stress tensor:

$$K_{jk} = T_{jk} + \frac{1}{2}\Pi_{jk} \tag{3.20}$$

with

$$T_{jk} = \frac{1}{2}\int \rho\overline{v}_j\overline{v}_k d^3x \tag{3.21a}$$

$$\Pi_{jk} = \int \rho\sigma^2_{jk} d^3x \tag{3.21b}$$

Let A_{jk} be the first term of eq. 3.19 and consider $(A_{jk} + A_{kj})/2$. Since the tensors W_{jk},T_{jk} and Π_{jk} are symmetric we obtain:

$$\frac{1}{2}\frac{d}{dt}\int \rho(x_k \overline{v}_j + x_j \overline{v}_k) d^3x = 2T_{jk} + \Pi_{jk} + W_{jk} \tag{3.22}$$

Let the *inertia tensor* be defined as follows:

$$I_{jk} = \int \rho x_j x_k d^3x \tag{3.23}$$

it is possible to demonstrate that (see Binney and Tremaine, 1987)

$$\frac{dI_{jk}}{dt} = \frac{d}{dt}\int \rho(x_k \overline{v}_j + x_j \overline{v}_k) d^3x \tag{3.24}$$

Combining it with eq. (3.22) we obtain the *tensorial virial theorem*:

$$\frac{1}{2}\frac{d^2 I_{jk}}{dt^2} = 2T_{jk} + \Pi_{jk} + W_{jk} \tag{3.25}$$

Taking the trace of eq. (3.21) we obtain $Tr(T) + Tr(\Pi)/2 = K =$ kinetic energy. It is also possible to demonstrate that the trace of W_{ij} is the potential energy of the system. Imposing the system to be in a steady state, the second derivative of the inertia is null, and we obtain:

$$\boxed{2K + W = 0} \qquad \text{Virial theorem} \tag{3.26}$$

Let E be the total mechanical energy if a system. The following relation holds:

$$E = K + W = -K = \frac{1}{2}W \tag{3.27}$$

A system forming by its material collecting together from a state of rest at infinity, in which $E_{in} = K_{in} = W_{in} = 0$, will successively collapse reaching an equilibrium configuration. In this phase the system is bound and $0 < E_f = -K_f = W_f/2$. Half of the potential energy contributes to the increase of the kinetic energy of the system, and in some way the other half is disposed in order to achieve a binding energy $E_b = -E = K$.

3.5 Relaxation of collisionless structures

In dynamics, relaxation is the process by which a system approaches equilibrium or by which it returns to equilibrium after a disturbance. So far we have considered the process of collisionless structure formation either in the initial moments or in the final ones, where equilibrium has settled. We now want to investigate the processes that lead to equilibrium. There exists a great variety of equilibrium configurations, but structures, like galaxies or galaxy clusters, seem to occupy a relatively small volume of this configuration space. In fact such objects obey a number of tight scaling relations and have a restricted variety of density profiles.

In this section we want to discuss what determines the particular configuration to which a collisionless system settles. In order to address this question we shall first make some considerations about the distribution function. If the latter is interpreted as a probability function, $f(\vec{x},\vec{v})d^3xd^3v$ gives the number of particles in an infinitesimal volume of the phase space. in this way it is possible to study the evolution of the distribution function by applying the collisionless Boltzmann equation, this distribution function is not observable. The number of objects, like galaxies in a cluster, in a finite volume of phase space is the quantity we can observe. It is therefore convenient to define a *coarse–grained distribution function* $f_c(\vec{x},\vec{v})$ as the average of f in some phase–space volume element centered on $(\vec{x},\vec{v})$. Given this definition, the coarse-grained DF does not obey the collisionless Boltzmann equation. However, an observer would detect an equilibrium configuration if $\partial f_c/\partial t = 0$, as there is no observable evolution. An operational definition of relaxation may therefore be that of a process leading the system toward a state with $\partial f_c/\partial t \simeq 0$.

By doing a comparison with what happens to a collisional gas that settles to a Maxwell–Boltzmann velocity distribution, we might expect that the collisionless particles approach a "most probable" state. In order to do that we have to seek the probability density p that maximizes the *entropy*:

$$S \equiv -\int_{\text{phase space}} p \ln p d\tau \tag{3.28}$$

where τ is the phase space volume. Identifying the probability density p with the distribution function f, and the volume in the phase space τ with d^3xd^3v, we obtain the entropy for a collisionless system. It can be shown (Binney and Tremaine, 1987) that for a system of finite mass and energy, no $f(\vec{x},\vec{v})$ maximizes the entropy. The more concentrated a system is, the larger the entropy becomes. Physically this is due to the long–range nature of gravity, which allows bound particles to fill an

infinitely large volume in phase space. Eq. (3.7) applied to eq. (3.28) guarantees that $dS/dt = 0$, meaning that the relaxation process is adiabatic. In this case there is no evolution to a "most probable" state. Different conclusions are reached if we consider the coarse–grained distribution function f_c. In this case there are hints that $S = S(t)$ may be a non–decreasing function of time, although the question is still debated (Mo et al., 2010).

The entropy approach is based on the idea of looking for some fundamental physical process that leads the system to an equilibrium state. Another approach is to consider the equilibrium configuration as a reflection of the particular initial conditions. By following this approach, we now discuss four relaxation mechanisms: phase mixing, chaotic mixing, violent relaxation and Landau damping.

3.5.1 Phase and chaotic mixing

Let us consider two particles orbiting in a potential, and having orbits with similar initial frequency and phase. This means that the trajectories in the phase space are very close to each other. The small difference in the phase after some time grows considerably. They separate linearly in the phase space, and the process is called *phase mixing*.

During this process, while f remains constant, the coarse–grained distribution function f_c decreases with time, as more and more unoccupied phase–space volume is mixed in. After some time, however, f_c stops evolving. In this sense phase mixing is considered a relaxation process. The time scale for the relaxation to occur strongly depends on the particular configuration of the system, but it is usually much longer than a dynamical time.

Fig. 3.1 provides a schematic representation of how an initially compact group of points in the phase space spreads out in a larger region of lower coarse–grained phase space density.

If the orbits are not regular as in the case just described, then they experience the so–called *chaotic mixing*. Two such kind of orbits, initially close one another, diverge exponentially as time goes by. The orbits will spread through the "Arnold web" (Mo et al., 2010), entirely covering it after some time. As in the phase mixing case, the chaotic mixing relaxes the coarse–grained distribution function leaving unaltered the fine–grained one. Because of the exponential divergence of the trajectories, chaotic mixing erases the memory of initial conditions faster than the phase mixing does.

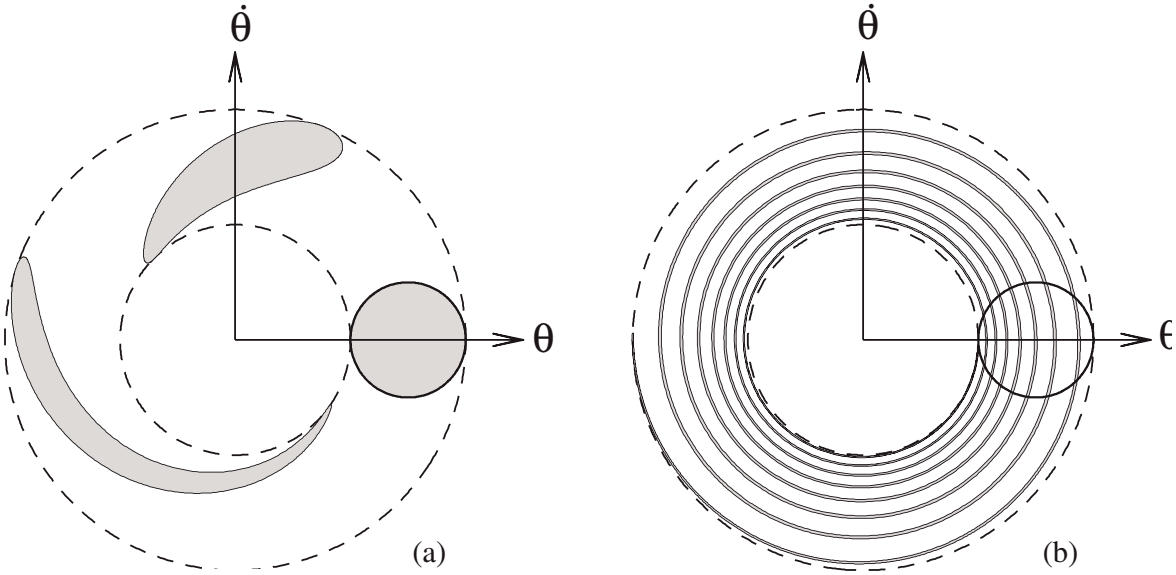

Figure 3.1: Schematic representation of the phase mixing process. Dashed lines represent orbits of constant energy. (a) The shaded circle is the initially compact group of points. The slightly different periods of the point cause these points to spread out, as shown by the shaded areas representing two successive moments of the evolution. (b) After several dynamical times the coarse–grained phase space density becomes constant within the annulus. [After Mo et al. (2010)]

3.5.2 Violent relaxation

Let us consider the process of collapse of an initial perturbation in the density field that leads to the formation of a cosmological object like a galaxy cluster. Let the total mechanical energy per mass unit be $\epsilon = v^2/2 + \Phi$. During the collapse the gravitational potential varies considerably. The energy ϵ therefore will change accordingly:

$$\frac{d\epsilon}{dt} = \frac{1}{2}\frac{dv^2}{dt} + \frac{d\Phi}{dt} = \vec{v}\cdot\frac{d\vec{v}}{dt} + \frac{\partial\Phi}{\partial t} + \dot{\vec{r}}\cdot\vec{\nabla}\Phi = \frac{\partial\Phi}{\partial t} \tag{3.29}$$

where we have used $\dot{\vec{v}} = -\vec{\nabla}\Phi$. The way energy changes depends on the particular configuration of the system, but the overall effect is a broadening of the energy distribution. A time–varying potential therefore provides a relaxation mechanism called *violent relaxation*.

From eq. (3.29) it is possible to notice that the energy change is independent on

mass. This implies that violent relaxation does not segregate particles according to their mass. This is different from what happens in a collisional system. In this case, two body encounters cause an exchange of momentum. More massive particle transfer energy to lighter ones, becoming more tightly bound sinking toward the center of the system.

Although a time–varying potential may provide a relaxation mechanism, it is not a sufficient condition for equilibrium. One can build time–varying potentials that do not lead to equilibrium. A time–varying potential and a mixing are both needed to have violent relaxation.

The time scale of this relaxation process is:

$$t_{vr} = \left\langle \frac{1}{\epsilon^2} \left(\frac{\partial \Phi}{\partial t} \right)^2 \right\rangle^{-1/2} \tag{3.30}$$

and it is approximately equal to the free–fall time of the system $t_{ff} = (3\pi/32G\bar{\rho})^{1/2}$, where $\bar{\rho}$ is the average density. This shows that the relaxation process is very fast.

It is worth noting that numerical simulations have shown that the process of violent relaxation is never complete. Final energies of the particles appear correlated with their initial values, and so does the shape of the system.

3.5.3 Landau damping

Gravitational interactions damp the perturbation waves of the density field of collisionless particles, providing a mechanism for relaxation.

It is possible to demonstrate that if we consider a fluid with a perturbation wavelength $\lambda < \lambda_J$, where λ_J is the *Jeans length* (see eq. 2.2) then the perturbation is stable. The wave propagates with a phase velocity $v_p = c_s(1 - \lambda^2/\lambda_J^2)^{1/2}$, where c_s is the sound speed. This can be understood by considering that the energy density of an ordinary sound wave is positive. The opposite holds for the gravitational energy density, because the enhanced attraction in the compressed regions is greater than the reduced attraction in the expanded regions. Therefore the Jeans length specifies where the net energy density becomes negative and the system can evolve to a lower energy state by allowing the wave to grow.

In case of a self gravitating collisionless system it is possible to demonstrate that a similar relation holds, provided that the sound speed is substituted with the velocity dispersion σ of the collisionless particles. Perturbations with $\lambda \geq \lambda_J$ are unstable and grow, while those with $\lambda < \lambda_J$ propagate with a group velocity $v_p \leq \sigma$.

The Landau damping works as follows (a mathematical treatment can be found in Binney and Tremaine, 2011). A particle having velocity very different with respect to the wave one will experience no net energy gain. In fact as it overtakes the wave, or is overtaken by it, it falls into the potential perturbation gaining energy, that is immediately lost as it exits the perturbation potential. On the other hand, particles near the resonance of the wave, $v \simeq v_p$, will experience a net change of energy. Those with $v \gtrsim v_p$ will be decelerated by the wave, and a transfer of energy from the particle to the wave occurs. Those with $v \lesssim v_p$ will be accelerated gaining energy at the expense of the wave. Since in general it will be $\partial f/\partial v < 0$, there are more slow moving particles than fast ones. The net result is a transfer of energy from the wave to the particles, therefore the perturbation is damped. The rate is determined by the gradient of the velocity distribution function at the group velocity of the wave. The energy of the perturbation is converted into random motions of the particles. The Landau damping, along with phase mixing, limits the effectiveness of violent relaxation, by damping the potential fluctuations that cause a mixing in particle binding energy.

3.6 The pseudo phase–space density

Numerical simulations have shown that DM halos in equilibrium are characterized by a self–similar spherically averaged density profile. The analytical expression of this profile was first proposed by Navarro et al. (1996, 1997) (NFW hereafter) as the best fit relation for DM halos:

$$\rho(r) = \frac{\rho_0}{\frac{r}{r_s}(1+\frac{r}{r_s})^2} \tag{3.31}$$

where ρ_0 is the normalization and r_s is the so–called *scale radius*. This profile has a cusp in the center, the logarithmic slope being -1, while in the outer regions the slope is -3. The scale radius is the distance from the center where the slope is equal to -2 and therefore is a shape parameter. An equivalent way to express the scale radius is using the *concentration parameter* $c = r_v/r_s$, where r_v is the virial radius. Such concentration parameter has proven to be sensitive to the mass and the epoch of formation of the systems. Generally, the lower the mass of a halo and the higher its formation redshift, the higher its concentration (see, e.g. Muñoz-Cuartas et al., 2011).

The universality appears to hold regardless of the choice of the linear power spectrum of fluctuations Navarro et al. (1997) or when analysing the monolithic build–up of hot dark matter Wang and White (2009).

Such universality seems to be due to some underlying fundamental process. Many have been claimed, like mergers, dynamical friction, angular momentum or entropy generation during virialization (Ludlow et al., 2013), but no general agreement has been achieved. Higher resolution simulations have recently shown deviations from an NFW profile, and a third parameter is actually required to describe the halo shape accurately. The *Einasto profile* has been proposed as a universal profile (see, e.e. Navarro et al., 2010; Ludlow et al., 2011) providing an excellent fit to simulated halos. This profile is characterized by a logarithmic slope with adjustable parameter Γ:

$$\ln(\rho/\rho_s) = -\frac{2}{\chi}\left[\left(\frac{r}{r_s}\right)^{\Gamma} - 1\right] \tag{3.32}$$

Although the Einasto profile provides a better fit to simulated halos than NFW, it does not explain the origin of the universality. In recent years a new quantity has been considered as universal profile, the *pseudo phase space density* (PPSD hereafter):

$$Q(r) = \rho/\sigma^3 \tag{3.33}$$

where ρ is the total matter density profile and σ is the 3D velocity dispersion of the tracers of the gravitational potential (Taylor and Navarro, 2001; Ludlow et al., 2010). An equivalent definition for the PPSD is the following:

$$Q_r(r) = \rho/\sigma_r^3 \tag{3.34}$$

where the total velocity dispersion has been substituted with the radial component σ_r.

Taylor and Navarro (2001) and Dehnen and McLaughlin (2005) have shown that for simulated DM–only halos, the PPSD relation takes a simple power–law expression:

$$Q(r) = \rho/\sigma^3 \propto r^{-\alpha} \tag{3.35}$$

Also $Q_r(r)$ obeys a power-law expression like $Q(r)$, but with a different exponent. A power law is much simpler to characterize than a complex expression like the NFW. Moreover, it is the simplest form that a halo relation could take, and this suggests that the PPSD may be the most fundamental aspect of dark matter halos.

In fact, assuming the PPSD to be a power law, it is possible to analytically derive the density profile of halos. Dehnen and McLaughlin (2005) demonstrates that only one solution exists for a particular "critical" value of α when considering realistic profiles of the velocity anisotropy parameter β (see eq. 3.16). In particular,

they use the radial definition of the PPSD, eq. (3.34), and β depending linearly on $\gamma = -d\ln\rho/d\ln r$, obtaining the value $\alpha = 1.94$.

Different conclusions are reached by Ludlow et al. (2011). By using a set of simulations they showed that the exponent α slightly varies from halo to halo.

If the velocity anisotropy profile is assumed to be known, by substituting the power law of eq. (3.35) in place of the quantity ρ/σ_r^3, the Jeans equation can be rewritten in the following way (Dehnen and McLaughlin, 2005; Ludlow et al., 2011):

$$\left(\gamma' - \frac{6}{5}\beta'\right) + \frac{2}{3}\left(\gamma + \alpha + \frac{3}{2}\right)\left(\gamma + \frac{2}{5}\alpha + \frac{6}{5}\beta\right) = -\frac{3}{5}k_s x^{2-2\alpha/3} y^{1/3} \tag{3.36}$$

where the primes indicate the derivative with respect to $\ln x$, $y = \rho/\rho_s$, $x = r/r_s$, $k_s = 4\pi G\rho_s r_s^2/\sigma_r^2$. The latter is a measure of the velocity dispersion in units of the "natural" velocity scale of the halo at r_s. For the moment let us consider the simple case $\beta(r) = 0$. In this case three central asymptotic behaviours are possible:

1. a steep central cusp, $\gamma \to 2\alpha - 6$
2. a central hole where $y(0) = 0$
3. a "critical" solution with a shallow central cusp, $\gamma \to -2\alpha/5$

The only physically meaningful solution is the third one, which is the limiting case where the radius of the central hole solution goes to zero, and corresponds to a maximally mixed state for given halo binding energy and mass (Taylor and Navarro, 2001).

The same conclusions are reached if the velocity anisotropy is not constant, provided that $\beta(r) \to 0$ as $r \to 0$.

In left panel of Fig. 3.2 we show that when an appropriate exponent of the PPSD is chosen, the Jeans equation allows to recover the density profile with the same accuracy of a direct fit of the Einasto profile to a simulated halo. This means that Einasto and power-law PPSD models provide an equally good description of the spherically averaged structure of simulated CDM haloes. α and Γ constitute equivalent measures of the shape of the mass profile.

In order to compute the density profile, a velocity dispersion must be assumed, as above explained. The choice is not totally arbitrary, as the velocity anisotropy $\beta(r)$ and the logarithmic slope $\gamma(r)$ of the density profile appear to be related to each other (Hansen and Moore, 2006; Ludlow et al., 2011). The right panel of Fig. 3.2 shows the $\beta - \gamma$ relation for three simulated halos. Hansen and Moore (2006)

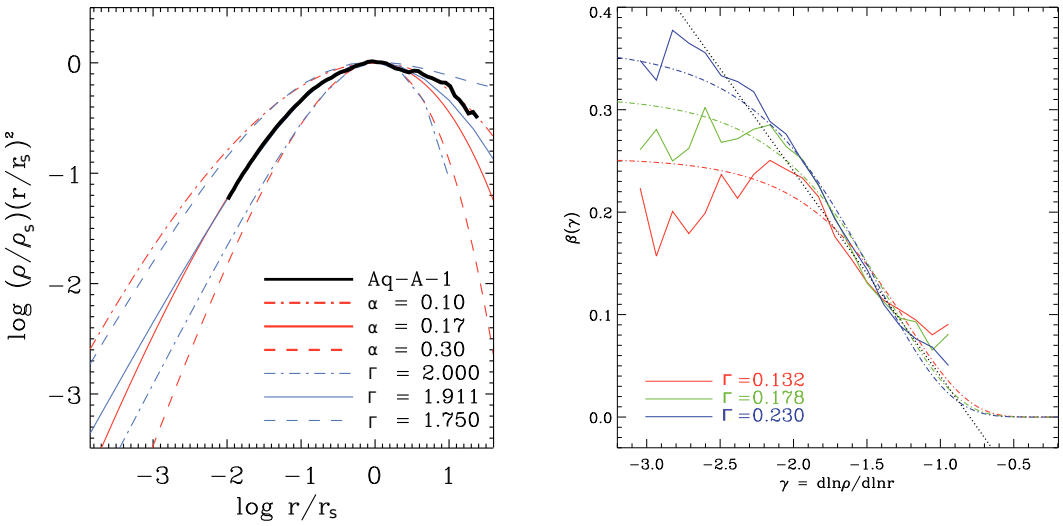

Figure 3.2: *Left panel:* Density profile of the billion-particle Aq-A-1 (Ludlow et al., 2011) simulated halo (black line) and the profiles obtained by setting the free exponent Γ of the Einasto profile and the free exponent α of the PPSD in order to highlight the similarity of the two descriptions. *Right panel:* Velocity anisotropy – density logarithmic slope relation for three halos characterized by different Einasto parameters. The dotted line is the relation provided by Hansen and Moore (2006) and the dot–dashed line is the one by Ludlow et al. (2011). Modified from Ludlow et al. (2011).

identify a universal relation between these two quantities, shown as dot–dashed line in Figure 3.2:

$$\beta(\gamma) = -0.2(\gamma + 0.8) \tag{3.37}$$

shown as a dotted line in Fig. 3.2. In the outer regions of the halos a departure from the relation of Hansen and Moore (2006) suggests that a more complex relation might hold. Ludlow et al. (2011) propose the following parametric relation:

$$\beta(\gamma) = \frac{\beta_\infty}{2}\left(1 + erf(\ln[(A\gamma)^2])\right) \tag{3.38}$$

where β_∞ and A depend on the Einasto shape parameter Γ (see Ludlow et al., 2011, for a quantitative presentation of these parameters).

Studying the time evolution of this relation, Hansen and Moore (2006) find that neither the density profile gives rise to the velocity anisotropy profile nor vice versa.

Instead, they find that the $\beta - \gamma$ relation is in place as soon as a given density profile exists and has reached a certain degree of stability, meaning that these two profiles are the result of a fundamental process happening during the structure build–up.

3.7 Mass content from dynamical information

We have seen in Sect. 2.6 that the measure of the mass of cosmological objects, such as clusters of galaxies, has proven to be an important tool for cosmological applications. The mass is not a direct observable, and many techniques have been developed to infer it by measuring observable quantities. Two methods that are widely used to infer the mass profile of galaxy clusters are the X-ray and the lensing techniques. The former makes use of the observations of the X-ray emission of the hot intracluster plasma (ICM hereafter). The lensing technique makes use of the relativistic effect of distortion of the trajectories of light emitted by distant background galaxies due to the mass of the observed cluster. These two methods have anyway some limitations. In the case of the X-ray technique, the limitation comes from the usual assumption that the plasma of the cluster is in hydrostatic equilibrium, and the cluster approximately spherically symmetric with no important recent merger activity. As for the lensing technique, its limitation is that it allows to compute the projected mass only, and this includes all the line-of-sight mass contributions. The complementarity of the different techniques is a great advantage to reliably constrain the mass of a cluster.

Here we want to discuss another kind of information, coming from the kinematics of the galaxies belonging to the observed cluster. In fact, the potential well of the cluster, due to the mass, is the main driver of the orbital motion of the galaxies which, in the absence of mutual interactions, can be treated as test particles in the gravitational potential of the cluster, which is considered as a system mainly made of non–collisional matter. The kinematics of galaxies therefore carries the information about the mass content of the cluster. The motion takes place in a 6-dimensional phase space, but the observations are able to capture only 3 of these dimensions, namely 2 for the position and one for the line of sight (*los*, hereafter) velocity. This is one of the most important limitations of the mass estimate through the observation of the kinematics of galaxies, and the techniques presented here have to face this issue.

Observed los galaxy velocities must be corrected for the effect of cosmological expansion to obtain the velocities that pertain to the motion of the galaxies in their cluster. In fact, the measured redshift of a cluster galaxy is due to the combined

effect of the cosmological expansion and of the peculiar motions of galaxies within the cluster. Harrison and Noonan (1979) pointed out that in order to properly measure the velocity dispersion of the cluster galaxies, a correction must be applied to the observed velocities. A galaxy emitting light with wavelength λ_g will be observed having a redshift $1 + z_{obs} = \lambda_{obs}/\lambda_g$, where λ_{obs} is the observed wavelength. We can think to split the information travel from the galaxy to the final observer in two steps: first from the galaxy to an observer at the center of the cluster, and then from this observer to the final one. If λ_{cl} is the wavelength observed by the observer at the center of the cluster, the redshift of the galaxy for the final observer reads:

$$1 + z_{obs} = \frac{\lambda_{obs}}{\lambda_{cl}} \frac{\lambda_{cl}}{\lambda_g} = (1 + z_{cos})(1 + z_{pec}) \tag{3.39}$$

In the non relativistic case, the peculiar velocity can be approximated as $z_{pec} = v_{pec}/c$, and the previous equation becomes:

$$z_{obs} = z_{cos} + \frac{v_{pec}}{c}(1 + z_{cos}) \tag{3.40}$$

Therefore to obtain the velocity of a cluster galaxy in the cluster rest-frame from the observed galaxy redshift z_g, one must use the following expression:

$$v_{rf} = c \cdot (z_g - z_{cos})/(1 + z_{cos}) \tag{3.41}$$

The rest-frame velocities are those that must be used in the determination of the cluster mass by the methods described below.

3.7.1 Dispersion Kurtosis method

The first method to infer the mass content of a galaxy cluster we present here is the so–called *Dispersion–Kurtosis technique*, hereafter shortened to DK, first introduced by Łokas (2002). It relies on the joint fit of the second and fourth moment of the velocities and the related moments of the Jeans equation.

In order to solve the Jeans equation (eq. 3.17), a profile for the velocity anisotropy $\beta(r)$ must be assumed. Many profiles have been proposed (see, e.g. Osipkov, 1979; Merritt, 1985; Mamon and Łokas, 2005a; Tiret et al., 2007), although simulations seem to suggest that for an ideal cluster of galaxies, obtained by stacking many simulated clusters, the velocity dispersion profile is almost constant in the inner regions ($r < r_s$), with a value near the isotropy, and becoming slightly radially anisotropic outward (see, e.g. Wojtak et al., 2013). A collapsing perturbation has

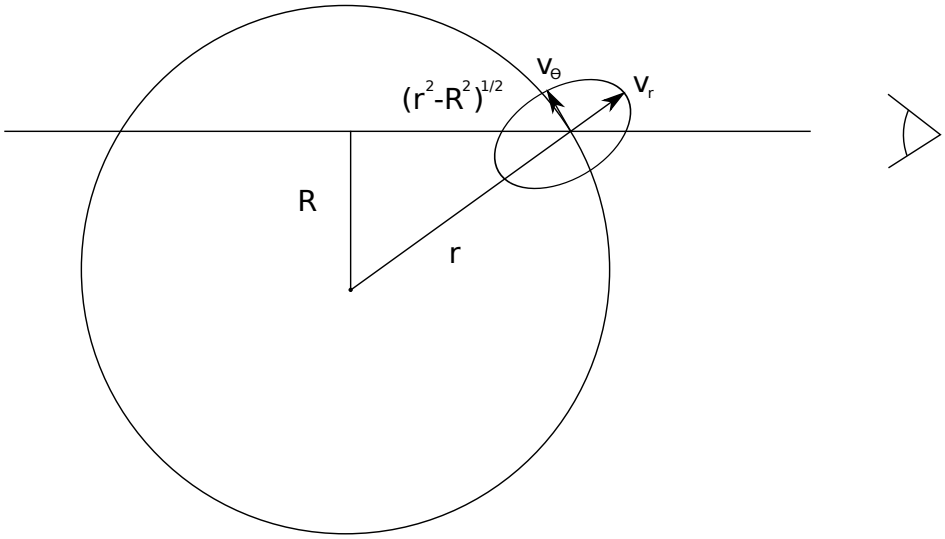

Figure 3.3: Configuration of the observation of the los velocity dispersion at a projected radius R in a spherical system.

the internal region characterized by radial motions toward the center. The radial motion far from the cluster follows the Hubble flow, moving away from the cluster. Therefore we expect that in between these two regimes a region with no radial motion is present. The radius at which this happens is called *turnaround radius*, for which $\sigma_r = 0$. If we model the system with eq. (3.17), the Hubble flow is not included, therefore we can impose that $\sigma_r \to 0$ for $r \to \infty$. The solution of the Jeans equation assuming $\beta = const$ is (Łokas, 2002):

$$\nu\sigma_r^2 = r^{-2\beta} \int_r^\infty r^{2\beta} \nu \frac{d\Phi}{dr} dr \tag{3.42}$$

Although this equation provides a solution, it is of no help in a real case, as the radial velocity dispersion is not an observable quantity. Such quantity can be related to the line–of–sight velocity dispersion σ_{los}, which is an observable by definition, via the following relations:

$$\Sigma(R) = 2 \int_R^\infty \frac{\nu r dr}{\sqrt{r^2 - R^2}} \tag{3.43}$$

$$\Sigma(R)\sigma_{los}^2 = 2 \int_R^\infty \frac{\nu\sigma_r^2 r dr}{\sqrt{r^2 - R^2}} \tag{3.44}$$

where Σ is the surface number density, and we have adopted the convention of r for the 3D radii and R for the projected distance from the center, see Fig. 3.3. These are Abel integrals, and the solutions are provided in Binney and Tremaine (1987) to be the following:

$$\nu(r) = -\frac{1}{\pi}\int_r^\infty \frac{d\Sigma}{dR}\frac{dR}{\sqrt{R^2-r^2}} \tag{3.45}$$

$$\nu(r)\sigma_r^2(r) = -\frac{1}{\pi}\int_r^\infty \frac{d(\Sigma\sigma_{los}^2)}{dR}\frac{dR}{\sqrt{R^2-r^2}} \tag{3.46}$$

Unfortunately eq. (3.44) and (3.46) are only valid for the specific case $\beta(r) = 0$. In general, the knowledge of σ_{los} alone is not enough for solving these equations. In fact, systems with different densities and velocity anisotropies can produce identical σ_{los} profile. Considering higher order moments of the velocity distribution can break this degeneracy.

In the case of fourth–order moments there are three different components, $\overline{v_r^4}, \overline{v_\theta^4} = \overline{v_\phi^4}, \overline{v_r^2 v_\theta^2} = \overline{v_r^2 v_\phi^2}$, related by two higher order Jeans equations (Merrifield and Kent, 1990). In Łokas (2002) it is shown that for a generic velocity anisotropy, constant with radius, the distribution function can be constructed from an energy–dependent function multiplied by some function of angular momentum:

$$f(E, L) = f_0(E)L^{-2\beta} \tag{3.47}$$

where $E = -\Phi - v^2/2$ is the energy and $L = (v_\theta^2 + v_\phi^2)^{1/2} r$ the momentum. By using this expression for the distribution function, it is possible to demonstrate that the two Jeans equations for the fourth–order moments reduce to the following:

$$\frac{d}{dr}(\nu\overline{v_r^4}) + \frac{2\beta}{r}\nu\overline{v_r^4} + r\nu\sigma_r^2\frac{d\Phi}{dr} = 0 \tag{3.48}$$

the solution being:

$$\nu\overline{v_r^4} = 3r^{-2\beta}\int_r^\infty r^{2\beta}\nu\sigma_r^2(r)\frac{d\Phi}{dr}dr \tag{3.49}$$

The line–of–sight fourth moment can be obtained by projection (an expression is provided in Łokas, 2002), and scaled by the dispersion to obtain the *kurtosis*:

$$\kappa_{los}(R) = \frac{\overline{v_{los}^4}(R)}{\sigma_{los}^4(R)} \tag{3.50}$$

A joint fit of the velocity dispersion and of the kurtosis allows to break the degeneracy and recover the density profile of the system. We want to remind that in order to apply this technique, the system is assumed to be spherical symmetric and in equilibrium. This technique is applied to a galaxy cluster in Chapter 5. More details are provided in that section.

3.7.2 MAMPOSSt

The MAMPOSSt technique, recently developed by Mamon et al. (2013), performs a maximum likelihood fit of the distribution of tracers of the system dynamics in projected phase space, assuming models for the mass profile, the anisotropy profile, the projected number density profile and the 3D velocity distribution.

The distribution function can be parametrized as follows:

$$f(\vec{r},\vec{v}) = \nu(r) f_v(\vec{v}|r) \tag{3.51}$$

where $\nu(r)$ is the number density profile. It is possible to write the los velocity distribution in cylindrical coordinates, where $\vec{e_z}$ is the axis along the los while $\vec{e_\perp}$ and e_ϕ are the axes perpendicular to the los. Referring to Fig. 3.3 for the notation, the los velocity distribution at a point distant r from the center, and with projected distance R, reads:

$$h(v_z|R,r) = \left(\frac{dN}{dv_z}\right) = \int_{-\infty}^{+\infty} dv_\perp \int_{-\infty}^{+\infty} f_v(v_z, v_\perp, v_\phi) dv_\phi \tag{3.52}$$

Integrating along the los, the surface number density is obtained:

$$\begin{aligned} g(R,v_z) &= \Sigma(R)\langle h(v_z|R,r)\rangle_{los} \\ &= 2\int_R^\infty \frac{r\nu(r)}{\sqrt{r^2-R^2}} h(v_z|R,r) dr \\ &= 2\int_R^\infty \frac{r\nu(r)}{\sqrt{r^2-R^2}} \left(\frac{dN}{dv_z}\right) \int_{-\infty}^{+\infty} dv_\perp \int_{-\infty}^{+\infty} f_v(v_z, v_\perp, v_\phi) dv_\phi \end{aligned} \tag{3.53}$$

In the DK method the distribution function was parametrized in terms of energy and angular momentum (see eq. 3.47). In MAMPOSSt a different approach has been followed. By assuming the form of the 3D velocity distribution, eq. (3.53) provides the analytical expression of the surface density distribution of tracers in projected phase space (PPS hereafter) through a single integral. In Mamon et al.

(2013) the explicit computation for a Gaussian distribution function shows that $h(v_z|R,r)$ depends on $\sigma_r(r)$, and the radial velocity dispersion becomes:

$$\sigma_r^2 = \frac{1}{\nu(r)} \int_r^\infty \exp\left[2\int_r^s \beta(t)\frac{dt}{t}\right] \nu(s)\frac{GM(s)}{s^2} ds \tag{3.54}$$

Once the velocity anisotropy and mass profiles are assumed, using eq. (3.46), the projected number density profile, eq. (3.53), is fully specified. If we define ΔN_p to be the number of objects within a given radial range, the probability density of observing an object at position (R, v_z) of PPS is:

$$q(R, v_z) = \frac{2\pi R g(R, v_z)}{\Delta N_p} \tag{3.55}$$

The parameters of the assumed profiles are obtained by using a maximum likelihood estimation, that is by minimizing:

$$-\ln \mathcal{L} = -\sum_{i=1}^{n} \ln q(R_i, v_{z,i}|\vec{\theta}) \tag{3.56}$$

for the N–parameter vector $\vec{\theta}$, where n is the number of data points.

We remind that this technique assumes the system to be in equilibrium and spherically symmetric. In Sect. 5.4 we apply this technique to a real, observed cluster. More details are provided in that section.

3.7.3 The caustic technique

The caustic technique, introduced by Diaferio and Geller (1997), is different from the other two methods, as it does not require dynamical equilibrium, but only spherical symmetry. In projected phase space, member galaxies tend to gather together, with a characteristic trumpet shape in the (R, v_{los}) plane (see Fig. 3.4). Measuring the velocity amplitude $\mathcal{A}$ of the galaxy distribution gives information about the escape velocity of the system. In turn, the escape velocity is related to the potential.

We shall now briefly describe how this technique works. If we assume a spherically symmetric system, the escape velocity is $v_{esc}(r) = \sqrt{-2\phi(r)}$, where $\phi(r)$ is the gravitational potential. Because of the meaning of escape velocity, it is unlikely for a galaxy having velocity greater than v_{esc} to be a member of the cluster. In the left panel of Fig. (3.4) the PPS of a simulated cluster is shown. The amplitude $\mathcal{A}$

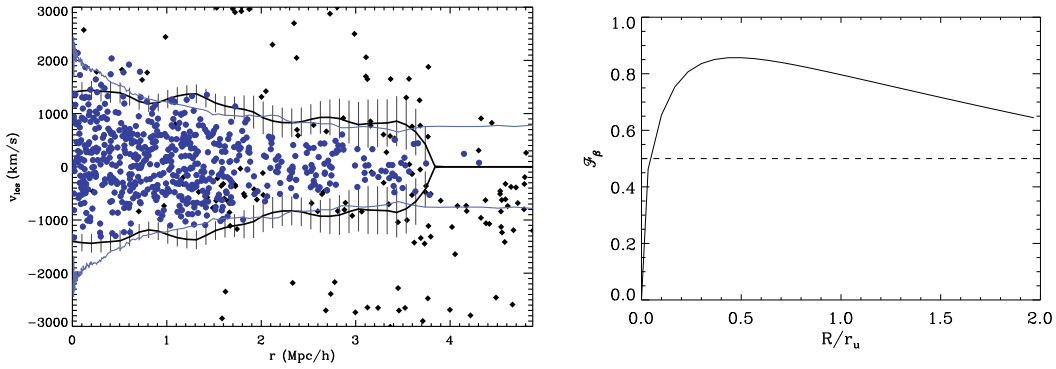

Figure 3.4: *Left panel:* phase space diagram of a simulated cluster. The black lines with $1-\sigma$ error bars and the cyan lines are the estimated and true caustics respectively. The symbols are the particles used as tracers of the internal dynamics; the blue dots are the bound particles. [After Serra and Diaferio (2013)]. *Right panel* Radial profile of $\mathcal{F}_\beta$ for a stacked sample of galaxies. The horizontal dashed line shows the commonly used value $\mathcal{F}_\beta = 0.5$. [After Biviano and Girardi (2003)].

of the caustic is a measure of the average component along the los of the escape velocity at that projected distance from the center:

$$\mathcal{A}^2(r) = \langle v^2_{esc,los} \rangle \tag{3.57}$$

For a cluster with no rotation $\langle v^2_\theta \rangle = \langle v^2_\phi \rangle = \langle v^2_{los} \rangle$, and the velocity can be expressed as $\langle v^2 \rangle = \langle v^2_{los} \rangle g(\beta)$ where:

$$g(\beta) = \frac{3 - 2\beta(r)}{1 - \beta(r)} \tag{3.58}$$

By combining eq. (3.57) and (3.58) follows:

$$-2\phi(r) = \langle v^2_{esc}(r) \rangle = \mathcal{A}^2(r) g(\beta) \tag{3.59}$$

The mass of an infinitesimal shell of matter is:

$$Gdm = G4\pi r^2 \rho(r) dr = -2\phi(r)\mathcal{F}(r) dr \tag{3.60}$$

where:

$$\mathcal{F} = \frac{-2\pi G \rho(r) r^2}{\phi(r)} \tag{3.61}$$

The mass profile is obtained by integrating eq. (3.60):

$$GM(<r) = \int_0^r \mathcal{A}^2(r)\mathcal{F}_\beta(r)dr \tag{3.62}$$

where $\mathcal{F}_\beta(r) = \mathcal{F}(r)g(\beta)$. Formally, determination of the mass profile would require knowledge of both $\rho(r)$ and $\beta(r)$. To overcome this problem, $\mathcal{F}_\beta = const$ is usually assumed, an assumption based on the analysis of cluster-size halos from cosmological numerical simulations (see Diaferio and Geller, 1997; Diaferio, 1999). In this case eq. (3.62) reads:

$$G(M < r) = \mathcal{F}_\beta \int_0^r \mathcal{A}^2(r)dr \tag{3.63}$$

Such strong assumption was first suggested in Diaferio (1999), who proposes the value $\mathcal{F}_\beta = 0.5$. Serra et al. (2011) correct this value to 0.7, while Biviano and Girardi (2003) show the $\mathcal{F}_\beta(r)$ profile obtained as a smooth approximation of the result obtained by Diaferio (1999) for a ΛCDM cosmology (see right panel of Fig. 3.4). $\mathcal{F}_\beta = const$ appears to be a good assumption except in the innermost regions of the clusters. Provided that $\mathcal{F}_\beta = const$, the exact value does not alter the mass profile. Therefore quantities depending on the profile shape, like the scale radius, are not affected by the particular choice of the value of $\mathcal{F}_\beta$.

It is worth noting two important aspects of this technique. Unlike the DK and MAMPOSSt techniques above described, the caustic method does not require the system to be in equilibrium, but only to be spherically symmetric. For this reason it allows to investigate the regions beyond the virial radius. In Sect. 5.4 we apply this technique to a real, observed cluster. More details are provided in that section.

4

Phenomenology of galaxy clusters

The simplest definition of galaxy cluster is that of an overdensity in the number of galaxies. In fact galaxy clusters can contain up to some thousands galaxies, moving in the potential well of the cluster with velocities of hundreds of $km\,s^{-1}$ on a scale of hundreds kpc. Such a definition can be misleading, as nowadays clusters are known to be mainly ($\sim$ 80%) composed by DM, which is not directly observable but whose presence drives the physical processes we can observe, e.g. the luminosity of galaxies, the X–ray emission of the hot plasma or the lensing distorsion. These processes and the detection of them is discussed in the next sections. Around $\sim$ 15% of cluster mass is in the form of a hot plasma called Intracluster Medium (ICM). Only $\sim$ 5% of the mass is made of stars forming galaxies.

In this Chapter we present the methods to detect clusters and to infer their mass. In fact in order to build a sample of galaxy clusters to study these objects, one needs an efficient method to identify clusters over a wide redshift range and an observable estimator or "proxy" of the cluster mass. Once the observational methods have been reviewed, the properties of cluster galaxies and the physical processes taking place in these systems are discussed. In fact although the baryon content is very small, on scales smaller than $10\,Mpc$ gas–dynamical processes become fundamental in shaping galaxy formation and evolution and consequently the observational properties of these structures. For this reason it is important to understand the baryonic processes taking place in the clusters, and how they can be observed to obtain information on the system.

4.1 Optical identification of clusters

The first modern method of galaxy clusters identification and classification was implemented by Abell in 1958 (Abell, 1958). His method was based on eye identification of apparent overdensities of galaxies in the photographic plates of the Palomar Observatory Sky Survey. The first release contained 2712 clusters, and it constitutes the basis of the largest galaxy cluster spectroscopic survey completed so far, the ESO Nearby Abell Cluster Survey (ENACS, Katgert et al., 1996, 1998).

Nowadays catalogues are based on automated procedures and do not rely on the observer's eye anymore. Many cluster identification methods have been developed. We now summarize the most widely used methods in the optical band.

The most used one, when redshift information is not available, is the *Matched Filter* (Postman et al., 1996). The spatial and luminosity distribution of observed galaxies in a given field is modelled as the sum of two contributions, one from the field and another from the cluster:

$$D(R,m) = b(m) + N_c N(R)\Phi(m) \tag{4.1}$$

the $b(m)$ is the background galaxy count as a function of the magnitude m, and the other term is the one relative to the cluster and is composed by three terms: $N(R)$ is the projected radial profile of the cluster galaxies as a function of the projected radial distance from the cluster center, R, $\Phi(m)$ is the differential cluster luminosity function (LF hereafter) and N_c is a measure of the number of cluster galaxies, the so–called *richness*. The best parameters are chosen by a Maximum Likelihood procedure aimed at minimizing the difference between the observed galaxy distribution, $D(R,m)$, and the model. The Matched Filter algorithm has been used on data from the ESO Imaging Survey (Olsen et al., 1999), the Sloan Digital Sky Survey (SDSS, Bahcall et al., 2003), the 2 Micron All Sky Survey (2MASS, Kochanek et al., 2003), and several other surveys (see Biviano, 2008, and references therein).

If, on the other hand, the redshift information is available, other methods are used, the most commonly adopted being the *friends–of–friends* percolation algorithm (FoF hereafter, Huchra and Geller, 1982; Geller and Huchra, 1983). The idea of this method is to link galaxies to one another according to their distance within a physical overdensity. Galaxies more distant than the chosen linking length are not considered part of the cluster. Of course the linking length is an arbitrary parameter, and different choices are possible (see, e.g. Huchra and Geller, 1982; Eke et al., 2004; Berlind et al., 2006). The FoF method has been applied many times in

spectroscopic surveys, e.g. the Center for Astrophysics Redshift Survey (Geller and Huchra, 1983), the Southern Sky Redshift Survey (Maia et al., 1989), the Las Campanas Redshift Survey (Tucker et al., 2000), the ESO Slice Project survey (Ramella et al., 1999), and, more recently, the SDSS, the Two Degree Field Galaxy Redshift Survey (2dFGRS), and the 2-Micron All Sky Redshift Survey (2MRS) (see Biviano, 2008, and references therein).

Another method used to identify clusters is the *Cluster Red Sequence* (CRS, Gladders and Yee, 2000). This method relies on the observational evidence that all rich clusters up to $z \sim 1$ have a well defined sequence of red galaxies in the color–magnitude diagram. The color bands are chosen so as to bracket the $4000\mathring{A}$ break feature of galaxy spectra. At $z > 1$ the $4000\mathring{A}$ break feature is shifted in the infrared (IR) frequencies, hence IR observations are needed. Selecting galaxies around the red-sequence, it is possible to exclude most of background and foreground galaxies, which are redder and bluer respectively. On the other hand in unrelaxed, low–mass clusters the red sequence may be not established yet, making the CRS technique not efficient. In particular, at high redshift, the fraction of early–type galaxies (ETG) decreases, making the red sequence less easily detectable.

The maxBCG method (Bahcall et al., 2003) is based on the fact that the brightest cluster galaxy (BCG) generally lies in a narrow region of the color–magnitude plot (see, e.g. Gladders and Yee, 2000). In Koester et al. (2007) this method has been applied to SDSS data, providing a catalogue composed of 13823 clusters out to $z = 0.3$. The comparison with the results of the MF method shows that about 80% of the systems are identified by both maxBCG and MF.

A geometrical approach is instead adopted in the *Voronoi Galaxy Cluster Finder* (VGCF, Ramella et al., 2001). The projected space is partitioned according to the Voronoi tessellation, so as each cell contains only one galaxy. The inverse of the cell area defines the local galaxy density. Clusters are defined as ensembles of adjacent cells with a density above a given threshold. This method is non-parametric, therefore it does not require a priori hypotheses on the cluster properties, such as cluster size, density profile, or shape. Barrena et al. (2005) showed that the VGCF method is even better than the MF method.

Mixed methods that exploit the advantages of different methods have been implemented, and are presented in the review by Biviano (2008).

4.2 Observational methods

In order to use galaxy clusters for cosmological analysis, cluster catalogues must provide an estimate of the mass of these objects. If a considerable amount of telescope time is available, the most commonly used techniques are the X–ray technique, the SZ and the lensing one as well as the analysis of the dynamics of cluster galaxies. The lensing technique makes use of the relativistic phenomenon of distortion of light paths due to the presence of a mass distribution, providing a direct measure of the gravitational well. Two techniques, the X–ray and the SZ, makes use of the physical processes taking place in the gas of the ICM. Understanding the physics of this medium appears therefore a fundamental issue for a correct estimate of the mass content in galaxy clusters. Another widely used technique makes use of the motion of the galaxies within the cluster, which is regulated by the gravitational potential of the system. This technique is not discussed here, as it is the main topic of this thesis, and has been presented in more detail in section 3.7.

If it is not possible to rely on sufficient telescope time, one must consider a robust definition of cluster mass proxies, that have minimal and well understood scatter across the full mass and redshift ranges of interest. If gravity is the dominant process in the assembly of galaxy clusters, the latter are self–similar, and simple scaling relations hold between basic cluster properties and the total mass (Kaiser, 1986). Baryonic processes take place in galaxy clusters, therefore the study of the scaling relations turn out to be useful not only for cosmology, but also for the comprehension of the physics of the ICM. We summarize the most widely used proxies in optical and X–ray observations, and refer the reader to Giodini et al. (2013) for a recent review.

4.2.1 Gravitational lensing

Overdensities in the matter distribution perturb the trajectories of photons that are emitted by distant galaxies. The effect reminds the distortion of images when observed through a piece of glass with a spatially varying index of refraction: the images look distorted and magnified. This phenomenon, called *gravitational lensing*, is a relativistic effect and is used to determine the projected mass of clusters. In fact the deflection is due to the presence of the mass distribution of the cluster, which is called *the lens*, therefore it is a direct measure of the gravitational potential, independent of the dynamical state of the system. For a recent review on the use of gravitational lensing to derive the mass profile of galaxy clusters we refer the

reader to Hoekstra et al. (2013).

When the deflection of light is large, multiple images of the same source are observed, and are useful to constrain the mass profile of the inner regions of clusters. This is the case of the so–called *strong lensing* regime. By this effect it is possible to put strong constraints to mass models in the inner regions of galaxy clusters, but it rarely allows model-independent reconstructions of mass profiles (Bartelmann et al., 2013).

If the deflection is not enough to produce multiple images, it is still possible to detect the coherent alignment of the images produced by the distortion of the light paths. We will refer to this case as *weak lensing* (WL) regime. The ellipticity imprinted by the presence of the mass distribution along the line of sight is characterised by the local strength of the gravitational field or *shear* γ, and by the scaled surface mass density or *convergence* κ, which is related to the surface density of the lens (the cluster) via the following relation:

$$\kappa = \frac{\Sigma}{\Sigma_{crit}} \tag{4.2}$$

where Σ_{crit} is the following term:

$$\Sigma_{crit} = \frac{c^2}{4\pi G} \frac{D_s}{D_l D_{ls}} \tag{4.3}$$

D_s being the angular distance to the source background galaxy, D_l the angular distance to the lens (cluster), and D_{ls} the angular distance from the lens to the source galaxy. Hence, the lensing signal depends on the redshifts of both the lenses and the sources. It is convenient to define the *reduced shear* g:

$$g = \frac{\gamma}{1-\kappa} \tag{4.4}$$

The effect of the gravitational distortion of light rays is to map a circular source into an ellipse having axis ratio $(1-|g|)/(1+|g|)$ and to magnify it by a factor $\mu = (1-\kappa)^{-2}(1-|g|^2)^{-1}$. As first shown by Kaiser and Squires (1993), it is possible to express the surface density in terms of the observable shear, allowing to reconstruct the mass distribution.

Rarely galaxies are circular. Elliptical shapes are in fact observed both due to their intrinsic shape or because we usually do not see disc galaxies face–on (van Uitert et al., 2012). Therefore to detect the ellipticity due to the WL effect, it is customary to average over many background sources. This statistical approach

implies that weak lensing has an intrinsic resolution set by the number density of galaxies. Typically (Bartelmann et al., 2013) a number density $n \simeq 30\, arcmin^{-2}$ and a total number $N \simeq 10$ galaxies are needed, resulting in a resolution of $\theta > \sqrt{N/n\pi} \simeq 20''$.

The first step to reconstruct the mass profile via the WL technique is the detection of background galaxies, whose ellipticity is measured after correcting for smearing due to the point–spread function (PSF) (see, e.g. Clowe and Schneider, 2002). The measured shear must then be converted into a measurement for the convergence κ. In Fig. 4.1 a map of κ is shown as solid dark contours. Both the shear

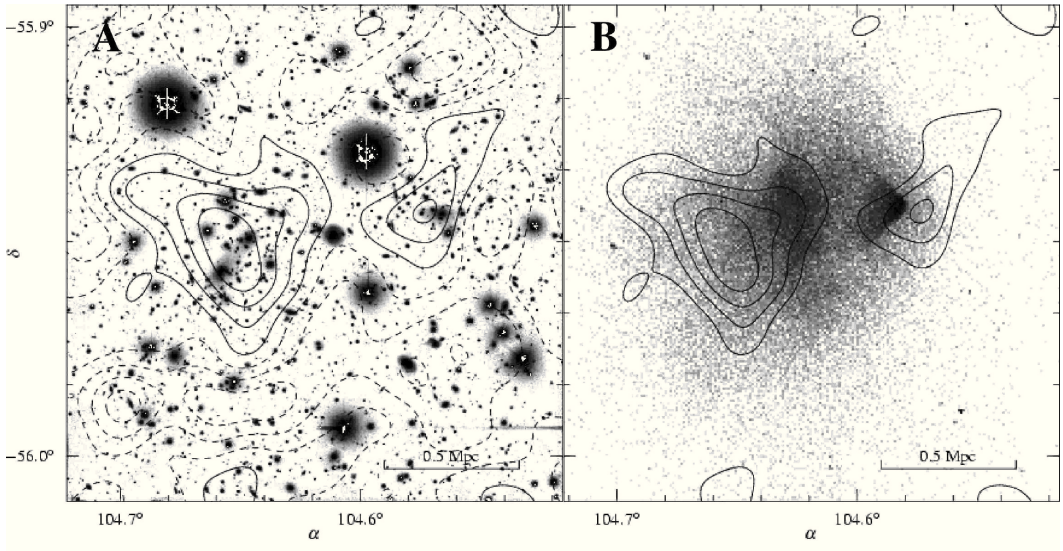

Figure 4.1: *Left panel:* Gray-scale I-band VLT image of the interacting galaxy cluster 1E 0657–558 used to measure the galaxy shapes for the background galaxies. Black contours are the weak–lensing mass reconstruction, solid contours referring to positive mass, dashed contours for negative mass, and the dash-dotted contour for the zero-mass level, which is set such that the mean mass at the edge of the image is zero. *Right panel:* Gray-scale Chandra X-ray image with the same weak-lensing contours as in left panel. [After Clowe et al. (2004)].

and the convergence are combinations of various second derivatives of the surface potential, and therefore the Fourier transform of the shear can be converted into the Fourier transform of κ by multiplying for the appropriate wavenumbers. In this kind of measurements what is actually measured from the background galaxies is

the reduced shear g. An iterative approach is therefore adopted, by assuming an initial κ map (usually $\kappa = 0$). g is corrected with this map to γ which is then transformed to a new κ map, and so on (Seitz and Schneider, 1995). This procedure typically converges in a few iterations (Clowe et al., 2004), providing an estimate of κ in the field relative to the level of κ at the edge of the image, which is unknown. For this reason, in this way it is not possible to measure the mass of the cluster reliably. It is therefore customary to assume a surface mass model for the cluster and convert this into a κ profile, and then into a profile for the reduced shear, which is compared with the azimuthally averaged shear profile from the data, as shown in Fig. 4.2. Different mass profiles are usually considered, typically

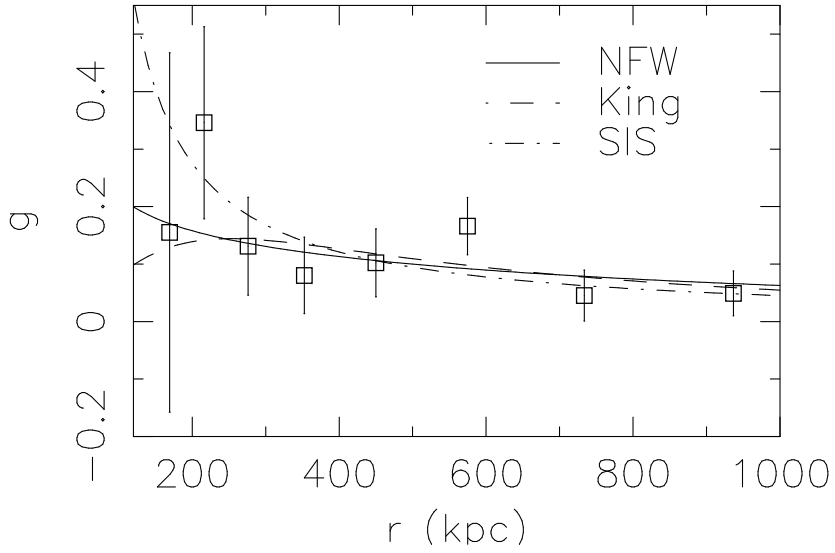

Figure 4.2: Reduced shear profile for the interacting galaxy cluster 1E 0657–558. The reduced shear profiles for the best–fit NFW (solid line), King (dashed line), and SIS (dash-dotted line) models are shown. [After Clowe et al. (2004)].

an NFW model (Navarro et al., 1996), the singular isothermal sphere (SIS) and a King model (Binney and Tremaine, 1987), and then integrated to obtain the surface density profile.

The dominant source of uncertainty in WL mass reconstruction is the interpretation of the signal, due to the fact that clusters are neither round nor described by simple parametric density profiles. The bias in the mass estimate can be reliably quantified using numerical simulations. Another source of uncertainty lies in the

fact that WL is sensitive to all matter along the line–of–sight. The structures present along the path of light therefore are a source of noise, which must be taken into account.

The WL analysis relies on the knowledge of the distance of the lens and the sources. Therefore the uncertainty on source redshifts is a dominant source of bias. Thanks to deep, multi-wavelength, wide-angle surveys the redshifts of intermediate redshift clusters are now well measured. However, in the case of high–redshift clusters, the lack of source redshift information is still a concern. Furthermore, high redshift clusters have a small number of galaxies behind them, making the WL analysis more difficult and noisy.

4.2.2 X–Ray Emission

Galaxy clusters are very bright extended X–ray sources, with luminosities of the order $10^{43} - 10^{45} erg\, s^{-1}$, the emission being due to the hot plasma of the ICM (Sarazin, 1988; Rosati et al., 2002).

The X–ray emission is the result of the interactions between ions and electrons. In particular the spectrum is characterized by a continuum due to the bremsstrahlung process and the recombination, while emission lines are due to the de–excitations of bound electrons (see, e.g. Boehringer and Werner, 2009). Collision rates of this plasma are proportional to the gas temperature and ion and electron densities, therefore the observed spectrum depends at the same time on the plasma temperature and on its chemical composition. Since the ICM is a plasma characterised by a thermal equilibrium, ionisation and recombination rates are balanced for every element. At the typical temperatures of the ICM, around $10^7 - 10^8 K$, the emission is dominated by the bremsstrahlung process, while the line emission becomes dominant for temperatures around $10^4 - 10^5 K$.

The power radiated is given by the following relation (see, e.g. Borgani, 2008):

$$\frac{dL_X}{dV} \propto \left(\frac{\rho_{gas}}{\mu m_p}\right)^2 \Lambda(T) \tag{4.5}$$

where ρ_{gas} is the gas density, μ is the mean molecular weight of the gas and m_p is the proton mass and, for the bremsstrahlung emission, $\Lambda(T) \propto T^{1/2}$. Due to the dependence on the square of the density, the X–ray emission allows to investigate the inner regions of the clusters.

If a cluster is relaxed, we can assume the ICM to be in hydrostatic equilibrium. If we also assume spherical symmetry, the pressure p of the ICM can be related to

the density of the gas ρ_{gas} via the following expression:

$$\frac{dp}{dr} = -\frac{GM(<r)\rho_{gas}}{r^2} \tag{4.6}$$

M being the mass within the radial distance r. Using the equation of ideal gas the mass profile reads:

$$M(<r) = -\frac{kTr}{G\mu m_p}\left(\frac{d\log\rho_{gas}}{d\log r} + \frac{d\log T}{d\log r}\right) \tag{4.7}$$

To recover the total mass profile from X–ray observables, different methods have been developed. For a detailed review we refer the reader to Ettori (2013).

One possibility is the use of parametric functions to model the gas density and temperature radial profiles through the observed surface brightness and spectral temperature data. In order to use the X–ray surface brightness, the latter must be PSF-corrected and deprojected into 3D emission measure profiles (see, e.g. Croston et al., 2006), and its peak is taken as the center of the cluster. Using the emissivity profile the gas density profile is obtained, accounting also for the weak dependence of the emissivity on temperature. Temperature profiles are modelled with a hot diffuse gas including metal emission lines (see, e.g. Smith et al., 2005a), then are deconvolved from the PSF blurring and either deprojected into 3D physical profiles or modelled with a functional form in 3D projected on the plane of the sky to reproduce the observed quantities. The total mass profile is then obtained through the hydrostatic equilibrium equation (HEE), eq. (4.7) (see, e.g. Pointecouteau et al., 2005; Nagai et al., 2007).

Another possibility is the widely used approach first described in Ettori et al. (2002a) and adopted in both observational (Morandi et al., 2007; Donnarumma et al., 2011; Ettori et al., 2010) and simulated datasets (Rasia et al., 2006; Meneghetti et al., 2010). A functional form, like an NFW profile, is adopted to describe the DM density profile, defined as the total mass minus the gas mass. The gas density profile is estimated from the geometrical deprojection (see, e.g. Ettori et al., 2002a) of either the measured X–ray surface brightness or the estimated normalization of the thermal model fitted in the spectral analysis. Once the mass and gas density profiles are known, the temperature profile, either 3D or projected, is obtained by inverting the hydrostatic equilibrium equation (eq. 4.7). The mass profile parameters are constrained by minimizing a χ^2 statistic comparing the temperature profile with the observed temperature measurements obtained in the spectral analysis. In Fig. 4.3 the best–fit results of the gas density and temperature profiles for an observed cluster are shown.

It is also possible to solve the HEE in a non–parametric way, by using the best–fit results on gas temperature and density of the deprojected spectra (see,e.g. Voigt and Fabian, 2006; Nulsen et al., 2010).

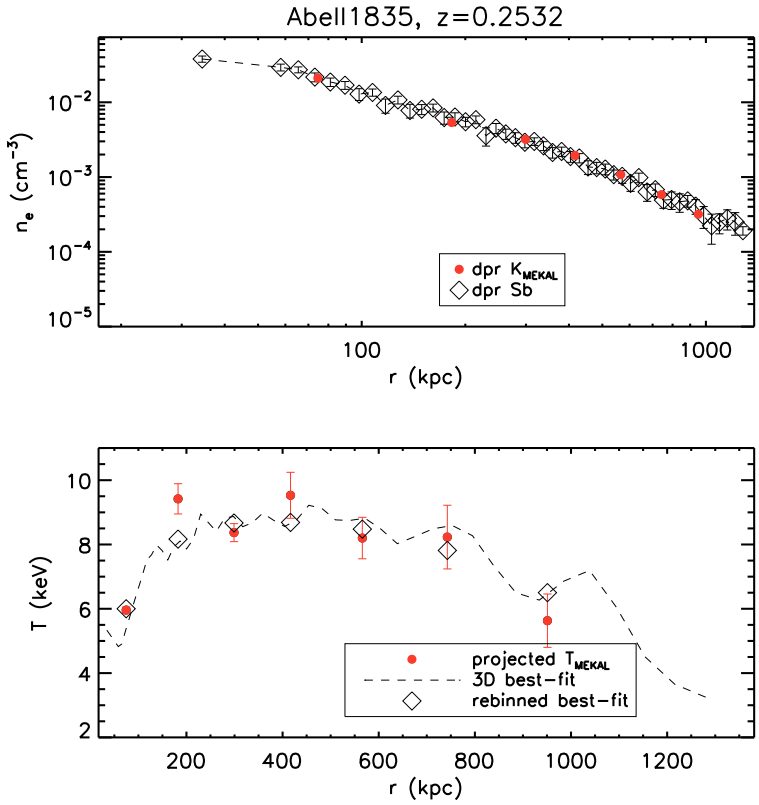

Figure 4.3: Results of the two analysis adopted for the mass reconstruction of Abell1835 by Ettori et al. (2010). *Top panel:* gas density profile as obtained from the deprojection of the surface brightness profile compared to the one recovered from the deprojection of the normalizations of the thermal model in the spectral analysis. *Bottom panel:* observed temperature profile with overplotted the best–fit model. [After Ettori et al. (2010)].

Comparing the mass estimates from X–ray analysis to those obtained via WL analysis (see Fig. 4.4), it appears that X–ray masses within R_{500} are on average 10% lower than the WL ones (Mahdavi et al., 2013), although the bias seems to disappears when restricting the analysis to cool–clusters only, characterized by a

more relaxed dynamical state. On the other hand, non–cool–core clusters present a bias up to 20%. Tensions between X–ray and WL masses in disturbed objects, and agreement in relaxed objects, have been reported also in other works (see, e.g. Böhringer et al., 2010; Donnarumma et al., 2011; Umetsu et al., 2012). Non–cool–core clusters have proven to be useful laboratories also when comparing the results from dynamical analysis. In Ettori et al. (2002b,a) the discrepancies were largest between X–ray and dynamical analyses in such non–relaxed clusters, highlighting the importance of the assumption of equilibrium in both kinds of analyses. Galaxy clusters are in fact dynamically young systems, and mergers can cause departures from equilibrium, as well as perturbing the geometry of the systems, making the spherical symmetry assumption not appropriate (Limousin et al., 2013).

4.2.3 Thermal Sunyaev–Zel'dovich effect

When photons of the CMB travel through a galaxy cluster, there is a small probability for them of being inverse–Compton scattered by electrons of the ICM. Since the CMB temperature has a temperature $T \simeq 2.73K$, while the ICM can have temperatures of order $10^8 K$, if such scatter occurs, the CMB photons increase their energy. This can be detected as a change in the CMB intensity and spectrum.

In the regime $E_\gamma \ll m_e c^2$, the energy variation of a single photon is:

$$\frac{\Delta E}{E} \simeq \frac{k_B T_e}{m_e c^2} \tag{4.8}$$

This photon will experience a number of collision given by $N = n_e \sigma_T$, where n_e is the electron's number density and σ_T the Thompson cross–section. The overall effect is quantified by the *Comptonisation parameter* y, given by:

$$y = \int_{los} n_e \frac{k_B T_e}{m_e c^2} \sigma_T dl \tag{4.9}$$

where the integral is along the line of sight. The observable effect in the CMB spectrum is the decrease of intensity at frequencies lower than $\nu_{SZ} \simeq 218 GHz$, and an increase for frequencies higher than ν_{SZ}, as shown in Fig. 4.5 (see, e.g. Carlstrom et al., 2002). It is possible to demonstrate (see Carlstrom et al., 2002, and references therein) that the y parameter is related to the change in the CMB temperature T_{CMB} given by:

$$\frac{\Delta T}{T_{CMB}} = f(x) y \tag{4.10}$$

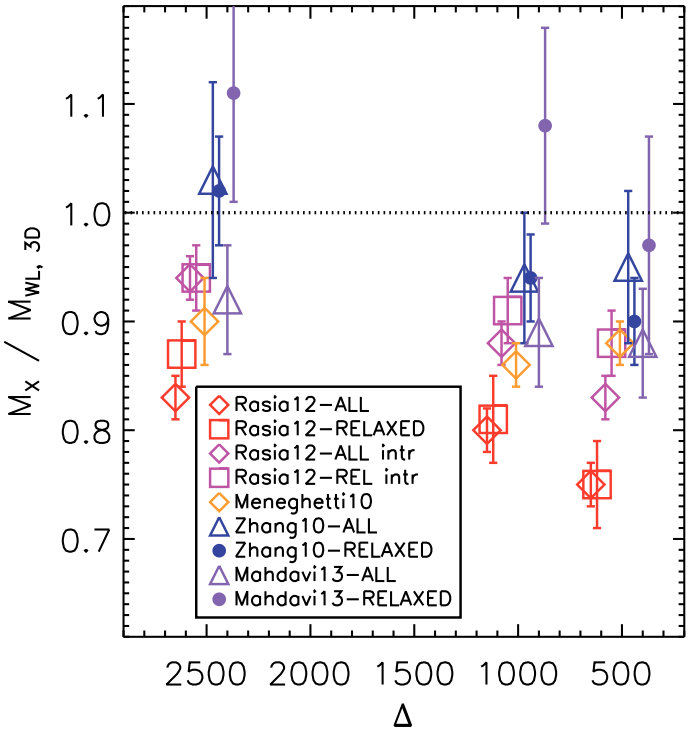

Figure 4.4: Comparison between X–ray and WL mass determinations from recent work based on both observed (Zhang et al., 2010; Mahdavi et al., 2013) and simulated (Meneghetti et al., 2010; Rasia et al., 2012) clusters. [After Ettori (2013)].

where $f(x)$ is a function of the dimensionless frequency $x = h\nu/k_B T_{CMB}$:

$$f(x) = \left(x \frac{e^x + 1}{e^x - 1} - 4 \right) (1 + \delta_{SZ}(x, T_e)) \tag{4.11}$$

where $\delta_{SZ}(x, T_e)$ is the relativistic correction to the frequency dependence. It is important to notice that the temperature change does not depend on redshift. This is one of the most important features of the SZ effect, making the use of it an important tool for the study of the high redshift Universe.

The Compton y–parameter integrated within a region centered on a cluster is

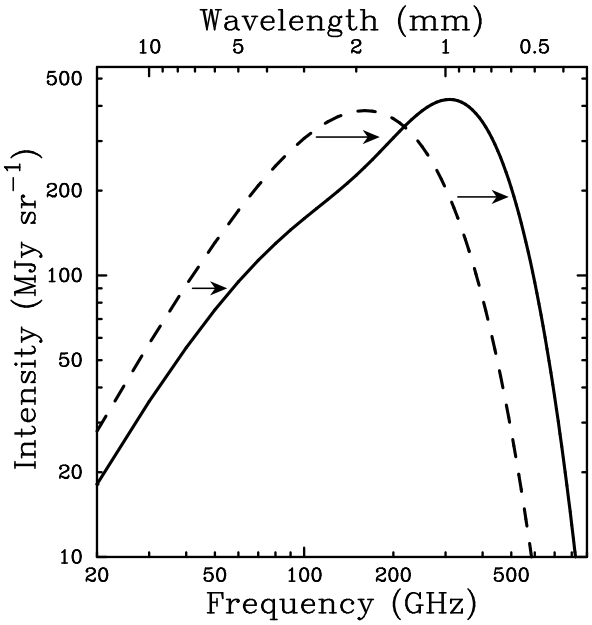

Figure 4.5: CMB spectrum, undistorted (dashed line) and distorted by the Sunyaev-Zel'dovich effect (solid line). In order to illustrate the effect, the SZE distortion shown is for a fictional cluster 1000 times more massive than a typical massive galaxy cluster. [After Carlstrom et al. (2002)].

called the Y parameter:

$$Y = \int y d\Omega = \frac{1}{D_A^2} \frac{k_B \sigma_T}{m_e c^2} \int dl \int n_e T_e dA = \frac{1}{D_A^2} \frac{\sigma_T}{m_e c^2} \int P(r) dV \qquad (4.12)$$

where D_A is the angular distance and A is the area perpendicular to the line of sight. The volume integral of pressure P is the total thermal energy content of the ICM, which should directly trace the depth of the potential well (Carlstrom et al., 2002). Therefore a tight scaling relation between the SZ signal Y and cluster mass is expected. The quantity YD_A^2 is called *intrinsic y-parameter*, as it removes the distance dependence on the previous equation. A strong correlation is indeed found between the SZ signal and the mass of clusters, as shown in fig. 4.6 (see, e.g. Rines et al., 2010; Marrone et al., 2012).

The main problem with SZ is that the signal is intrinsically very faint. The first generation of SZ telescopes needed long time of observation to get a significant SZ

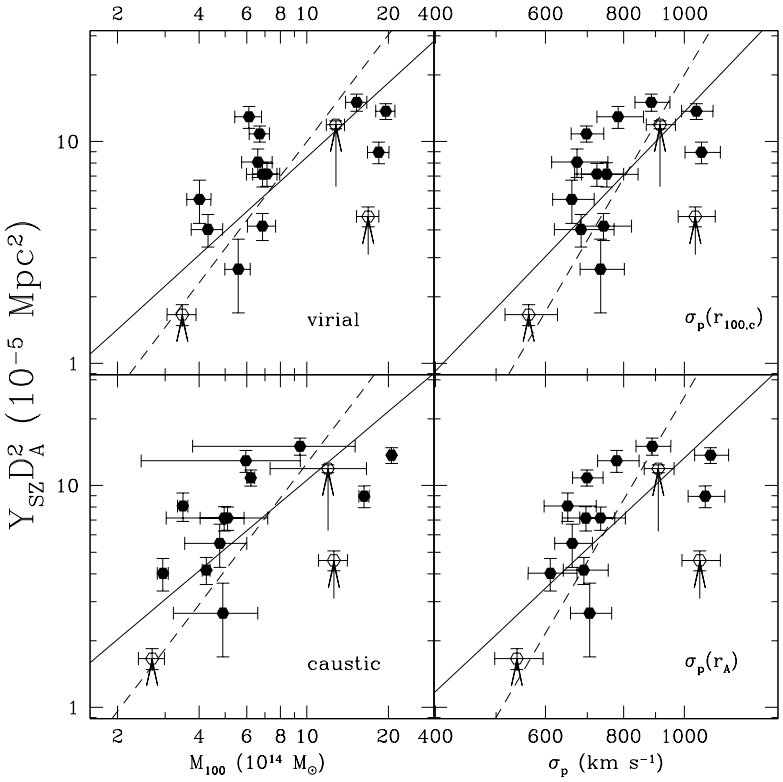

Figure 4.6: Comparison between the integrated SZ parameter, corrected for the angular distance term, and the cluster mass or the velocity dispersion of 15 from HeCS (Rines et al., 2010). *Left panels:* SZ data vs. M_{100} estimated from the virial theorem (top) and the caustic mass profile (bottom). Solid and open points refer to data obtained from different works (see Rines et al., 2010, for more details). The dashed line shows the slope of the scaling predicted from numerical simulations: $Y_{SZ} \propto M_{100}^{1.6}$ following the results by Motl et al. (2005), while the solid line is the fit of the data.*Right panels:* SZ data vs. projected velocity dispersions measured for galaxies inside the caustics and (top) inside r_{100} estimated from the caustic mass profile and (bottom) inside the Abell radius $2.14 Mpc$. The dashed line shows the scaling predicted from simulations $Y_{SZ} \propto M_{100}^{1.6}$ following the results by Motl et al. (2005) along with the scaling $\sigma \propto M^{0.33}$ by Evrard et al. (2008). The solid line shows the fit to the data. [After Rines et al. (2010)].

detection of a single known cluster. The new generation, like Planck, SPT, ACT and SZA, are much more sensitive (AMI Consortium et al., 2012). Another limitation of the SZ effect is its capacity of measuring only the projected mass along the line of sight, therefore the estimate is contaminated by the small objects in background and foreground that are not resolved in other wavelengths and can bias the mass estimate.

4.2.4 Cluster mass proxies

For optical studies the most used mass proxies are the richness, N, and the luminosity, L. Both N and L are measured in a certain magnitude range and out to a certain radius from the cluster center, summing up, respectively, the number and the luminosities of galaxies.

If m_c is the magnitude below which the sample is complete, the total cluster luminosity is obtained by extrapolating the contribution of the galaxies with $m > m_c$. The number of galaxies dn of a given luminosity is given by $dn = \Phi(l)dl$, where l is the luminosity and $\Phi(l)$ is the so–called *luminosity function* (LF). The most widely used one is the Schechter LF (Schechter, 1976):

$$\Phi(l)dl = \Phi_*(l/l_*)^\alpha \exp(-l/l_*)d(l/l_*) \tag{4.13}$$

where l is the galaxy luminosity, l_* and Φ_* are the characteristic luminosity and number density, respectively, and α is the faint-end power-law exponent. In order to obtain the total luminosity within a given distance from the center, the luminosity density profile must be determined, then Abel inverted via the equivalent of eq. (3.45) and finally extrapolated to the desired radius with a suitable fitting function, like an NFW profile (eq. 3.31).

In the same way one can proceed to obtain the richness within a given distance from the center. Although conceptually equal, when extrapolating the richness one must be careful, since faint galaxies are much more numerous than bright galaxies, while their integrated contribution to the total luminosity is only marginal.

Another commonly used method to obtain an estimate of the mass of a cluster using optical data is the use of the virial theorem (Zwicky, 1933) applied to the observed velocities of cluster galaxy members. The virial theorem, eq. 3.26, can be recast in the following form:

$$M = \frac{3\pi}{G} P \sigma_v^2 R_h \tag{4.14}$$

where G is the gravitational constant, σ_v is the line-of-sight velocity dispersion of cluster galaxies, and R_h is the harmonic mean radius of the projected spatial

distribution of cluster galaxies:

$$R_h = \frac{n(n-1)}{2\sum_{i>j} R_{ij}^{-1}} \tag{4.15}$$

where R_{ij} is the projected distance between two cluster galaxies, and n is the number of cluster galaxies. The factor 3π corrects for projection effects, while P is the so–called *surface pressure term*, needed when the entire cluster is not included in the observed sample (see,e.g. Girardi et al., 1998).

This method is based on the assumption that galaxies are distributed in the same way the mass is. Differences in the two distributions have been observed (see, e.g. Biviano et al., 2002). If the analysis is restricted to the ETG, the two profiles are very similar and the resulting mass estimate more reliable, provided that the clusters are not too far from dynamical equilibrium (Biviano et al., 2006; Hicks et al., 2006; Johnson et al., 2006).

As for the X–ray observations, a relation between the luminosity L_X and the temperature T of the ICM is known (see, e.g. Markevitch, 1998; Arnaud and Evrard, 1999; Maughan, 2007): $L_X \propto T^{\alpha} E(z)$ where $E(z)$ is given by eq. (2.18), and according to Pratt et al. (2009), $\alpha \simeq 2.5 - 3$ at cluster scales and even steeper and with large scatter for galaxy groups (Osmond and Ponman, 2004). If the assumption of hydrostatic equilibrium holds, then the relation linking the mass and the temperature is $M \propto T^{3/2} E^{-1}(z)$. Combining these two relations, we obtain the relations between the X–ray luminosity and the mass (see Fig. 4.7):

$$M \propto L^{3/4} E^{-7/4}(z) \tag{4.16}$$

Kravtsov et al. (2006) introduced a new quantity, the Y_X parameter, that demonstrated to be a very robust mass proxy being directly proportional to the cluster thermal energy. It is defined as follows:

$$Y_X = M_{gas} T_X \tag{4.17}$$

Its scaling relation with M_{500} is characterized by an intrinsic scatter of only $5 - 7\%$ at fixed Y_X, regardless of the dynamical state of the cluster. This robustness has been confirmed in a number of recent works, both on the observational side (see, e.g. Arnaud et al., 2007; Pratt et al., 2009) and on the theoretical one (see, e.g. Rasia et al., 2011; Fabjan et al., 2011) by means of cosmological hydrodynamical simulations.

In order to reduce the scatter in the relations between total mass and observables, combinations of X–ray observables are sought (Ettori et al., 2012; Ettori, 2013):

$$M \propto L^{\alpha} M_{gas}^{\beta} T^{\gamma} \tag{4.18}$$

For the particular conditions and values of the parameters we refer the reader to Ettori (2013). In such paper it is shown that the use of this generalized scaling relation allows to reliably recover the total mass of galaxy clusters, with a typical error of order $\sim 5\%$.

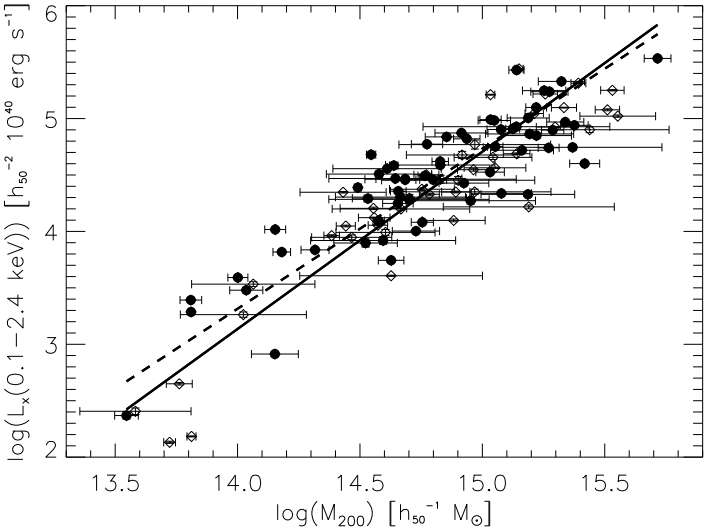

Figure 4.7: Relation between cluster mass and X–ray luminosity for a sample of 106 galaxy clusters. [After Reiprich and Böhringer (2002)].

The relations between the mass and the proxy can be biased because of some physical processes taking place in clusters. A way to recognize the presence and the effect of these phenomena is the comparison among different proxies. An interesting example is the comparison between the optical information coming from the velocity dispersion σ_v of galaxies and the X–ray luminosity L_X of the cluster. It is known that there is a population of clusters for which the mass derived from L_X is smaller than the one obtained from σ_v. These are called *X-ray underluminous clusters*. On the other hand there is also a population whose mass estimated from

L_X is bigger than the mass from σ_v. These are called *X–ray bright clusters* (Bower et al., 1997; Popesso et al., 2007). These differences shed light on the dynamical stage of these systems. The X–ray underluminous clusters are thought to be at an early stage of their dynamical evolution, while the opposite holds for the X–ray bright systems, where dynamical processes lead an important role. In fact dynamical friction reduces the velocity of galaxies and tidal interactions transfer part of the kinetic energy of galaxies to internal energy.

4.3 Properties of cluster galaxy populations

The study of the properties of cluster galaxies and the relations with their environment as well as with redshift allows to constrain the mechanisms of galaxy formation and evolution.

In galaxy clusters, galaxies with different morphologies are present. In particular, most of cluster galaxies are *early type galaxies* (ETGs), at odds with what is observed in the field, where *late type galaxies* (LTGs) constitute the most common type of galaxies (Whitmore et al., 1993; Postman et al., 2005). Even inside the cluster itself, different morphological types are distributed differently: the fractions of Es and S0s increase with increasing local density and the fractions of S and Irr decrease (see, e.g. Postman and Geller, 1984). This is the so-called *morphology–density relation* (MDR in the following). Because of the correlation between density and distance from cluster center, the MDR can be thought as a relation between the morphological type and the distance from the cluster center. The MDR seems to be in place already at $z \simeq 1$ in massive clusters, as shown by Postman et al. (2005); Smith et al. (2005b), while in low–mass, irregular clusters the MDR does not appear to hold at redshift above ~ 0.5 (Dressler et al., 1997).

Another characteristic feature of galaxies is the color. It has been observed that cluster galaxies tend to lie in a narrow region of the color vs. magnitude diagram (see, e.g. Bower et al., 1992). This is the so–called *color–magnitude relation* (CMR in the following) and appears to be in place even at high redshift (e.g. Andreon et al., 2008; Strazzullo et al., 2013). The scatter of the CMR appears to increase with clustercentric distance and at the faint end of the LF (Smail et al., 1998; Pimbblet et al., 2006). The CMR varies with redshift, the red galaxy fraction decreasing at increasing redshift. This effect is known as *Butcher–Oemler effect* after the first authors who noticed it (Butcher and Oemler, 1978).

Galaxies in clusters present a difference also in their luminosity with respect to field galaxies. Compared to the LF of field galaxies, the LF of cluster galax-

ies presents a steeper faint-end slope, a brighter characteristic magnitude, with a plateau at intermediate luminosities, as shown in Fig. 4.8 for the Coma cluster. Within the cluster, the LF depends on the clustercentric distance. In fact the ratio

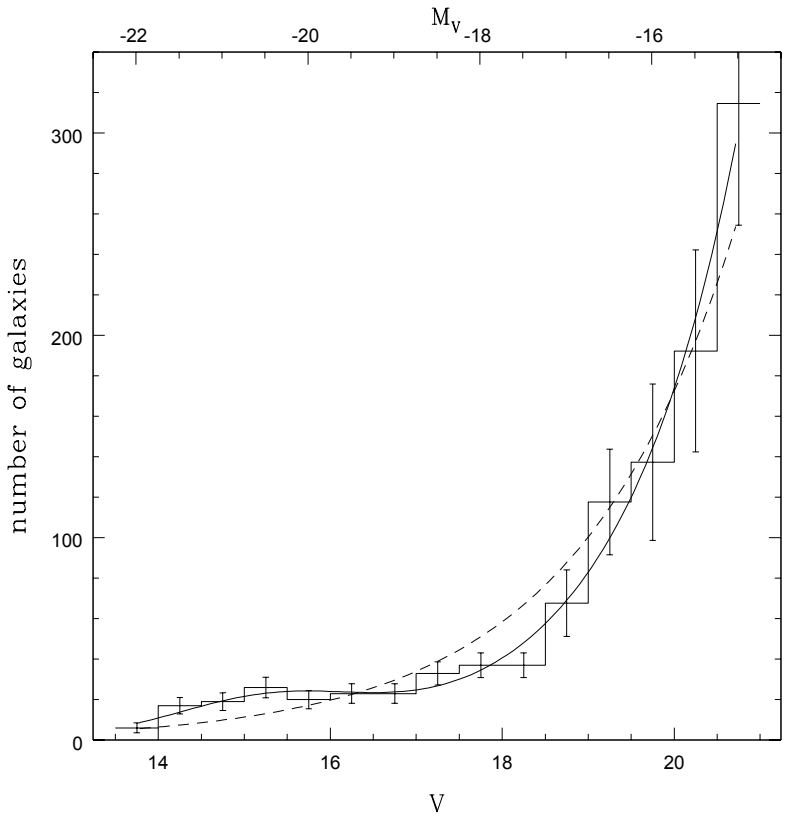

Figure 4.8: The LF of the Coma galaxy cluster. It is possible to notice the excess of bright galaxies relative to a Schechter function (dashed line), a steep faint-end upturn and a plateau at intermediate luminosities. The solid line is a Gaussian+Schechter fit to the data. [After Lobo et al. (1997)].

between the number of bright giants and faint dwarfs increases toward the center, an effect known as *luminosity segregation* (Capelato et al., 1980). This issue is however still debated and studied. We refer the reader to Biviano (2008) and references therein for a more comprehensive treatment of the topic.

A peculiarity of the luminosity in the clusters is the presence of the BCG and the ICL. The former is the acronym for *Brightest Cluster Galaxy*. The BCG is a much

bigger and luminous galaxy with respect to the other ETGs (Bernardi et al., 2007) and it resides close to the bottom of the potential well of the cluster (Ramella et al., 2007). BCG luminosity correlates with the cluster's one (Lin and Mohr, 2004) and its main axis results aligned to the cluster's main axis (Struble, 1987).

The *Intra–Cluster Light* (ICL) consists of stars which are bound to the cluster potential and it is usually found in form of diffuse light around the BCG. It has low surface brightness with smooth distribution around the BCG, although it can extend to large radii. The identification of the ICL in observations is a difficult task, since the typical surface brightness of the ICL is less than 1% of the dark sky and can be contaminated by foreground and background galaxies. Moreover, the separation between the light of the BCG and the ICL is somewhat arbitrary, making the comparison between theory and observations Cui et al. (2013) difficult. ICL results useful to understand the dynamical evolution of clusters since it provides a direct probe of the past galaxy encounters that stripped the stars (see, e.g. Da Rocha et al., 2008).

4.4 Enviromental processes in clusters

Galaxy clusters are invaluable laboratories for studying astrophysical processes affecting the evolutionary properties of galaxies. Several are in fact the phenomena taking place in clusters and that are responsible for the phenomenology we presented in the previous sections. Below we summarize the most important ones, namely dynamical friction, collisions, tidal interactions and ram-pressure stripping.

A galaxy moving in a medium composed by DM particles feels a drag that slows it down due to gravitational interactions between DM particles and the galaxy itself. This force, first described by Chandrasekhar (1943), is the *dynamical friction*. DM particles tend to fall in the wake produced by the moving galaxy, creating an excess of density of matter behind the galaxy. This excess attracts gravitationally the galaxy, resulting in a drag force that is opposed to the motion of the galaxy, according to the following relation:

$$\frac{d}{dt}\vec{v}_{orb} = -4\pi G^2 \ln(\Lambda) M_{gal} \rho(< v_{orb}) \frac{\vec{v}_{orb}}{v_{orb}^3} \tag{4.19}$$

where $\rho(< v_{orb})$ is the density of background particles with velocities less than the orbital velocity v_{orb} of the galaxy, M_{gal} is the mass of the galaxy and Λ is the Coulomb logarithm (see, e.g. Chandrasekhar, 1943; White, 1976).

The effect of dynamical friction is that of making the galaxy lose energy and angular momentum, therefore sinking toward the center of the cluster and eventually merging with the central galaxy, on a time–scale (Boylan-Kolchin et al., 2008), in units of dynamical time, given by

$$\frac{\tau_{df}}{\tau_{dyn}} \propto \frac{M_{cl}}{M_{gal}} \tag{4.20}$$

where M_{cl} is the cluster mass. From the definition of dynamical time (eq. 2.3) the time–scale of the dynamical friction is

$$\tau_{df} \propto \frac{v_{gal}^3}{M_{gal}\rho} \tag{4.21}$$

Therefore dynamical friction results to be more effective in higher density environments and for more massive galaxies and not very effective when the galaxy moves fast.

Galaxies whose orbits intersect or get close to one another can collide or even merge. This causes an important morphological modification and trigger a starbust event (see, e.e. Fujita, 1998; Moore et al., 1999). The gas in the galaxies can be consumed during such event of star formation, or expelled from the system (Duc and Bournaud, 2008). The timescale for a galaxy to experience a collision event is given by

$$\tau_c \propto \frac{1}{\nu r_{gal}^2 v_{gal}} \tag{4.22}$$

where v_{gal} is the relative velocity between the two galaxies, r_{gal} is the galaxy radius, and ν is the galaxy number density (Gnedin, 2003). From the previous equation collisions appear to be more frequent in higher density environments and between larger galaxies. When the two galaxies get close enough and with low relative velocity, they can even merge, on a timescale given by

$$\tau_m \propto \frac{\sigma_v^3}{\nu r_{gal}^2 \sigma_{gal}^2} \tag{4.23}$$

where σ_v is the cluster velocity dispersion and σ_{gal} the internal velocity dispersion of the galaxy (Mamon, 1992).

The gradients of the gravitational potential in the clusters cause galaxies to be stripped by tidal forces. The external parts are progressively removed, starting

from the DM halos, while the baryonic part is more resistant as it is more compact. Tidal stripping is more effective for galaxies moving at lower velocities (Diemand et al., 2004) since they spend more time in the inner regions where tidal interactions are stronger. Tidal stripping and dynamical friction are related. On one hand, dynamical friction becomes ineffective when tidal mass-losses become important (Faltenbacher and Mathews, 2007)), because dynamical friction is more effective for more massive objects (see eq. 4.20). On the other hand, tidal mass–losses are enhanced by dynamical friction, since they are more effective in slow–moving galaxies than their fast–moving counterparts (Diemand et al., 2004). Hence, dynamical friction is likely to be more effective at the first orbit of a galaxy while tidal disruption may take several orbits.

The gas component in cluster galaxy is subject to a wind due to its motion relative to the ICM. This wind exerts a pressure that can remove the gas in the galaxy if it is sufficiently strong to overcome the gravity of the galaxy:

$$\rho_{ICM} v_{gal}^2 > \alpha \frac{G M_{gal} \rho_{gas}}{R_{gal}} \tag{4.24}$$

where ρ_{ICM} is the ICM gas density, R_{gal} is the projected galaxy radius in the direction transverse to the galaxy motion, ρ_{gas} is the 3–D galaxy gas density profile and α is a term that depends on the precise shape of the gas and mass profile of the galaxy (McCarthy et al., 2008). This process is known as *ram pressure stripping* (Gunn and Gott, 1972). There have been theoretical studies (see, e.g. McCarthy et al., 2008, and references therein) supporting this scenario, and recently observational evidences have been provided by the long tails of gas observed in some cluster galaxies (see, e.g. Crowl et al., 2005). As evident from eq. (4.24), ram pressure is more effective for a low–mass galaxy moving at high velocity in a dense ICM.

The processes so far discussed consume the gas reservoir of galaxies, causing galaxies halting the star formation. This process is called *starvation* and could partially account for the different properties of cluster and field galaxies (Balogh et al., 2000). Fig. 4.9 shows a scheme of the clustercentric radius over which each of the listed physical mechanisms may be effective at fully halting star formation or transforming the visual morphology of a radially infalling galaxy.

Studying the redshift evolution of the SFR, it appears that the typical SFR in galaxies was much higher at high redshift ($z \simeq 3$) than at $z = 0$ (Arnouts et al., 2005). In particular the most massive galaxies, mainly giant ellipticals located in galaxy clusters, are characterized by old stellar populations, being observed already in place by $z \simeq 2$. In contrast, faint field galaxies present a younger stellar

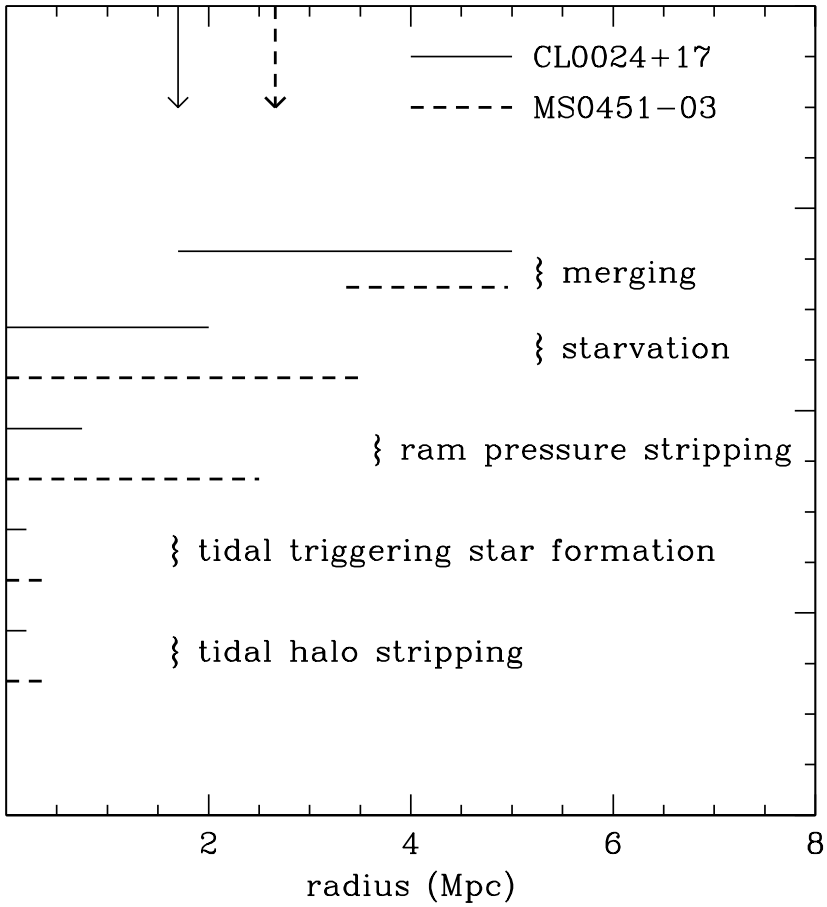

Figure 4.9: Clustercentric radius over which each of the listed physical mechanisms may be effective at fully halting star formation or transforming the visual morphology of a radially infalling galaxy. The solid and dashed lines are the estimates relative to two clusters, as indicated in the figure. Arrows indicate the virial radius of each cluster. [Modified from Moran et al. (2007)].

population (see, e.g. Treu et al., 2005; Bundy et al., 2006). This is the so–called *downsizing* scenario (Cowie et al., 1996; Gavazzi et al., 1996). The downsizing process seems at odds with the hierarchical formation of structures. Actually, the above described scenario is relative to the formation of the main stellar population, which does not necessarily coincide with the assembly of galaxy stellar mass (Fontanot et al., 2009). Feedback plays a fundamental role in the mass–dependent evolution

of galaxies. In fact mergers in high mass galaxies stimulate both star formation and active galactic nuclei (AGN). The latter are the result of gas accretion onto supermassive black holes. The effect of the AGN is to heat the inter–galactic medium (IGM) sufficiently to prevent it from condensing and forming stars, regulating the star formation rates of massive galaxies and suppressing overcooling in groups and clusters (e.g. Planelles et al., 2013).

5

Mass, velocity anisotropy and pseudo phase space density profiles of Abell 2142

5.1 Introduction

As discussed in Sect. 4.2, two methods that are widely used to infer the mass profile of galaxy clusters are the X-ray and the lensing techniques. These two methods have anyway some limitations. In the case of X-ray technique, the limitation comes from the usual assumption that the plasma of the cluster is in hydrostatic equilibrium, and the cluster approximately spherically symmetric (Ettori et al., 2002a) with no important recent merger activity (Böhringer et al., 2010). As for the lensing technique, its limitation is that it allows to compute the projected mass only, and this includes all the line-of-sight mass contributions. The complementarity of the different techniques is a great advantage to reliably constrain the mass of a cluster.

In this Thesis another kind of information is used, coming from the kinematics of the galaxies belonging to the observed cluster. The motion takes place in a 6-dimensional phase space, but the observations are able to capture only 3 of these dimensions, namely 2 for the position and one for the line of sight (los, hereafter) velocity. This is one of the most important limitations of the mass estimate through the observation of the kinematics of galaxies. To overcome this issue, most methods assume spherical symmetry.

In this section, the results of the study of the galaxy cluster Abell 2142 (A2142 hereafter), a rich galaxy cluster at $z \sim 0.09$, are presented. The great amount of

galaxy members allows us to derive the total mass profile, testing different models, as well as performing dynamical analyses deriving the anisotropy of the orbits of galaxies, and computing the pseudo phase space density profile and the $\beta - \gamma$ relation. This cluster shows evidence of some recent mergers. In fact, the X-ray emission appears to have an elliptical morphology elongated in the Northwest-Southeast direction (Markevitch et al., 2000; Akamatsu et al., 2011). The merging scenario is supported also by the presence of substructures of galaxies lying along the direction of the cluster elongation, as found in the SZ maps by Umetsu et al. (2009), lensing analysis by Okabe and Umetsu (2008) and analysis of the distribution of los velocities of Owers et al. (2011). However, analysing *XMM-Newton* images to investigate the cold fronts of A2142, Rossetti et al. (2013) exclude the mergers to be major ones, but rather of an intermediate degree.

As discussed in Sect. 3.6, the self-similarity of the DM-only haloes seems to be broken, and substituted with the pseudo phase space density $Q(r) = \rho/\sigma^3$, where ρ is the total matter density profile and σ is the 3D velocity dispersion of the tracers of the gravitational potential (Taylor and Navarro, 2001; Ludlow et al., 2010). The use of the radial velocity dispersion instead of the total one has proven to be a valid and robust alternative for the computation of the PPSD, in this case called $Q_r(r)$. The link between these two formulations of the PPSD is constrained by the velocity anisotropy (hereafter, anisotropy) of the system, which plays a non trivial role in shaping the structure of a system. The density profile and the anisotropy profile are in fact found to correlate. A best-fit relation is provided by Hansen and Moore (2006) and Ludlow et al. (2011), linking the logarithmic slope of the density profile $\gamma = d\ln\rho/d\ln r$ and the anisotropy $\beta(r)$. Hereafter we will refer to anisotropy as β or the equivalent $\sigma_r/\sigma_t = 1/\sqrt{1-\beta^2}$. We also denote the relation between anisotropy and logarithmic slope of the density profile as the $\beta - \gamma$ relation.

Throughout this section, we adopt a ΛCDM cosmology with $H_0 = 70\,\mathrm{km\ s^{-1}\ Mpc^{-1}}$, $\Omega_0 = 0.3$, $\Omega_\Lambda = 0.7$. The virial quantities are computed at radius r_{200}, where r_Δ is the radius within which the mean density is Δ times the critical density of the Universe.

5.2 The data

The photometric information has been obtained from the SDSS DR7 database[1], searching for the galaxies having $238.983 < \mathrm{RA} < 240.183$, $26.633 < \mathrm{DEC} < 27.834$

[1] http://cas.sdss.org/astro/en/tools/chart/chart.asp

and petroMag$_{r'} < 22$. The spectroscopic information has been provided by Owers et al. (2011). The full sample is composed of 1631 galaxies with both photometric and spectroscopic information. The cluster center is assumed to coincide with the X-ray center provided by De Grandi and Molendi (2002).

Two algorithms have been used to select cluster members, those of den Hartog and Katgert (1996) and Mamon et al. (2013), hereafter dHK and *clean*, respectively. Both identify cluster members on the basis of their location in projected phase-space[2]: R, $v_{\rm rest}$, using the spectroscopic values for the velocities. We adopt the membership determination of dHK, resulting in 996 members. In fact, the *clean* algorithm removes one more galaxy but it is very close to the distribution of selected members and it seems unlikely to be an interloper. Anyway, this galaxy is at ≈ 3 Mpc from the cluster center, which should make no difference in the analysis here. Fig. 5.1 shows the location of galaxies in the projected phase-space diagram and the members identification of the two methods.

The cluster mean redshift and line-of-sight velocity dispersion, as well as their uncertainties, have been computed using the biweight estimator (Beers et al., 1990) on the redshifts and rest frame velocities of the members: $\langle z \rangle = 0.08999 \pm 0.00013$, $\sigma_{\rm los} = 1193^{+58}_{-61}$ km/s.

5.2.1 The color identification

We identify the Red Sequence iteratively by fitting the $g' - r'$ vs. r' color-magnitude relation of galaxies with $r' < 19.5$ and $g' - r' > 0.7$, then selecting galaxies within $\pm 2\sigma$ of the found sequence (where σ is the dispersion around the best fit relation). We refer to the cluster members within $\pm 2\sigma$ of the Red Sequence, and those above this range, as Red Sequence galaxies, and to the cluster members more than 2σ below the Red Sequence as blue galaxies, as shown in Fig. 5.2.

5.2.2 Removal of substructures

Owers et al. (2011) found some substructures in A2142, probably groups that have been recently accreted by the cluster. These substructures can alter the kinematics of the system since they still retain memory of the infall kinematics. For this reason, we compute the mass profile of the system excluding the galaxies belonging to these substructures. In particular we consider the largest substructures in this

[2] R is the projected radial distance from the cluster center (we assume spherical symmetry in the dynamical analyses). The rest-frame velocity is defined as $v = c\ (z - \bar{z})\ /\ (1 + \bar{z})$. The mean cluster redshift $\bar{z}$ is re-defined at each new iteration of the membership selection, until convergence.

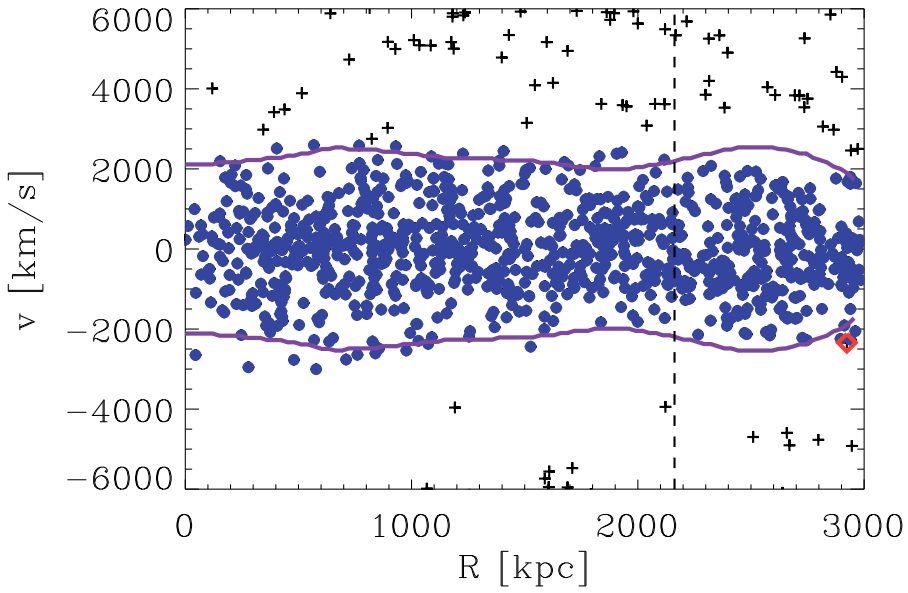

Figure 5.1: Distribution of the galaxies of Abell 2142 in the projected phase-space of projected radii and line-of-sight rest-frame velocities. Cluster members, as identified by both dHK and *clean* algorithms, are denoted by blue filled dots. The red diamond is the galaxy identified as member by dHK but not by the *clean* algorithm. The purple solid lines are the caustic, described in Sect. 5.3. The vertical dashed line locates the virial radius of the concordance model (see Sect. 5.4).

cluster, namely S2, S3 and S6, following the nomenclature of Owers et al. (2011). Therefore, we remove galaxies inside circles, the centers and radii of which are reported in Table 5.1.

5.2.3 The samples

Some of the techniques (described in Sect. 5.3) that we use to compute the mass profile of the cluster rely upon the assumption of equilibrium of the galaxy population. Red galaxies are likely an older cluster population than blue galaxies, probably closer to dynamical equilibrium (e.g. Moss and Dickens, 1977; van der Marel et al., 2000). For this reason, red galaxies constitute a better sample for the

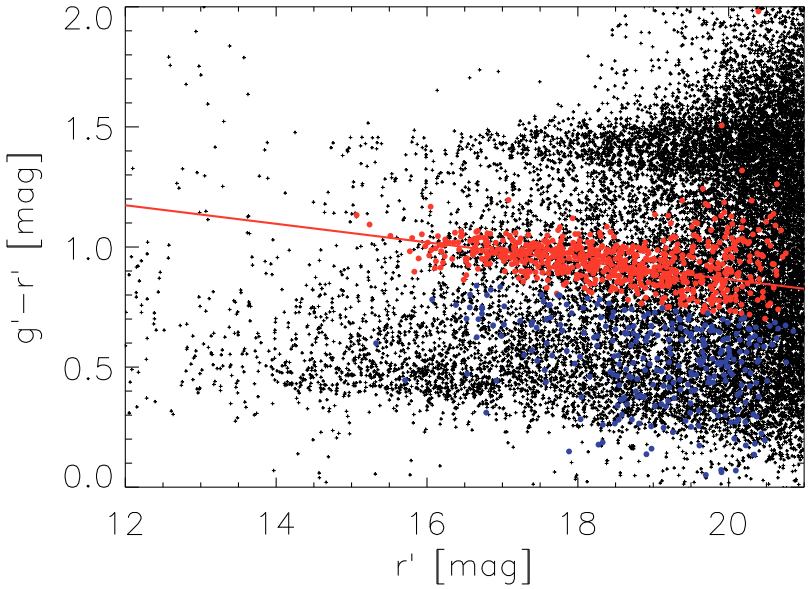

Figure 5.2: Color magnitude diagram $g' - r'$ vs. r'. Red (blue) points are relative to red (blue) member galaxies. Black points are galaxies, for which we have photometric information, that are not identified as members. The red solid line locates the Red Sequence.

application of such techniques. Among red galaxies, those outside substructures (see Sect. 5.2.2) are the most likely to be in dynamical equilibrium. We therefore use these galaxies for the determination of the mass profile.

The three samples that will be used hereafter are as follows. We will refer to the sample made of all the member galaxies to as the ALL sample. BLUE will be the sample made of blue galaxies. RED will be the sample made of red galaxies not belonging to the substructures described in Sect. 5.2.2. See Table 5.2 for a summary of the number of galaxies belonging to each sample.

5.3 The techniques

The methods we use, described hereafter, all assume spherical symmetry.

Table 5.1: Coordinates, with respect to the cluster center, and radii of the areas of the three main substructures, as found by Owers et al. (2011)

	x_c [Mpc]	y_c [Mpc]	r [Mpc]
S2	0.600	0.763	0.467
S3	2.007	1.567	0.700
S6	2.327	–0.180	0.812

Sample	n_{tot}	n_{200}
ALL	996	706
RED	564	447
BLUE	278	162

Table 5.2: For each sample, the total number of member galaxies and the number of member galaxies within r_{200}, the latter being the value of the concordance model (see Sect. 5.4), are shown.

5.3.1 Methods

DK: The dispersion kurtosis technique, hereafter shortened to DK, first introduced by Łokas (2002), relies upon the joint fit of the los velocity dispersion and kurtosis profiles of the cluster galaxies. In fact, fitting only the los velocity dispersion profile to the theoretical relation coming from the projection (see Mamon and Łokas, 2005b for single integral formulae for the case of simple anisotropy profiles) of the Jeans equation (Binney and Tremaine, 1987) does not lift the intrinsic degeneracy between mass profile and anisotropy profile determinations (as Łokas and Mamon, 2003 showed for the Coma cluster). This technique assumes spherical symmetry and dynamical equilibrium of the system, and it allows to estimate the virial mass, the scale radius and the value of the cluster velocity anisotropy, considered as a constant with radius.

MAMPOSSt: The MAMPOSSt technique, recently developed by Mamon et al. (2013), performs a maximum likelihood fit of the distribution of galaxies in projected phase space, assuming models for the mass profile, the anisotropy profile, the projected number density profile and the 3D velocity distribution. In particular, for our analysis we have used an NFW model for the mass and

the projected number density profiles, either a simplified Tiret (Tiret et al., 2007) profile or a constant value for the anisotropy profile and a Gaussian profile for the 3D velocity distribution. As in the DK method, to apply MAMPOSSt we must assume spherical symmetry and dynamical equilibrium of the system. By this method we estimate the virial mass, the scale radius of the mass density profile and the value of anisotropy of the tracers.

Caustic: The caustic technique, introduced by Diaferio and Geller (1997), is different from the other two methods, as it does not require dynamical equilibrium, but only spherical symmetry. Hence, this technique also provides the mass distribution beyond the virial radius. In projected phase space, member galaxies tend to gather together. Measuring the velocity amplitude $\mathcal{A}$ of the galaxy distribution gives information about the escape velocity of the system. In turn, the escape velocity is related to the potential, hence the mass profile: $M(r) = M(r_0) + (1/G) \int_{r_0}^{r} \mathcal{A}^2(s)\, \mathcal{F}_\beta(s)\, ds$, where $\mathcal{F}_\beta(r) = -2\pi G\,(3-\beta)/(2-\beta)\, r^2 \rho(r)/\Phi(r)$ (Diaferio, 1999).

Since the DK and MAMPOSSt techniques make use of the assumption of dynamical equilibrium of the system, the use of the RED sample allows a more correct application of those techniques, since this sample is likely to be the most relaxed sample. On the other hand, we use the ALL sample for the caustic technique.

5.3.2 Practical implementation

To compute the parameter values with the MAMPOSSt technique, we performed a Markov Chain Monte Carlo (MCMC) procedure (see, e.g., Lewis and Bridle, 2002), using the public CosmoMC code of A. Lewis.[3] In MCMC, the parameter space is sampled following a procedure that compares the posterior (likelihood times prior) of a point in this space with that of the previous point, and decides or not to accept the new point following a criterion that depends on the two posteriors (we use the Metropolis-Hastings algorithm). The next point is chosen at random from a hyperellipsoidal gaussian distribution centered on the current point. This procedure ensures that the final density of points in the parameter space is proportional to the posterior probability. MCMC then returns probability distributions as a function of a single parameter, or for several parameters together. Here, the errors on a single parameter are computed by marginalising the posterior probabilities over the other two free parameters.

[3] http://cosmologist.info/cosmomc

For the caustic technique, we use the ALL sample, since the equilibrium of the sample is not required, also considering the galaxies beyond the virial radius. To apply the caustic technique, the $\mathcal{F}_\beta$ parameter (Diaferio, 1999) must be chosen. The choice of the parameter is quite arbitrary, hence we have tested 3 different choices: the constant value 0.5, as first suggested in Diaferio (1999), the constant value 0.7 as suggested in Serra et al. (2011), and the profile described in Biviano and Girardi (2003). When using the value 0.7 and the profile of Biviano and Girardi (2003), the estimated virial masses are much greater than those obtained with the other techniques relying on the dynamics of galaxies as well as the results coming from the X-ray and the weak lensing analysis (see below). Therefore we decided to consider only the caustic technique with $\mathcal{F}_\beta = 0.5$ (the same value has been recently adopted by Geller et al., 2013). We adopt $r_0 = 0$, which relieves us from the choice of a mass at some finite radius r_0. Once we have computed the mass profile, we fit it with a NFW profile to obtain the estimate of the scale radius.

5.3.3 The scale radius of galaxy distribution

The NFW scale radius of the galaxy distribution is used as input for the DK and MAMPOSSt analyses, therefore it has been computed for the RED sample. The number density profile of the spectroscopic sample is affected by the incompleteness issue. We have corrected it using the completeness profile provided by Owers et al. (2011).

We have divided the cluster in radial bins and counted the galaxies inside each bin. In the bins where galaxies belonging to substructures have been removed and where the presence of a bright star in the cluster field caused a lack of detection, the number density of galaxies is artificially reduced. In order to take this into account, we have assumed the galaxy density in the affected regions to be equal to the mean density in the rest of the bin.

The RED galaxy number density profile is well fit by a projected NFW profile (Łokas and Mamon, 2001) with scale radius equal to 0.95 ± 0.14 Mpc. The fit is an MLE fit performed on all RED members with $\chi^2_{\rm reduced} = 0.83$. The ALL and BLUE samples are less concentrated, the values of the scale radius being 1.84 ± 0.25Mpc for the ALL sample with $\chi^2_{\rm reduced} = 2.08$ and 16 ± 11Mpc for the BLUE sample with $\chi^2_{\rm reduced} = 0.88$. In Fig. 5.3 the surface number density profiles for the different samples are shown. The scale radius for the BLUE sample is very high and is due to a very flat distribution of these galaxies.

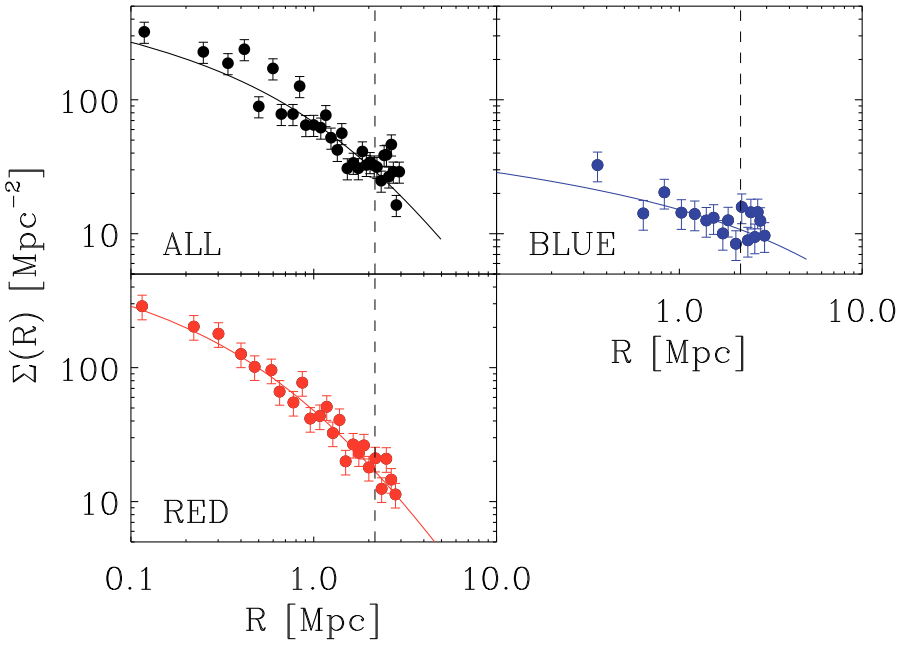

Figure 5.3: Surface number density profiles for the ALL, RED and BLUE samples, along with their best-fit projected NFW profiles. The dashed vertical line locates the virial radius of the concordance model (see Sect. 5.4).

5.4 Mass profiles

5.4.1 Mass profiles obtained from the different methods

We have used the velocities of the galaxies within r_{200} to compute the mass profile of A2142. In Fig. 5.4, the velocity dispersion profiles are shown, along with the best-fit profiles coming from the DK and MAMPOSSt analyses.

The DK technique assumes a constant value for the anisotropy, while we have chosen 2 profiles for the anisotropy model in MAMPOSSt, a constant value and a Tiret profile $\beta(r) = \beta_0 + (\beta_\infty - \beta_0)\, r/(r + r_{\rm anis})$. Here, we set $\beta_0 = 0$ (inner isotropy) and set $r_{\rm anis}$ to the scale radius of the galaxy number density profile. In Sect. 5.5, we compute the anisotropy profile for the RED sample and find that it is not compatible with a Tiret profile, therefore we made the *a posteriori* decision not to consider the result of MAMPOSSt with a Tiret profile.

We have also tried to assume different mass profiles and velocity anisotropy

models in MAMPOSSt, namely a Burkert (Burkert, 1995), a Hernquist (Hernquist, 1990) and a Softened Isothermal Sphere profile (Geller et al., 1999), all with both constant and Tiret profile for the anisotropy. The resulting estimates of virial mass and mass profile concentration are very similar to the case of NFW mass profile with constant anisotropy, with differences of the order of very few percent. We therefore only considered the NFW model for the mass profile.

The results are summarised in Tab. 5.3. Fig. 5.5 shows the detailed results of our MAMPOSSt MCMC analysis.

In Fig. 5.6, we show the mass profiles obtained from the different methods, along with the virial values of mass and radius. The results coming from the X-ray (Akamatsu et al., 2011) and weak lensing (Umetsu et al., 2009, WL hereafter) analysis are also shown.

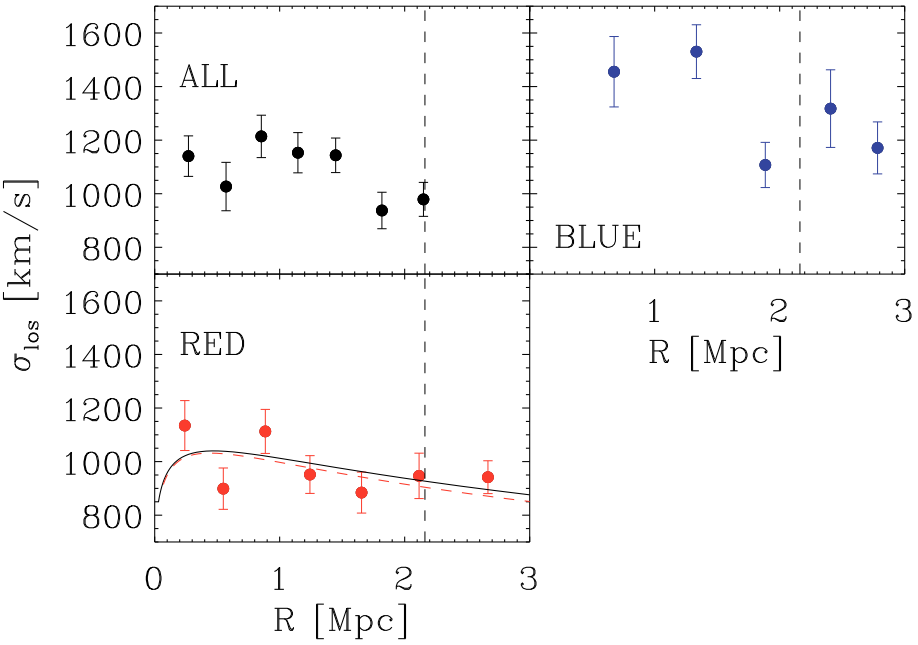

Figure 5.4: Velocity dispersion profiles for the ALL, RED and BLUE sample. For the RED sample we also show the best-fit profile coming from the DK analysis (black), and the profile computed after the MAMPOSSt analysis (dashed red). The dashed vertical line locates the virial radius of the concordance model (see Sect. 5.4).

Method	sample	M_{200} $[10^{15}\mathrm{M}_\odot]$	r_{200} [Mpc]	r_s [Mpc]	c	σ_r/σ_t
caustic ($\mathcal{F}_\beta = 0.5$)	ALL	$1.26^{+0.54}_{-0.42}$	$2.17^{+0.27}_{-0.28}$	$0.58^{+0.12}_{-0.10}$	3.7 ± 0.9	
DK	RED	$1.32^{+0.11}_{-0.21}$	$2.20^{+0.06}_{-0.12}$	$0.93^{+0.39}_{-0.10}$	2.4 ± 0.6	$1.0^{+0.20}_{-0.04}$
MAMPOSSt	RED	$1.28^{+0.14}_{-0.49}$	$2.18^{+0.08}_{-0.32}$	$0.83^{+1.73}_{-0.35}$	$2.6^{+2.0}_{-1.9}$	$1.0^{+0.50}_{-0.20}$
Kinematics		$1.31^{+0.26}_{-0.23}$	2.19 ± 0.14	0.64 ± 0.17	3.4 ± 0.9	
X-ray		$1.11^{+0.55}_{-0.31}$	$2.08^{+0.30}_{-0.22}$	0.74 ± 0.31	2.8 ± 1.1	
WL		$1.24^{+0.18}_{-0.16}$	2.16 ± 0.10	0.51 ± 0.08	4.3 ± 0.7	
Concordance model		1.25 ± 0.13	2.16 ± 0.08	0.54 ± 0.07	4.0 ± 0.5	

Table 5.3: Values of virial mass, virial radius, scale radius and concentration for different techniques, the average value of the kinematical techniques after symmetrizing the errors, and the value of the concordance model, obtained as the result of the average of all the values coming from the different techniques (see Sect. 5.5 for the average procedure). X-ray values come from Akamatsu et al. (2011), weak lensing (WL) from Umetsu et al. (2009). Both for X-ray and WL we had the values and the errors of the virial radius and the concentration: we have symmetrized these errors and propagated them to obtain the estimates of the errors on the scale radii.

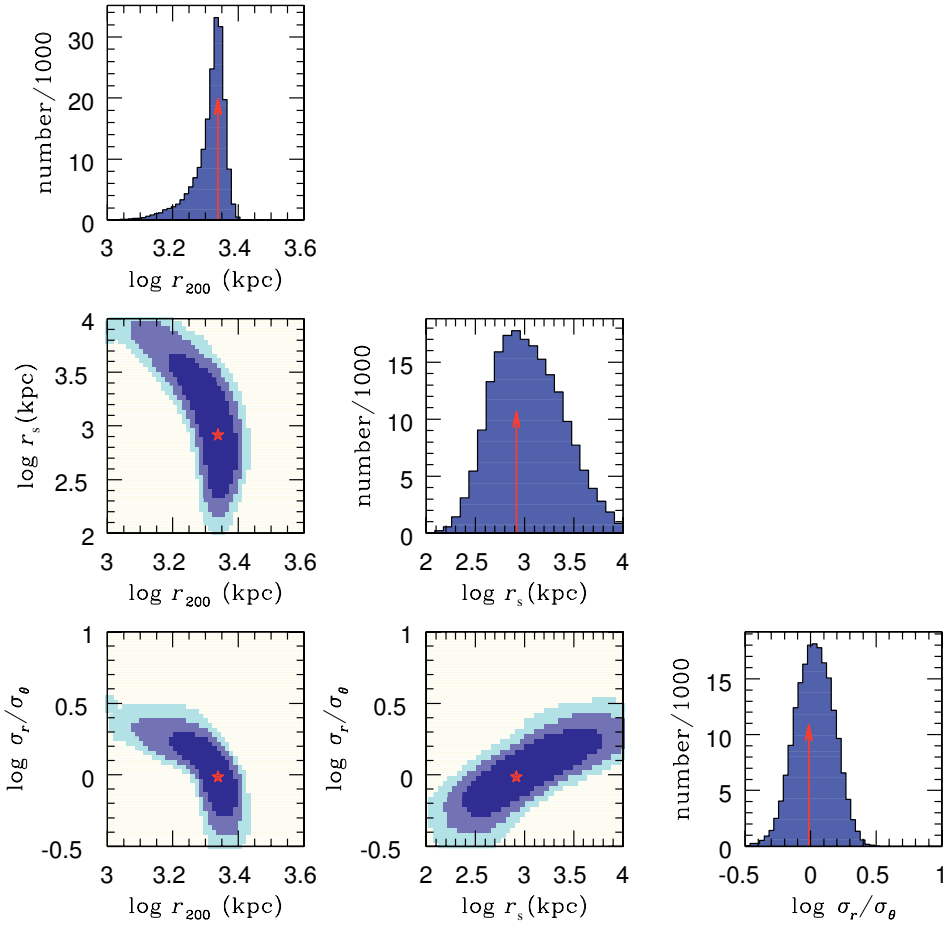

Figure 5.5: Parameter space and probability distribution functions for the virial radius, mass profile scale radius and velocity anisotropy, as found by MAMPOSSt. The coloured regions are the 1,2,3 σ confidence regions, while the red stars and the red arrows locate the best-fit values. These are based upon an MCMC analysis with 6 chains of 40 000 elements each, with the first 5000 elements of each chain removed (this is the *burn-in* phase that is sensitive to the starting point of the chain). The priors were flat within the range of each panel, and zero elsewhere.

5.4.2 Concordance mass profile

We now combine the constraints from the different mass modelling methods to build a *concordance* mass profile. We attempt to give the same weight to kinematics, X-ray and WL in the final estimate of the parameters, so we now compute a single

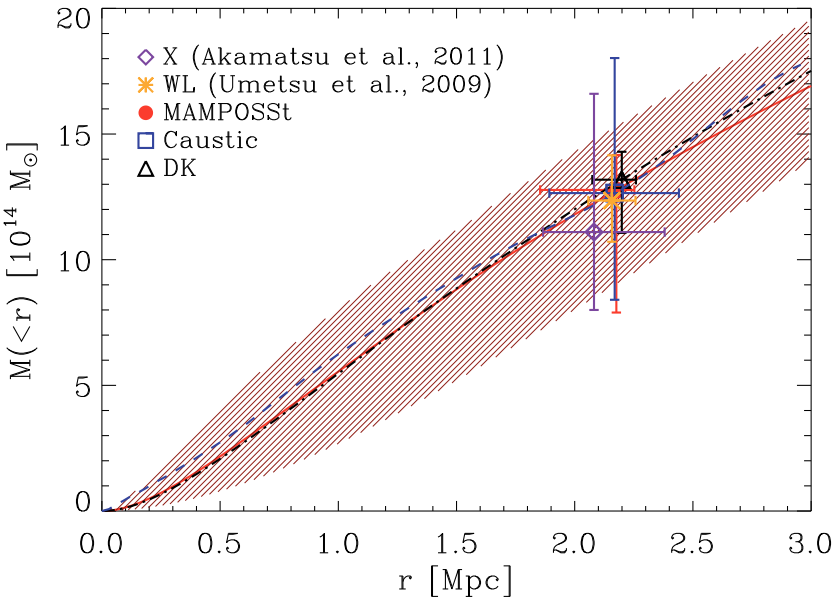

Figure 5.6: Mass profiles computed from the different methods. The black dash-dotted line and the triangle with error bars refer to DK technique, the dashed blue line and blue square to the caustic method, the solid red line and red point to MAMPOSSt. The symbols with error bars refer to the virial mass and radius. The purple diamond with error bars is the result of the X-ray analysis, while the orange star is the one coming from weak lensing analysis. The shaded area is the 1σ confidence region of the mass profile according to the MAMPOSSt results.

value coming from kinematical techniques for the scale radius, and one for the virial radius. For this we take the mean of the values r_s and r_{200} of the different methods, inversely weighting by the symmetrized errors. Since the measures of these two quantities by the various methods are not independent (as they are based on essentially the same data-sets) we multiply the error on the average by $\sqrt{3}$, 3 being the number of values used to compute the average. In fact, the usual error on the weighted average decreases like the square root of the number of values.

The mean value and its error are shown as solid and dashed lines in the left panels of Fig. 5.7. In the right panels of Fig. 5.7, we plot the values of scale and virial radius obtained from the three independent methods: kinematics, X-ray and WL. The average error-weighted value and its error, this time computed

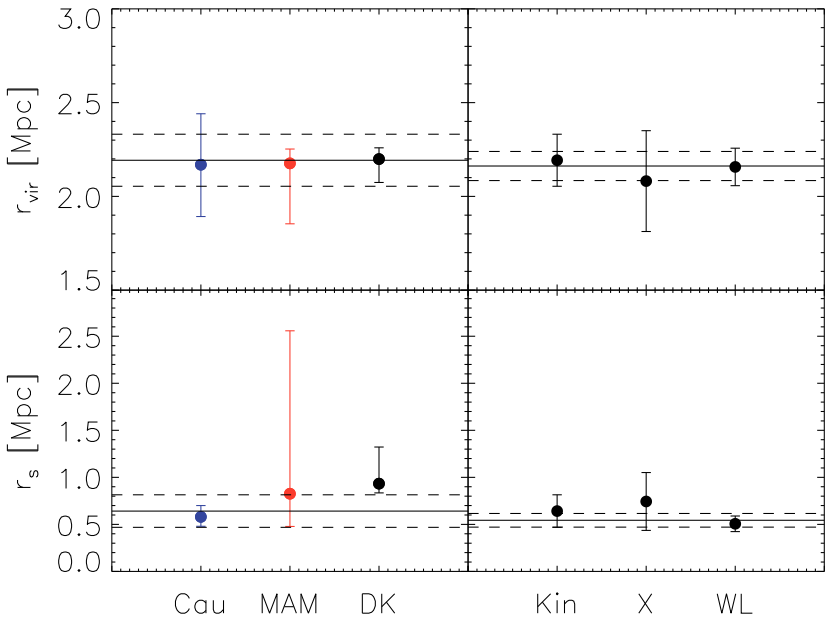

Figure 5.7: Virial (top panels) and scale (bottom panels) radius for all the methods. *Left panels:* blue diamonds are values obtained from the caustic technique, red ones for MAMPOSSt, and black ones for DK (from left to right, respectively). The average value and its error are the solid and dashed lines, respectively. See the text for the computation of the error. *Right panels:* values obtained from the kinematical analysis, X-ray and WL (from left to right, respectively). The average value and its error are the solid and dashed lines, respectively.

without multiplication factor (since the three measures are independent), are $r_{200} = 2.16 \pm 0.08$, $r_s = 0.54 \pm 0.07$.

5.5 Velocity anisotropy profiles

The Jeans equation can be solved for $\beta(r)$ to obtain information about the anisotropy of the orbits of the system. The Jeans equation contains 4 unknown quantities, therefore to solve it we need other 3 relations, namely the Abell integrals to relate the projected number density and velocity dispersion to the real ones and assume a mass profile for the cluster. This *anisotropy inversion* was first solved by Binney and

Mamon (1982), but several other authors have provided simpler algorithms. We follow the approach of Solanes and Salvador-Sole (1990), and we test the results by comparing them with those obtained following the approach of Dejonghe and Merritt (1992). Once the mass profile is specified, this procedure is fully non parametric. In fact, instead of fitting the number density profile, we bin and smooth it with the LOWESS technique (see, e.g. Gebhardt et al., 1994). We then obtain the 3D number density profile by using Abel's equation (e.g., Binney and Mamon, 1982). In the same way, we smooth the binned $\sigma_{\rm los}$ profile. This procedure requires the solution of integrals up to infinity. Mamon et al. (2010) showed that a $3\,\sigma$ clipping removes all the interlopers beyond 19 virial radii. Therefore, an extrapolation up to such a distance is enough to solve the integrals having infinity as limit of integration. We use 30 Mpc as the maximum radius of integration, and extrapolate the smoothed profiles up to this limit. A factor 2 change of the upper limit of integration does not affect our results in a significant way.

The result of the anisotropy inversion is shown in Fig. 5.8. The confidence levels are obtained by estimating two error contributions. One contribution comes from the uncertainties in the number density and $\sigma_{\rm los}$ profiles. Since the number density profile is affected by much smaller uncertainties than the $\sigma_{\rm los}$ profile, we only consider the error contribution from the latter. It is virtually impossible to propagate the errors on the observed $\sigma_{\rm los}$ through the Jeans inversion equations to infer the uncertainties on the β profile solution. We then proceed to estimate these uncertainties the other way round. We modify the β profile in two different ways: 1) $\beta(r) \to \beta(r) + S + T\,r$, and 2) $\beta(r) \to J\,\beta(r) + Y$, using a wide grid of values for the constants, respectively (S, T) and (J, Y). Using the mass and anisotropy profiles, it is then possible to determine $\sigma_r(r)$ and then the $\sigma_{\rm los}$ profile (e.g., Mamon and Łokas, 2005b). The range of acceptable β profiles is determined by a χ^2 comparison of the resulting $\sigma_{\rm los}$ profiles with the observed one.

In addition, another source of uncertainty on the β profile solution comes from the uncertainty in the mass profile. This is estimated by running the anisotropy inversion for four different mass profiles corresponding to the combination of allowed values of virial and scale radii within $1\,\sigma$. The profiles obtained modifying the mass profile (not shown) lie within the confidence interval of the main result, hence the confidence interval represents well the uncertainty on the anisotropy profile.

The ALL sample $\beta(r)$ depends weakly on radius: the innermost region is compatible with isotropy, while the anisotropy is increasingly radial at large radii. The RED sample is compatible with isotropy at almost all radii. The difference between the two samples is almost entirely due to the BLUE galaxies, the anisotropy

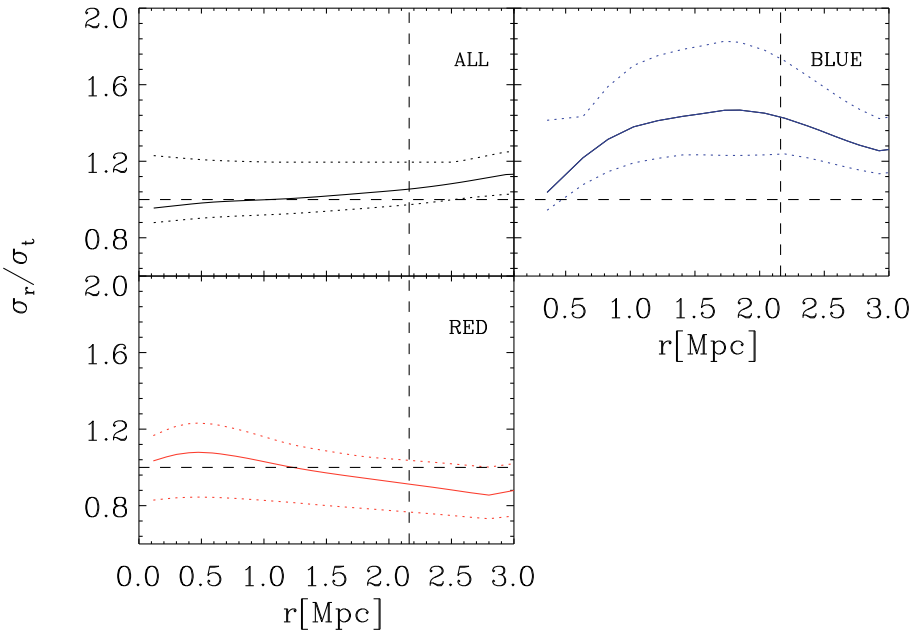

Figure 5.8: Velocity anisotropy profile for the ALL, RED and BLUE samples. The solid line is the result of the inversion of the Jeans equation, while the dotted lines are the 1σ confidence intervals. The vertical dashed line locates the virial radius.

of which is compatible with isotropy in the center, then becomes rapidly radially anisotropic and finally flattens at radii $>$ 1Mpc.

As a check, we compare the values of β obtained from the anisotropy inversion with the best-fit results of DK and MAMPOSSt. In these techniques, we assumed a constant value of the anisotropy for the RED sample, which appears to be a good assumption given the results of β after the inversion. The value estimated by both DK and MAMPOSSt is $\beta = 0.0$, consistent within the uncertainties with the β profile shown in Fig. 5.8.

5.6 $Q(r)$ and $\beta - \gamma$ relations

We can take advantage of the results just found for the galaxy populations of A2142 to test the PPSD profile and the relation linking the logarithmic slope of the density profile and the anisotropy $\beta(r)$.

The mass is dominated by dark matter, which is not an observable, so we use the galaxies as tracers of the total matter dynamics. We thus consider the radial velocity dispersion and velocity anisotropy that we measured (using our concordance mass profile) for the galaxies (see Sect. 5.5), instead of those of the dominant DM, which we cannot directly measure. We still have a choice for the density profile in both the PPSD and the $\beta - \gamma$ relation: it could be either the total density profile or the density profile of the tracer for which we compute the radial velocity dispersion and the anisotropy.

5.6.1 Use of the total matter density profile

We begin by adopting the total density profile $\rho(r)$. We compute both the PPSD profile $Q(r) = \rho/\sigma^3$ and its radial counterpart $Q_r(r) = \rho/\sigma_r^3$. In the top panels of Fig. 5.9, we show, for the different tracers (ALL, RED, BLUE), the radial profile of $Q(r)$ (left panels) and $Q_r(r)$ (right panels) within the virial radius. In order to compute the errors on the best-fit slope parameters, we have assumed the number of independent Q and Q_r values to be the same as those of the observed velocity dispersion profile (see Fig. 5.4).

Assuming a power-law behaviour of the PPSD profile, as suggested by Dehnen and McLaughlin (2005), we fit the profiles of both $Q(r)$ and $Q_r(r)$ in two ways: either keeping the exponent fixed to the values found for haloes in ΛCDM simulations by Dehnen and McLaughlin (2005) or considering it as a free parameter. In Table 5.4 the results of such fits are shown. The $Q(r)$ profile for the RED sample is in good agreement with the $r^{-1.84}$ relation by Dehnen and McLaughlin (2005), the latter being almost always within the confidence interval of our results. The fit of the profile with a linear relation in the log-log plane is compatible with the theoretical value -1.84 within $1.7\,\sigma$. On the other hand, for the BLUE sample, the slope of the PPSD is steeper than the theoretical expectation.

The $Q_r(r)$ profiles of all 3 samples are in good agreement with the relation that Dehnen and McLaughlin (2005) found for simulated ΛCDM haloes, $r^{-1.92}$. The better agreement for the BLUE sample is due to the relatively larger uncertainty that we have on σ_r with respect to σ, because of the large uncertainties that affect $\beta(r)$. The profile for the RED sample is in agreement with the theoretical relation within $0.3\,\sigma$.

Ludlow et al. (2010) warn against fitting the pseudo phase space density profile outside the scale radius, because of the upturn they find in the $Q(r)$ profile in the

	$Q(r)$		$Q_r(r)$	
	A $[M_\odot\ Mpc^{-3}\ km^{-3}\ s^3]$	B	A $[M_\odot\ Mpc^{-3}\ km^{-3}\ s^3]$	B
Fixed slope				
ALL	5534 ± 314	-1.84	25071 ± 3341	-1.92
RED	7727 ± 391	-1.84	38484 ± 5622	-1.92
BLUE	1753 ± 294	-1.84	3998 ± 1084	-1.92
Free slope				
ALL	6342 ± 367	-2.28 ± 0.11	29175 ± 4223	-2.27 ± 0.24
RED	8034 ± 411	-2.00 ± 0.09	38881 ± 5665	-1.77 ± 0.23
BLUE	3121 ± 793	-2.97 ± 0.50	5413 ± 1810	-2.60 ± 0.67

	$Q(r)\ GAL$		$Q_r(r)\ GAL$	
	A $[10^{-9}\ Mpc^{-3}\ km^{-3}\ s^3]$	B	A $[10^{-9} Mpc^{-3}\ km^{-3}\ s^3]$	B
Fixed slope				
ALL	6.82 ± 0.68	-1.84	28.49 ± 5.37	-1.92
RED	3.62 ± 0.46	-1.84	13.23 ± 3.21	-1.92
BLUE	0.98 ± 0.23	-1.84	1.30 ± 0.47	-1.92
Free slope				
ALL	10.19 ± 25.60	-1.09 ± 0.15	46.94 ± 7.34	-1.09 ± 0.26
RED	8.21 ± 17.01	-0.90 ± 0.14	40.48 ± 6.69	-0.71 ± 0.25
BLUE	0.88 ± 1.81	-0.90 ± 0.61	1.52 ± 0.55	-0.52 ± 0.74

Table 5.4: The PPSD profile is parametrized as $Q(r) = A \cdot r^B$. The first panel at the top shows the results of the fit of $Q(r)$ and $Q_r(r)$ for the different samples, both when keeping fixed the exponent to the values suggested by Dehnen and McLaughlin (2005), and when considering the exponent as a free parameter. In the bottom panel, the one identified by $Q(r)\ GAL$ and $Q_r(r)\ GAL$, the same quantities are shown, but referred to the PPSD computed using the galaxy number density profile instead of the total matter density profile.

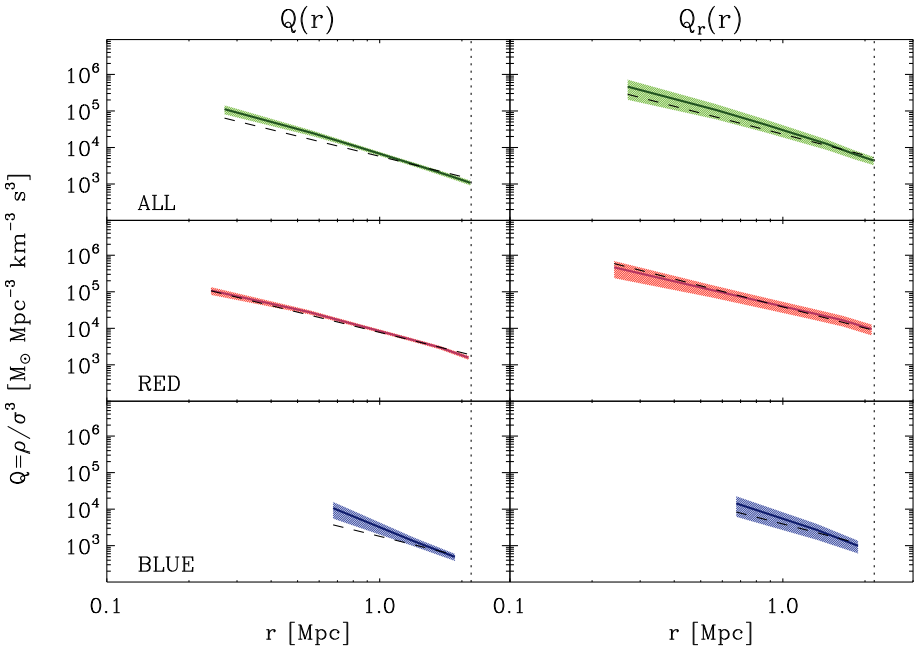

Figure 5.9: Radial profiles of Q (left columns) and Q_r (right columns) within the virial radius, and the $1\,\sigma$ confidence regions (shaded areas), for different types of member tracers: green for the ALL sample (top panels), red for the RED sample (middle panels) and blue for the BLUE sample. The shaded areas represent the propagation of the errors associated with ρ, σ and σ_r. The dashed lines are the power-law relations $Q(r) \propto r^{-1.84}$ and $Q_r(r) \propto r^{-1.92}$ found by Dehnen and McLaughlin (2005) on numerically simulated haloes. The vertical dotted lines locate the virial radius of the concordance model (see Sect. 5.4).

outer regions. However, for our 3 samples, none of the $Q(r)$ and $Q_r(r)$ profiles show significant curvature in log-log space.

In Fig. 5.10, we show the $\beta(r) - \gamma(r)$ relation. The $\beta - \gamma$ relation of the ALL sample matches well that found by Hansen and Moore (2006) on single-component dissipationless simulations (cosmological and academic). However, the $\beta - \gamma$ relation for the RED sample shows curvature, with lower values of β at the steeper slopes (larger radii) than found in simulations by Hansen and Moore (2006).

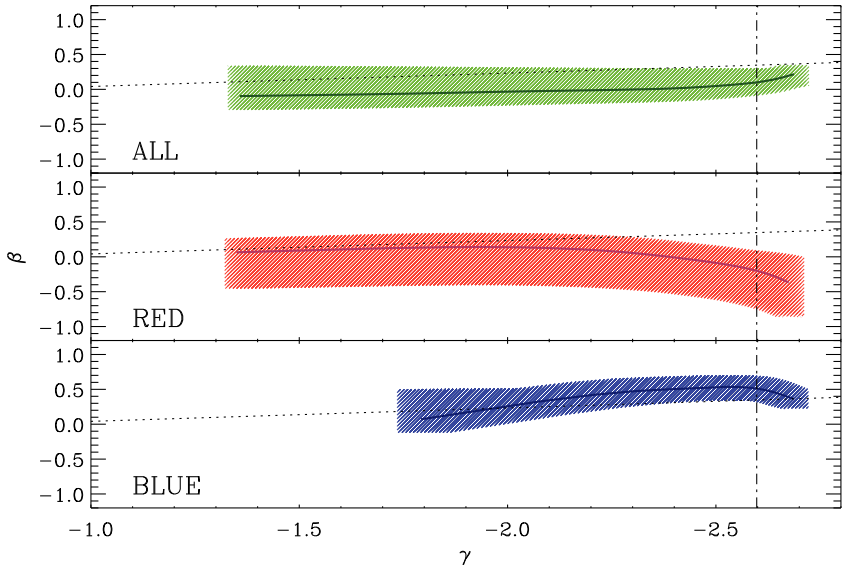

Figure 5.10: Velocity anisotropy versus logarithmic slope of the total density profile. The samples are ALL galaxies (top), RED (middle) and BLUE galaxies (bottom panel). The dashed areas are the $1\,\sigma$ confidence regions. The $\beta - \gamma$ relation found by Hansen and Moore (2006) for single-component dissipationless simulations is shown as the dotted lines. The vertical dot-dashed line locates the value of γ relative to the virial radius.

5.6.2 Use of the tracer density profile

We now repeat our analyses of the PPSD and the $\beta - \gamma$ relations, replacing the total mass density with the number density of the tracer of the sample.

In Fig 5.11, we show the PPSD computed using the galaxy number density profile instead of the total matter density one. For all three samples, both $Q(r)$ and $Q_r(r)$ remain as power laws, but are considerably shallower than the relation found by Dehnen and McLaughlin (2005) on simulated ΛCDM halos.

In Fig. 5.12, we show the $\beta - \gamma$ relation computed using the galaxy number density profile instead of the total matter density one. The behaviour does not change significantly from the case of the $\beta - \gamma$ relation computed using the total matter density profile: the global shapes of the profiles are similar but the BLUE sample now presents a noisier profile, while ALL and RED profiles are shifted

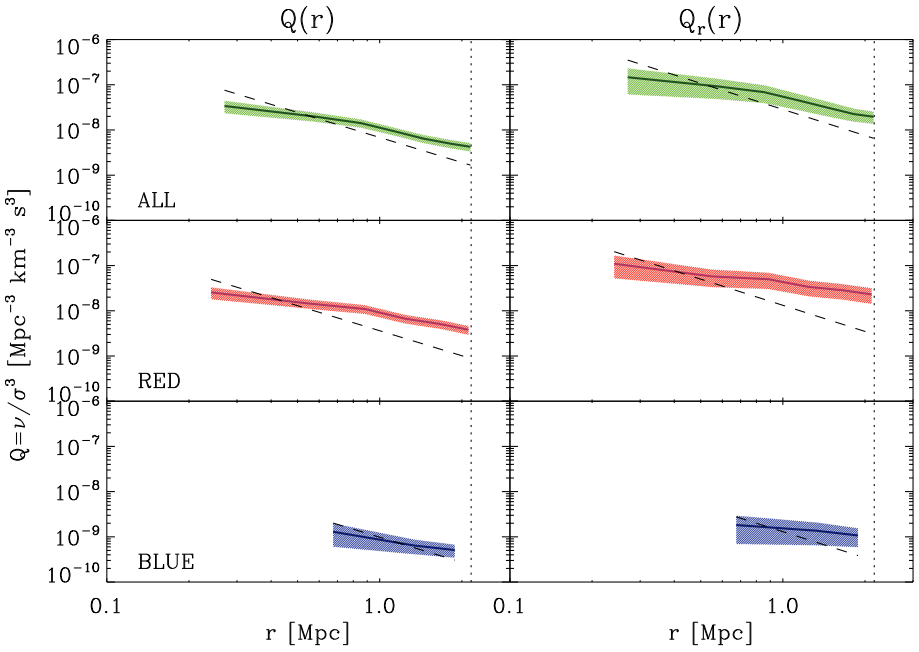

Figure 5.11: Same as Fig. 5.9, but now using the radial profiles of galaxy number density instead of total mass density to estimate the PPSD.

toward higher values of γ, reflecting the shallower trend of the galaxy number density profile with respect to the matter density one.

5.7 Conclusions and Discussion

We have computed the mass and velocity anisotropy profiles of A2142, a nearby ($z = 0.09$) cluster, using the kinematics of cluster galaxies. After a membership algorithm was applied, we considered the sample made of all members (ALL sample), as well as two subsamples, consisting in blue member galaxies (BLUE sample) and in red member galaxies that do not belong to substructures (RED sample).

We have made use of three methods based on the kinematics of galaxies in spherical clusters: DK, MAMPOSSt and Caustic (see Sect. 5.3). The mass profiles, as well as the virial values of the mass and the radius, are consistent among the different methods, and in agreement with the results coming from the X-ray (Akamatsu et al., 2011) and the weak lensing (Umetsu et al., 2009) analyses. Serra et al.

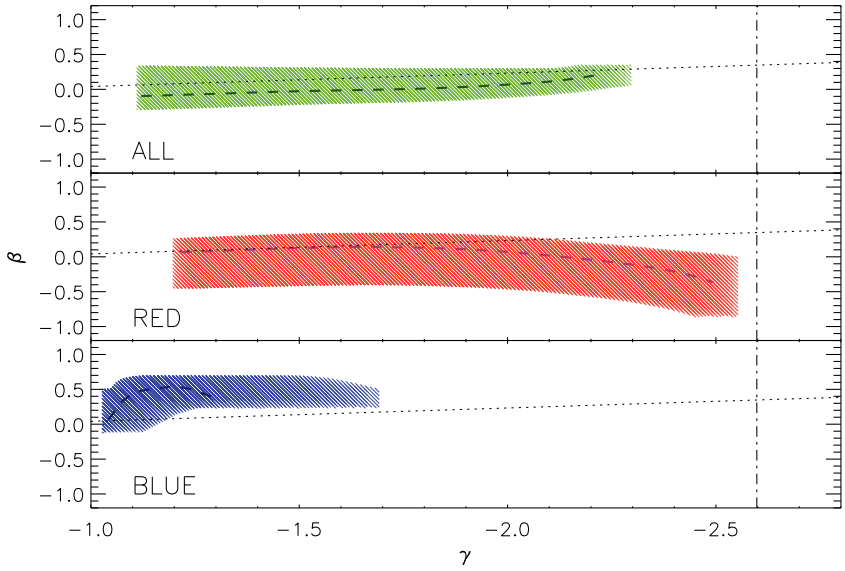

Figure 5.12: Same as Fig. 5.10, but now using the radial profiles of galaxy number density of the three samples instead of total mass density to estimate the slope.

(2011) found that the caustic technique tends to overestimate the value of mass in the central region of a cluster. Our results appear consistent with this finding, the caustic mass profile increasing more rapidly with radius in the inner part with respect to the profiles coming from DK and MAMPOSSt.

Munari et al. (2013a) report the scaling relation between the virial mass of clusters and the velocity dispersion of the member galaxies within the virial sphere. Using the most realistic ("AGN") hydrodynamical simulation at their disposal, they find $\sigma_{1D} = 1177\,[h(z)\,M_{200}/10^{15}M_{\odot}]^{0.364}$ for the galaxies within the virial sphere, where σ_{1D} is the total $3D$ velocity dispersion within r_{200}, divided by $\sqrt{3}$. The analysis was carried out in the 6D phase space, hence is immune to projection effects. Nevertheless, because of the statistical nature of the relation they find, it provides a relation which is likely to hold for real, observed systems in a relaxed state. As a test, we check the consistency of the velocity dispersion – mass relation found by Munari et al. (2013a) with our findings for A2142. The values of virial mass obtained with this relation are as follows: $1.42 \times 10^{15}M_{\odot}$ for the ALL sample, $1.07 \times 10^{15}M_{\odot}$ for the RED sample and $2.50 \times 10^{15}M_{\odot}$ for the BLUE sample. The

values obtained for the ALL and RED samples are in agreement, within the uncertainties, with the concordance value of the mass of A2142. This seems to indicate that RED cluster members are in, or very close to, equilibrium. The large difference obtained for the BLUE cluster members warns against using the blue galaxy los velocity dispersion as a proxy for the cluster mass.

A glance at Table 5.3 indicates that our different estimates of the mass concentrations are bimodal: the caustic and weak lensing have values $\simeq 4$, while those for the DK, MAMPOSSt and X-ray methods are < 3.

Could these lower mass concentrations found by methods based upon internal kinematics be a sign that A2142 is out of dynamical equilibrium? The substructures found by Owers et al. (2011) and the results by Rossetti et al. (2013) on the importance of the mergers undergone by A2142 suggest that full relaxation is to be excluded. On the other hand, the agreement on the virial radius among the different method and with the results from X-ray and lensing (the latter of which does not require equilibrium) suggests that A2142 is not far from dynamical equilibrium. This allows us to assume a concordance model for the mass profile, with $M_{200} = (1.25 \pm 0.13) \times 10^{15} \mathrm{M}_{\odot}$ and $c = 4.0 \pm 0.5$.

Previous studies based on the kinematics of galaxies in clusters have shown that galaxy populations have similar concentrations to those of the total matter, or slightly smaller, blue galaxies being instead much less concentrated (see, e.g., Biviano and Girardi, 2003; Katgert et al., 2004). On the other hand, Biviano and Poggianti (2009) found in the ENACS clusters that the red galaxy population has a concentration that is as much as 1.7 times lower than that of the total matter density profile. Here, we find that the scale radius for the RED galaxy number density profile (0.95 kpc) is 1.8 times greater than that of the total mass density profile from our concordance model, which is in agreement with the ENACS result.

The scale radius of the BLUE population in Abell 2142 appears unusually high, leading to a concentration (using our concordance virial radius) of 0.16 (best) or 0.39 ($+1\,\sigma$), which are much lower than expected from previous studies. Blue galaxies within the virial cones of clusters are more prone to projection effects than red galaxies: Mahajan et al. (2011) analysed clusters and their member galaxies in the SDSS, using los velocities and cosmological simulations to quantify the projection effects. They conclude that $44 \pm 2\%$ of galaxies with recent (or ongoing) starbursts that are within the virial cone are outside the virial sphere. Since galaxies with recent star formation have blue colours, our BLUE sample includes this recent-starburst subsample, plus perhaps some more galaxies with more moderate recent star formation. Moreover, an analysis of cosmological simulations by Mamon et al. (2010) indicates that there is a high cosmic variance in the fraction of interlopers

within the DM particles inside the virial cone. This suggests that the unusually low concentration of the blue galaxy sample could be a sign of an unusually high level of velocity interlopers with low rest frame velocities in front and behind Abell 2142.

Wojtak and Łokas (2010) found a virial radius that corresponds to $r_{200} = 2.15^{+0.10}_{-0.12}$ Mpc, in excellent agreement with our different estimates of the virial radius (Table 5.3). On the other hand, they find a scale radius $r_s = 1.0^{+0.3}_{-0.2}$Mpc not compatible with our value of the concordance model, although in agreement with the results of the DK, MAMPOSSt and X-ray analyses. Note that Wojtak and Łokas assumed that the DM and galaxy scale radii were equal. Such an unverified assumption may have biased high their scale radius for the mass distribution. On the other hand, the values of the DM scale radii that we found from DK and MAMPOSSt (0.93 and 0.83 Mpc, respectively, see Table 5.3) are quite close to that of the RED galaxy population used as the tracer (0.95 Mpc).

The parameters describing the mass profile are then used to invert the Jeans equation and compute the velocity anisotropy for the three different samples considered. Despite large uncertainties, the $\beta(r)$ profile for the full set of cluster members is compatible with isotropy, becoming weakly radially anisotropic in the outer regions. The behaviour of the RED sample is different. Although compatible within 1σ with isotropy at all radii within r_{200}, it has a marginally significant decreasing slope, starting slightly radially anisotropic in the center and becoming slightly tangentially anisotropic at large radii. The difference between the $\beta(r)$ profiles for the ALL sample and the RED sample is mainly due to the behaviour of the BLUE sample, which shows radial anisotropy at all radii except in the center where it is isotropic.

The velocity anisotropy profile for the ALL sample in the center is compatible with that found by Wojtak and Łokas (2010). In the outer part, at $\simeq$ 3Mpc, the value of σ_r/σ_θ found by Wojtak and Łokas (2010) is higher and 1.4σ distant from ours. Analysing a stacked sample of 107 ENACS clusters, Biviano and Katgert (2004) found the orbits of ellipticals and S0s (hence red) galaxies to be compatible with isotropy and those of early and late-type spirals to have radial anisotropy. The velocity anisotropy profile for our BLUE sample presents a behaviour that lies in between the profiles found in Biviano and Katgert for the early spirals and the late spirals together with emission line galaxies, suggesting agreement between their findings and ours. The anisotropy profiles we found for the ALL sample appears to be consistent with that measured in simulated ΛCDM haloes by Lemze et al. (2012). The scatter in the anisotropy profiles is considerable in the above-mentioned papers and this reflects the variety of configurations of galaxy clusters.

In this sense, the behaviour of the anisotropy of A2142 does not present strong deviations from the general trend.

With the information obtained on A2142, we are able to test some theoretical relations regarding the interplay between the mass distribution and the internal kinematics of a cluster. We investigated the radial profile of the pseudo phase space density $Q(r)$, as well as its radial counterpart $Q_r(r)$. When we consider the total density profile to compute Q and Q_r, we find that the profiles for A2142 are weakly consistent with the theoretical expectations (Dehnen and McLaughlin, 2005; Ludlow et al., 2010) when considering the ALL sample, but a good agreement is observed in the RED sample. This strengthens the scenario of blue galaxies being a population of galaxies recently fallen into clusters, that have had no time to reach an equilibrium configuration yet, or are heavily contaminated by interlopers.

Biviano et al. (2013) have performed a similar analysis on MACS1206, a cluster at $z = 0.44$. They find a $Q(r)$ profile with a slope for the blue galaxies in agreement with the predictions of Dehnen and McLaughlin (2005). We speculate that this different behaviour might provide a hint on the dynamical history of clusters. In fact, a cluster that has undergone the phase of violent relaxation only recently might present a population of blue galaxies in equilibrium. On the other hand, a cluster that has undergone the violent relaxation phase since long, should have had time to transform its blue galaxies into red ones. Therefore the blue galaxy population would be mainly composed of only recently accreted galaxies, hence not in dynamical equilibrium.

We estimate the PPSD profile of the total matter making the assumption that the galaxy velocity dispersion is a good proxy for the total matter dynamics. When we replace the total mass density by the number density of the tracer for which we compute the velocity dispersion, the PPSDs are shallower power-laws than those found by Dehnen and McLaughlin (2005) in simulated ΛCDM haloes.

The anisotropy configuration of the internal kinematics reflects the formation history of the cluster. Therefore we expect a relation between the anisotropy and the potential of the cluster. A relation linking the $\beta(r)$ profile and $\gamma(r)$, the logarithmic slope of the potential, has been analysed and compared to the theoretical results provided by Hansen and Moore (2006), resulting in a weak agreement. A correlation between the β and γ appears to hold out to $\gamma \simeq -2.3$ in the RED sample, corresponding to a radial distance $\simeq 0.5\, r_{200} \simeq 1\,\mathrm{Mpc}$. Interestingly, cluster-mass simulated ΛCDM haloes also follow the Hansen and Moore relation out to slopes of $\gamma \approx -2.3$ but not beyond (see Fig. 17 of Lemze et al., 2012). Our considerations do not change when we compute the $\beta - \gamma$ relation using the logarithmic slope of the number density profile of galaxies instead of the total matter density profile.

This brings the question of what is more relevant for galaxy clusters: the total mass density or the tracer number density? One can argue that the PPSDs found in ΛCDM haloes are the consequence of the global gravitational potential (hence total mass profile), violent relaxation, or more generally the mass assembly of clusters through a combination of a several major mergers and numerous minor mergers. Alternatively, one can argue that it is inconsistent to associate the total density profile to the tracer velocity dispersion profile and that one should instead associate the tracer density profile to the tracer velocity dispersion profile. Similar questions arise for the origin of the NFW model for density profiles on one hand and of the $\beta - \gamma$ relation on the other.

For giant elliptical galaxies, the NFW model must apply to the DM component, while the observed tracer applies for $\beta - \gamma$. Indeed, Mamon and Łokas (2005a) have shown that the observed inner aperture velocity dispersions are too high to be matched by a single NFW component (while the addition of a stellar Sérsic component matches the observations). Moreover, in the elliptical galaxy remnants of binary mergers of spiral galaxies made of stars, gas and DM, the $\beta - \gamma$ relation is well obeyed by the stellar component (Mamon et al., 2006), but not well with the slope of the total mass density profile (Mamon, unpublished).

So it surprising that the PPSDs that we measure for Abell 2142 match better the relations found in ΛCDM haloes when the total density profile is used instead of the density profile of the tracer used to estimate the velocity dispersion. Perhaps one should not expect clusters to behave as elliptical galaxies. Indeed, in comparison with the progenitors of elliptical galaxies, the progenitors of clusters (galaxy groups) have deeper gravitational potentials that more effectively prevent cooling and dissipative contraction of gas. Moreover, cluster-mass halos grow relatively faster at $z = 0$ than galaxy-mass halos (e.g., van den Bosch, 2002), hence are built by more recent mergers than elliptical galaxies, and these mergers, some major, will mix the inner regions. For this reason, the baryonic and DM mass distributions in clusters are closer than in elliptical galaxies.

At all radii, the RED galaxy sample shows somewhat lower β for given γ (measured with total mass density) than found in simulated haloes. This slight mismatch might be due to the use of galaxies as tracers of the internal kinematics of the cluster. In fact, it has been shown (see e.g. Ludlow et al., 2010; Munari et al., 2013a) that galaxies and DM may have different kinematics. Furthermore, the above-mentioned relations have been derived using DM-only simulations, therefore the effect of the presence of baryons is not taken into account. Finally, the $\beta - \gamma$ relation may vary from cluster to cluster (Ludlow et al., 2011).

Before reaching any conclusion, we must keep in mind that the present theo-

retical studies are lacking the influence of the baryonic physics, as well as the dynamical processes acting on galaxies but not on DM particles. This might induce the differences when comparing the theoretical predictions with the observational results.

When we will have a better control on these properties, the PPSD might provide a powerful tool for the study of structure formation. As an example, the PPSD of the blue galaxies in A2142 appears very different from that found for the blue galaxies in another cluster, MACS J1206.2–0847 at $z = 0.44$ (Biviano et al., 2013). This discrepancy suggests interesting perspectives for the comprehension of the formation of galaxy clusters.

6

The relation between velocity dispersion and mass in simulated clusters of galaxies

6.1 Introduction

The methods to measure the mass of galaxy clusters are described in Sect. 4.2. In the same section, it was pointed out that methods like the X-ray or WL can only be applied to clusters for which high quality data are available, like in the case of A2142 whose mass has been derived by means of the kinematics of its member galaxies in Sect. 5.4.2.

When these high quality data are not available, it is still possible to infer cluster mass using the mass proxies. In this thesis the velocity dispersion of member galaxies is considered. It is crucial to understand whether a cluster velocity dispersion measured on its member galaxies is a reliable proxy for its mass. Calibration of such scaling relation can be based on detailed multi-wavelength observations of control samples of galaxy clusters. On the other hand, detailed cosmological simulations are quite useful to calibrate such scaling relations independently from possible observational systematic effects (e.g. Borgani and Kravtsov, 2011, and references therein).

The implementation of baryonic physics can play a fundamental role in these analysis. In principle, since galaxies are nearly collisionless tracers of the gravitational potential, one expects velocity dispersion to be more robust than X-ray and SZ mass proxies against the effects induced by the presence of baryons and by their

thermal history.

Using a set of cluster-sized halos extracted from a ΛCDM cosmological simulation, Biviano et al. (2006) analysed the reliability of the velocity dispersion as a mass proxy. They considered both DM particles and simulated galaxies as tracers of the gravitational potential of their host halo. They found that in typical observational situations, the use of the line-of-sight velocity dispersion, $\sigma_{\rm los}$, allows a more precise cluster mass estimation than the use of the virial theorem. They used only one kind of simulation without exploring different baryonic physics.

Evrard et al. (2008) analysed the $\sigma_{200} - M_{200}$ relation using several cosmological simulations, and showed that it is close to the virial scaling relation $\sigma_{200} \propto M_{200}^{1/3}$ across a broad range of halo masses, redshifts, and cosmological models. When looking at simulated galaxies, some studies found that they show a significant, albeit small, velocity bias with respect to DM particles (Diemand et al., 2004; Faltenbacher et al., 2005; Faltenbacher and Diemand, 2006; Faltenbacher and Mathews, 2007; Lau et al., 2010). These studies agreed that the amplitude of the velocity bias, i.e. the ratio between the velocity dispersions of simulated galaxies and DM particles, is not larger than $\approx 10\%$, but disagreed on whether galaxies are positively (velocity bias > 1) or negatively (velocity bias < 1) biased. The disagreement is unlikely to come from resolution issues (Evrard et al., 2008). Other effects are more important in affecting the value of the bias, such as the distance from the cluster centre (Diemand et al., 2004; Gill et al., 2004), baryon dissipation and redshift dependence (Lau et al., 2010).

The way simulated galaxies are selected also has an important effect on the amount of velocity bias. By selecting simulated galaxies in stellar mass, rather than in total mass, the velocity bias is strongly reduced or even suppressed (Faltenbacher and Diemand, 2006; Lau et al., 2010). A similar effect is seen when the selection of simulated galaxies is based on their total mass at the moment of infall, which is found to be proportional to the stellar mass (Faltenbacher and Diemand, 2006; Lau et al., 2010; Wetzel and White, 2010). The proportionality between total and stellar mass of a galaxy is lost after the galaxy enters the cluster, because the DM halo is more easily stripped than the stellar component by the cluster tidal forces (Diemand et al., 2004; Boylan-Kolchin et al., 2008; Lau et al., 2010; Wetzel and White, 2010). Observational evidence for tidal stripping of cluster galaxies has been obtained from lensing studies (Natarajan et al., 2002; Limousin et al., 2007). Tidal stripping is more effective for galaxies moving at lower velocities (Diemand et al., 2004). When the mass removed from a simulated galaxy by tidal stripping is such that the galaxy mass drops below the resolution limit, the galaxy is effectively

tidally disrupted. As the galaxies that are disrupted are preferentially those of smaller velocities, the survivers will display on average a larger velocity dispersion than DM particles, i.e. a positive velocity bias (Faltenbacher and Diemand, 2006).

Another important process is dynamical friction (Chandrasekhar, 1943; Esquivel and Fuchs, 2007), which removes energy from a galaxy orbit, bringing it closer to the cluster centre, and slowing down its velocity (e.g. Boylan-Kolchin et al., 2008; Wetzel and White, 2010). If a sufficient number of galaxies is slowed down by dynamical friction and survive both tidal disruption and merging with the central galaxy, dynamical friction might cause a negative velocity bias in the cluster galaxy population.

All the processes discussed so far alter the dynamics of tracers like galaxies, providing a source of uncertainty in the aforementioned relation linking mass and velocity dispersion. With that comes the need of further investigations about this topic, also because of the different results found in the literature on the velocity bias of cluster galaxies. The aim of the study presented in this chapter is to characterise the relation between the velocity dispersion and the mass of simulated halos spanning a wide mass range, from $\sim 10^{13}\mathrm{M}_{\odot}$ to $\gtrsim 10^{15}\mathrm{M}_{\odot}$, at different redshifts (from $z = 2$ to $z = 0$), and using different tracers, DM particles, subhalos, and galaxies, in order to understand how reliable is the velocity dispersion as a proxy for cluster masses. Simulations with different physics implemented are used, in order to understand how different physical processes affect the structures and hence the dynamics of tracers.

In this chapter we do not consider observational biases, such as projection effects and presence of interlopers (Biviano et al., 2006; Saro et al., 2012), but we focus on the effects due to the physics and the implementation of baryonic physics in the simulations. We find that such implementation affects the kinematics of the systems. The analysis of observational effects must therefore be based on simulations where baryonic physics is taken into account.

This chapter is structured as follows. In Sect. 6.2 we describe the simulations used for this work and define the samples used in our analyses. In Sect. 6.3 we determine the relation between mass and velocity dispersion, and how it depends on redshift and on the different types of simulations. In Sect. 6.3.1 we quantify the scatter and its nature (statistical or intrinsic). In Sect. 6.3.2 we describe the velocity bias of subhalos and galaxies with respect to the underlying diffuse component of DM particles. In Sect. 6.3.3 we look for a signature of the different dynamical processes which are at work in galaxy systems, on the velocity distributions of the different tracers of the gravitational potential. Finally in Sect. 6.4 we discuss our results and present our conclusions.

6.2 Simulations

6.2.1 Initial conditions

Our samples of cluster-sized and group-sized halos are obtained from 29 Lagrangian regions, centred around as many massive halos identified within a large-volume, low-resolution N-body cosmological simulation, resimulated with higher resolution. We refer to Bonafede et al. (2011) for a more detailed description of the set of initial conditions used to generate samples of simulated clusters used for our analysis.

The parent Dark Matter (DM) simulation followed 1024^3 DM particles within a box having a comoving side of 1 h^{-1} Gpc, with h the Hubble constant in units of 100 km s^{-1} Mpc^{-1}. The cosmological model assumed is a flat ΛCDM one, with $\Omega_m = 0.24$ for the matter density parameter, $\Omega_{bar} = 0.04$ for the contribution of baryons, $H_0 = 72$ km s^{-1} Mpc^{-1} for the present-day Hubble constant, $n_s = 0.96$ for the primordial spectral index and $\sigma_8 = 0.8$ for the normalisation of the power spectrum. Within each Lagrangian region we increased the mass resolution and added the relevant high-frequency modes of the power spectrum, following the zoomed initial condition (ZIC) technique (Tormen et al., 1997). Outside these regions, particles of mass increasing with distance from the target halo are used, so that the computational effort is concentrated on the region of interest, while a correct description of the large scale tidal field is preserved. Each high-resolution Lagrangian region is shaped in such a way that no low-resolution particle contaminates the central zoomed-in halo at z = 0 at least out to 5 virial radii. As a result, each region is sufficiently large to contain more than one interesting halo with no contaminants within its virial radius.

Initial conditions have been first generated both for DM-only simulations. The mass of DM particles in the zoomed–in regions is $m_{DM} = 10^9\, h^{-1} M_\odot$. Henceforth we refer to these simulation as DM-only. Initial conditions for hydrodynamical simulations have been generated only in the low–resolution version, by splitting each particle within the high-resolution region into two, one representing DM and another representing the gas component, with a mass ratio such to reproduce the cosmic baryon fraction. The mass of each DM particle is then $m_{DM} = 8.47 \cdot 10^8\, h^{-1} M_\odot$ and the initial mass of each gas particle is $m_{gas} = 1.53 \cdot 10^8\, h^{-1} M_\odot$.

6.2.2 The simulation models

All the simulations have been carried out with the TreeePM–SPH GADGET-3 code, a more efficient version of the previous GADGET-2 code (Springel, 2005). As for the computation of the gravitational force, the Plummer-equivalent softening length is fixed to $\epsilon = 5\,h^{-1}$ kpc in physical units below z = 2, while being kept fixed in comoving units at higher redshift.

Besides the DM–only simulation, we also carried out a set of non–radiative hydrodynamic simulations (NR hereafter) and two sets of radiative simulations, based on different models for the release of energy feedback.

A first set of radiative simulations includes star formation and the effect of feedback triggered by supernova (SN) explosions (CSF set hereafter). Radiative cooling rates are computed by following the same procedure presented by Wiersma et al. (2009). We account for the presence of the cosmic microwave background (CMB) and for the model of UV/X–ray background radiation from quasars and galaxies, as computed by Haardt and Madau (2001). The contributions to cooling from each one of eleven elements (H, He, C, N, O, Ne, Mg, Si, S, Ca, Fe) have been pre–computed using the publicly available CLOUDY photo–ionisation code (Ferland et al., 1998) for an optically thin gas in (photo–ionisation) equilibrium. Gas particles above a given threshold density are treated as multiphase, so as to provide a sub-resolution description of the interstellar medium, according to the model originally described by Springel and Hernquist (2003). We also include a description of metal production from chemical enrichment contributed by SN-II, SN-Ia and low and intermediate mass stars (Tornatore et al., 2007). Stars of different mass, distributed according to a Chabrier IMF (Chabrier, 2003), release metals over the time-scale determined by the corresponding mass-dependent life-times (taken from Padovani and Matteucci 1993). Kinetic feedback contributed by SN-II is implemented according to the scheme introduced by Springel and Hernquist (2003): a multi-phase star particle is assigned a probability to be uploaded in galactic outflows, which is proportional to its star formation rate. In the CSF simulation set we assume $v_w = 500\,km\,s^{-1}$ for the wind velocity.

Another set of radiative simulations is carried out by including the same physical processes as in the CSF case, with a lower wind velocity of $v_w = 350\,km\,s^{-1}$, but also including the effect of AGN feedback (AGN set, hereafter). In the model for AGN feedback, released energy results from gas accretion onto supermassive black holes (BH). This model introduces some modifications with respect to that originally presented by Springel (2005) (SMH) and will be described in detail by Dolag et al. (2012, in preparation). BHs are described as sink particles, which grow

their mass by gas accretion and merging with other BHs. Gas accretion proceeds at a Bondi rate, while being Eddington–limited. Radiated energy corresponds to a fraction of the rest-mass energy of the accreted gas. This fraction is determined by the radiation efficiency parameter $\epsilon_r = 0.1$. The BH mass is correspondingly decreased by this amount. A fraction of this radiated energy is thermally coupled to the surrounding gas. We use $\epsilon_f = 0.1$ for this feedback efficiency, which increases to $\epsilon_f = 0.4$ whenever accretion enters in the quiescent "radio" mode and takes place at a rate smaller than one-hundredth of the Eddington limit (e.g. Sijacki et al., 2007; Fabjan et al., 2010).

6.2.3 The samples of simulated clusters

The identification of clusters proceeds by using a catalogue of FoF groups as a starting point. The SUBFIND algorithm (Springel et al., 2001; Dolag et al., 2009) is used to identify the main halo, whose centre corresponds to the position of the most bound DM particle, and substructures within each FoF group. In the following, we will name "galaxies" the bound stellar structures hosted by the subhalos identified by SUBFIND in the radiative CSF and AGN hydrodynamical simulations.

In this work we consider all the main halos with $M_{200} > 10^{13}\mathrm{M}_{\odot}$ from $z = 0$ to $z = 2$, which contain no low–resolution particles within the spherically defined r_{200}. Among these cluster-sized and group-sized halos, we only retain those with at least five subhalos more massive than $10^{11}\mathrm{M}_{\odot}$ within r_{200}. The number of selected halos varies at different redshifts and in different simulation sets, from a minimum of 54 to a maximum of 308.

The subhalos that we consider in our analysis are selected to be more massive than $10^{11}\mathrm{M}_{\odot}$, which corresponds to 72 particles in the DM simulations. The galaxies we consider in our analysis (in the CSF and AGN sets) are selected to have a stellar mass $\geq 3 \times 10^{9}\mathrm{M}_{\odot}$. By choosing this lower limit in stellar mass, we retain all subhalos more massive than $10^{11}\mathrm{M}_{\odot}$ and include many others with smaller masses. As a consequence, there are more halos with ≥ 5 galaxies than with ≥ 5 subhalos (within r_{200}). Note that the effects of the AGN feedback is negligible for galaxies with stellar masses below the chosen limit since they are generally hosted within halos where BH particles have never been seeded.

6.3 The velocity dispersion - mass relation

Given a tracer of the gravitational potential of a halo (DM particles, subhalos, galaxies) it is possible to write a relation between halo mass and velocity dispersion of the tracer, based on (i) the definition of circular velocity at r_{200}, $v_{200} = 10\,[G\,h(z)\,M_{200}]^{1/3}$, and (ii) the relation between σ_{200} and v_{200}. A relation between velocity dispersion and mass can be derived analytically once the form of the mass density profile and of the velocity anisotropy profile are given (see e.g. Mauduit and Mamon, 2007, and the erratum Mauduit and Mamon 2009).

Following Evrard et al. (2008), we use the one-dimensional velocity dispersion $\sigma_{1D} \equiv \sigma_{200}/\sqrt{3}$. Using the relations provided by Łokas and Mamon (2001, eqs. 22–26) we calculate the ratio between σ_{1D} and v_{200} for NFW mass profiles of concentrations $c = 3$ and 10, and for (constant) velocity anisotropies (see eq. 3.16) $\beta = 0$ and 0.5. These values of c and β are typical of group- and cluster-sized halos (e.g. Gao et al., 2008; Wojtak et al., 2008; Mamon et al., 2010). We find $\sigma_{1D}/v_{200} = 0.64, 0.69$ for $\beta = 0$ and $\sigma_{1D}/v_{200} = 0.68, 0.70$ for $\beta = 0.5$; the larger values are for $c = 10$. The average value we calculate using DM particles for all the halos selected in our analysis, $\sigma_{1D}/v_{200} = 0.68$, lies within the same range.

Using the range $\sigma_{1D}/v_{200} = 0.64$–$0.70$ just found, and the definition of v_{200}, we find

$$\frac{\sigma_{1D}}{\mathrm{km\ s^{-1}}} = A_{1D} \cdot \left[\frac{h(z)\,M_{200}}{10^{15} M_\odot}\right]^{\alpha} \tag{6.1}$$

with $A_{1D} = 1040$–1140 and $\alpha = 1/3$. Given that the real, simulated halos are not perfect NFW spheres, and that a halo concentration depends on its mass and redshift (e.g. Duffy et al., 2008; Gao et al., 2008), the real values of A_{1D} and α can be different, and need to be evaluated from the data. Moreover, DM particles, subhalos, and galaxies do not necessarily obey the same σ_{1D}–M_{200} relation. We therefore evaluate for each cluster of the samples described in Sect. 6.2.3 the values of σ_{1D} of DM particles, subhalos, and (for the CSF and AGN simulations) galaxies. The use of simulations with different baryonic physics implemented allows us to understand how baryons and different feedback models modify the scaling relation between velocity dispersion and mass. The σ_{1D} values of DM particles are obtained using the biweight estimator (Beers et al., 1990), when at least 15 data points are available. Otherwise, as suggested by Beers et al. (1990), we use the classical standard deviation. The confidence intervals for the σ_{1D} values are obtained using eq. (16) in Beers et al. (1990).

We then perform a linear fit to the $\log(\sigma_{1D})$ vs. $\log[h(z)\,M_{200}]$ values, with

σ_{1D} in units of km s^{-1} and M_{200} in units of $10^{15}\,h^{-1}M_\odot$, for each simulation set, at several redshifts. The fits were performed with the IDL procedure `linfit`, inversely weighting the data by the uncertainties in the values of σ_{1D}. The results of these fits are the values of the parameters A_{1D} and α of eq. (6.1). In Fig. 6.1 and 6.2 we show examples of these fits for the AGN simulations at redshift 0 and 1.26, respectively.

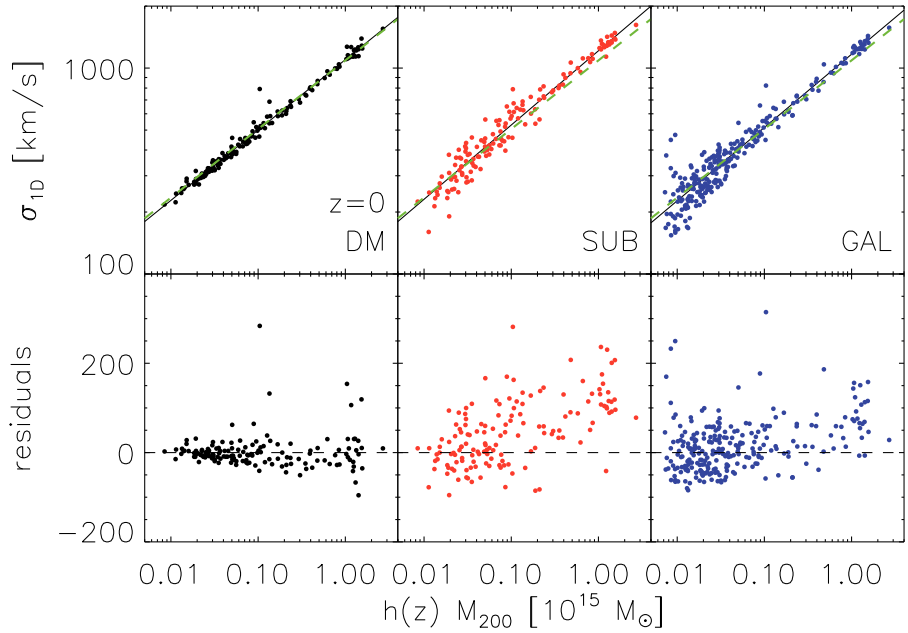

Figure 6.1: *Top panels:* velocity dispersion σ_{1D} (km s^{-1}) as a function of halo mass $h(z)\,M_{200}$ ($10^{15}\,M_\odot$), for DM particles (left panels), subhalos (central panels), and galaxies (right panels), at z=0, in the AGN simulation sets. The dashed green line represents the theoretically expected relation $\sigma_{1D} = 1090 \cdot (h(z)\,M_{200})^{1/3}$; the solid line in each panel represents the best-fit relation. *Bottom panels:* y-axis residuals of the DM particles (left), subhalos (centre), and galaxies (right), from the DM best-fit relation.

In Fig. 6.3 we show the best fitting values of A_{1D} and α as a function of redshift, for different tracers in the AGN simulation, as an example. The slope α is confirmed to be consistent with the theoretically expected value $\alpha = 1/3$. On the other hand, its value is significantly larger when using subhalos or galaxies as tracers. In any case the values of α and A_{1D} do not generally show a significant dependence

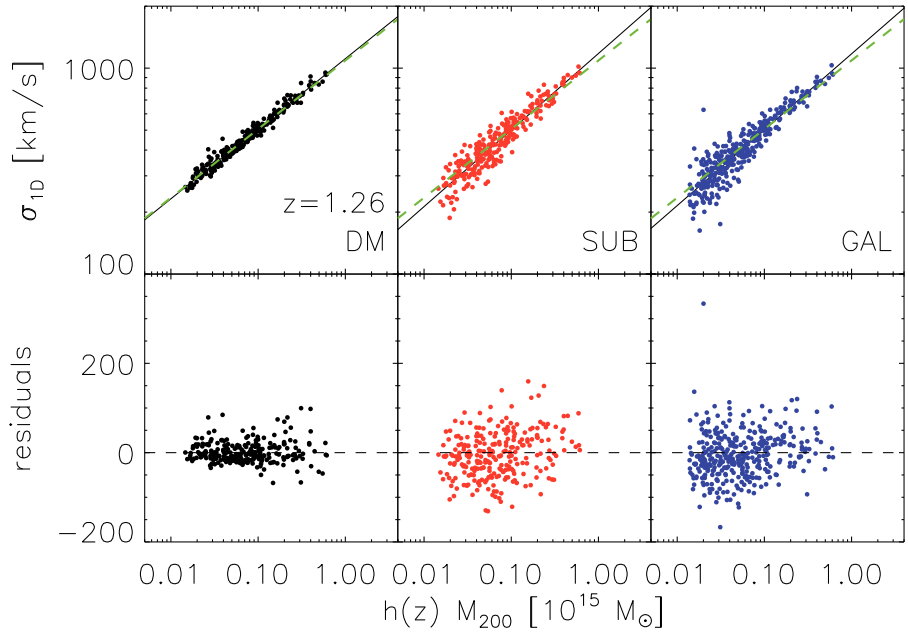

Figure 6.2: Same as Fig. 6.1 but for z=1.26.

on z. Only in two cases (subhalos in the DM simulation and galaxies in the AGN simulation - see Appendix 6.5) we do find (marginally) significant correlations between α and z, mostly driven by the point at z = 2. Even in these cases, α changes very little with redshift, $\simeq 4\%$ for the galaxies in the AGN simulation from z = 1.5 to z = 0. In fact, a model where α is constant with z provides an acceptable fit (in a χ^2 sense) to all cases (also those not shown in Fig. 6.3). Since the variation of A_{1D} and α with z is not significant, we take the weighted averages of their values over all redshifts to characterise the $\sigma_{1D} - M_{200}$ relations of the different types of simulations and tracers (see Table 6.1 and Fig. 6.4).

In Fig. 6.4 we show the dependence of the parameters α and A_{1D} on the physical processes included in the simulations. When considering DM particles as tracers, the A_{1D} values are well within the theoretically expected range, and the α values are close to the virial expectation 1/3, regardless of the baryonic physics implemented in the simulations. When considering subhalos or galaxies as tracers, the σ_{1D}-M_{200} relations are significantly steeper ($\alpha > 1/3$) than for DM particles and than expected theoretically. Furthermore, while the slope is nearly the same for all

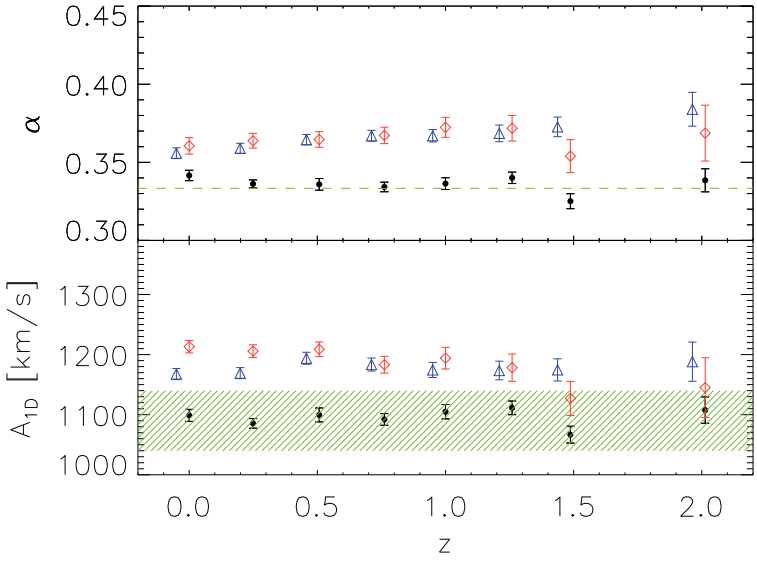

Figure 6.3: Average values of α and A_{1D} (see eq. 6.1) for halos in AGN simulations as a function of redshift, for different tracers, DM particle (black dots), subhalos (red diamonds), and galaxies (blue triangles). The dashed green line in the top panel is the theoretically expected value $\alpha = 1/3$, the horizontal shaded area in the bottom panel indicates the expected theoretical range $A_{1D} = 1040$–1140 (see text). The data of galaxies have been shifted by -0.05 in z for the sake of clarity.

the simulation sets, with $\alpha \simeq 0.36$, the same does not hold for the normalization A_{1D}, this value being smaller when cooling and star formation are included. In each simulation set, the α and A_{1D} values are highest for the subhalos, and lowest for the DM particles, with the values for the galaxies being closer to those of the subhalos.

Both the A_{1D} and the α values we find for the DM particles are in the range of the values listed by Evrard et al. (2008) and coming from the analysis of different simulations (see Table 4 in Evrard et al., 2008), most of which are DM-only. The comparison with Lau et al. (2010) is less straightforward, since they did find a z-dependence of the α parameter for DM particles. Taking an error-weighted average of the values they found at different redshifts, we obtain $A_{1D} = 1103 \pm 2$ km s^{-1}, $\alpha = 0.325 \pm 0.011$ for their non-radiative simulations, and $A_{1D} = 1160 \pm 9$ km s^{-1}, $\alpha = 0.296 \pm 0.012$ for their radiative simulation. Lau et al. (2010)'s σ_{1D}–M_{200} rela-

	A_{1D} (km s^{-1})	α
DM	1094 ± 3.7	0.334 ± 0.0014
NR	1102 ± 3.4	0.336 ± 0.0021
CSF	1081 ± 4.1	0.329 ± 0.0021
AGN	1095 ± 4.4	0.336 ± 0.0015
DM sub	1244 ± 4.7	0.361 ± 0.0027
NR sub	1259 ± 5.3	0.364 ± 0.0030
CSF sub	1166 ± 5.1	0.362 ± 0.0018
AGN sub	1199 ± 5.2	0.365 ± 0.0017
CSF gal	1165 ± 6.7	0.355 ± 0.0025
AGN gal	1177 ± 4.2	0.364 ± 0.0021

Table 6.1: Weighted average values over all redshifts of the parameters A_{1D} and α defining the $\sigma_{1D} - M_{200}$ relation (see eq. (6.1)) for different simulation sets, for DM particles (top table), subhalos (middle table), and galaxies (bottom table).

tions are therefore flatter than ours, particularly so for the radiative simulations. We discuss these differences in Sect. 6.4.

6.3.1 Scatter

An analysis of the scatter of the scaling relations is quite important for cosmological applications. It has been pointed out (see, e.g. Mortonson et al., 2011) that the so called Eddington bias causes the mass function to shift toward higher values of mass if the scatter in the scaling relation between mass and mass proxy is not properly taken into account. Furthermore we want to understand the nature of such scatter, that is whether it is intrinsic or mainly due to statistical uncertainties.

The best fit relation eq. (6.1) has been subtracted from the values of the velocity dispersion of the clusters for each simulation at each redshift. The result for the AGN set at z=0 is shown in Fig. 6.5 for the three tracers. The errors are associated to the biweight average value (Beers et al., 1990). In this figure the distribution of the residuals is also shown, along with the best fit gaussian curves and the reduced χ^2 values of the fits. The residuals appear to be normally distributed, substructures and galaxies having a wider distribution.

The scatter appears to be independent of cluster mass, as well as of redshift and the type of simulation as shown in top panels of Fig. 6.6, the only difference being in the tracer used to build the σ_{1D}–M_{200} relation. When using DM particles the scatter is around 5%, while using substructures or galaxies it is around 12%.

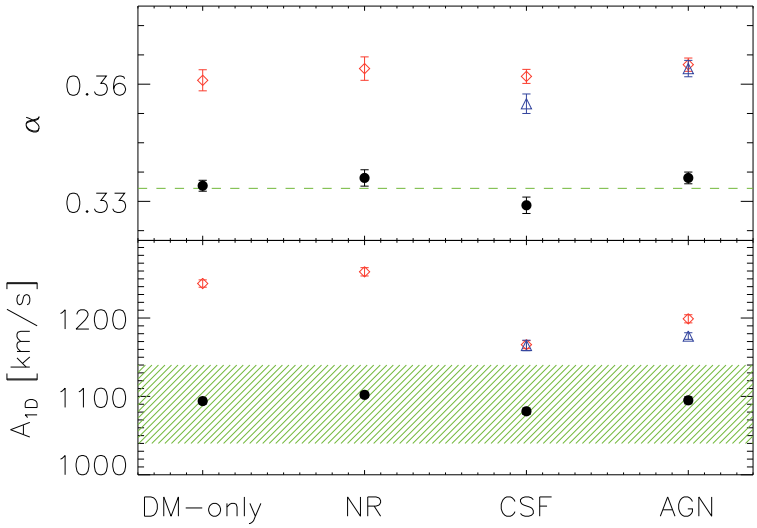

Figure 6.4: Values of α and A_{1D} (see eq. 6.1) averaged over all redshifts for different tracers - DM particle (black dots), subhalos (red diamonds), and galaxies (blue triangles) - for the different types of simulations. The dashed green line in the top panel is the theoretically expected value $\alpha = 1/3$, the horizontal shaded area in the bottom panel indicates the expected theoretical range $A_{1D} = 1040$–1140 (see the text).

In order to understand the nature of the scatter, that is whether it is intrinsic or statistical, we have tried to compute the intrinsic scatter following Williams et al. (2010). Performing a linear fit of the $\log \sigma_{1D} - \log M_{200}$ relation, the intrinsic scatter is considered as a parameter that minimizes $\chi^2 = \sum_{i=1}^{N_{clus}} [y_i - (a \cdot x_i + b)]^2 / [\epsilon_{y,i}^2 + a^2 \cdot \epsilon_{x,i}^2 + \sigma_{int}^2]$, where $y = a \cdot x + b$ is the linear relation, $\epsilon_{x,i}$ and $\epsilon_{y,i}$ are the uncertainties on the x and y quantities and σ_{int} is the intrinsic scatter. In order to estimate the value of the intrinsic scatter and its uncertainty, we performed 1000 bootstrap resamplings of the couples of values $(M_{200}, \text{œ}_{1D})$, each time computing the intrinsic scatter estimate. In a first time, we have evaluated the intrinsic scatter in 4 bins of mass, but we found no mass dependence. Therefore we have evaluated it using all the data. The intrinsic scatter relative to DM particles is 5%, comparable with the total scatter. This means that when using DM particles the scatter in the scaling relation is entirely intrinsic. In fact the values of velocity dispersion evaluated

using DM particles have been obtained using a huge number of objects, hence the statistical uncertainty is very small. On the other hand velocity dispersions estimates using substructures and galaxies are based on relatively small numbers of objects, and statistical uncertainties dominate the scatter. The resulting intrinsic scatter for these tracers turns out to be quite small and consistent with the value found for DM particles.

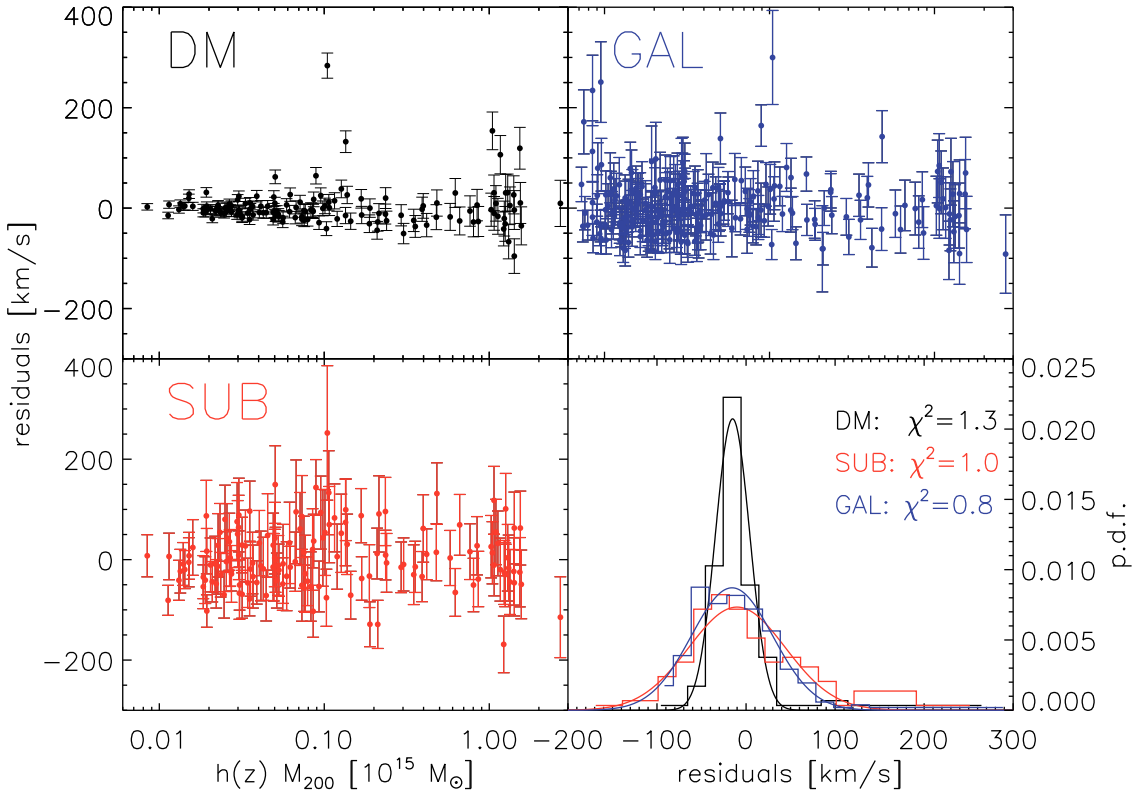

Figure 6.5: Residuals of the velocity dispersion after subtracting the best fit relation eq. (6.1) for the AGN set at z=0, for the three tracers as indicated in the panels. The distributions of residuals for the three tracers is also shown in the bottom right panel, along with the best fit gaussian curves and the reduced χ^2 of the fits.

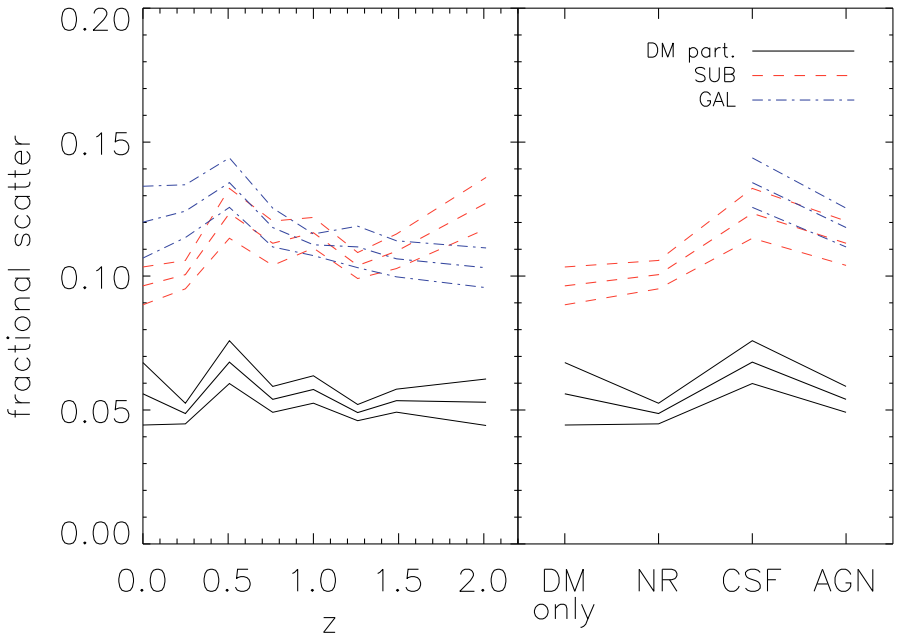

Figure 6.6: *Left panel:* Fractional scatter as a function of redshift in the AGN set. Black solid line refers to the value computed by using DM particles, red dashed and blue dash-dotted by using substructures and galaxies, respectively. The thinner lines are the confidence intervals. *Right panel:* Fractional scatter as a function of the type of simulation at z=0. Lines and colours are the same as in the left panel.

6.3.2 Velocity bias

The difference between the σ_{1D}–M_{200} relations established for DM particles, on one side, and subhalos and galaxies, on the other side implies that subhalos and galaxies have a higher velocity dispersion than DM particles in high mass halos. Since the relation is steeper for subhalos and galaxies than for DM particles, the opposite may occur in halos of low masses. To examine how σ_{1D} changes in halos of different masses when using different implementations of baryonic physics, here we analyse the velocity bias, i.e. the ratio between the velocity dispersions of subhalos (galaxies) and DM particles, $b_v = \sigma_{sub}/\sigma_{DM}$ ($b_v = \sigma_{gal}/\sigma_{DM}$, respectively), for two subsamples of halos, one with masses $h(z)M_{200} < 10^{14} M_\odot$, and the other with masses $h(z)M_{200} > 3 \cdot 10^{14} M_\odot$ (the low- and high-mass samples hereafter). The av-

erage b_v values as a function of redshift are shown in Fig. 6.7 and 6.8, for subhalos and galaxies in different simulation sets, separately for the halos in the low-mass sample (left panels) and for the halos in the high-mass sample (right panels).

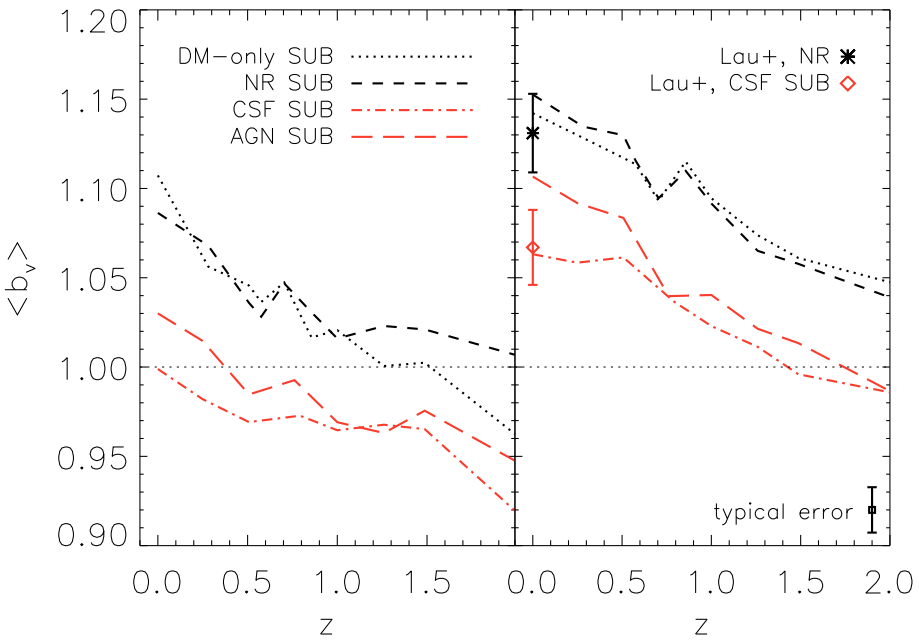

Figure 6.7: Average values of the velocity bias for subhalos, as a function of redshift, for halos in the low-mass sample (left panel) and in the high-mass sample (right panel). Dotted line refers to substructures in the DM set, short black dashed line refers to substructures in the NR set, the other lines refer to substructures of the CSF and AGN sets, as indicated in the legend. Error-bars on the bias values are not shown for the sake of clarity. A typical error-bar is shown at the bottom-right of the right panel. The other points with error bars are the z = 0 values from Lau et al. (2010). The legend in the right panel identifies the different symbols as representative of the non-radiative simulations (NR), and the CSF simulations of Lau et al. (2010).

The bias is on average higher for the high-mass sample halos, and at lower redshifts. A remarkable change in the bias appears when introducing cooling and star formation. In fact the biases are higher for substructures in the DM and in non-radiative simulations (NR) than in the radiative ones (CSF, AGN), both when

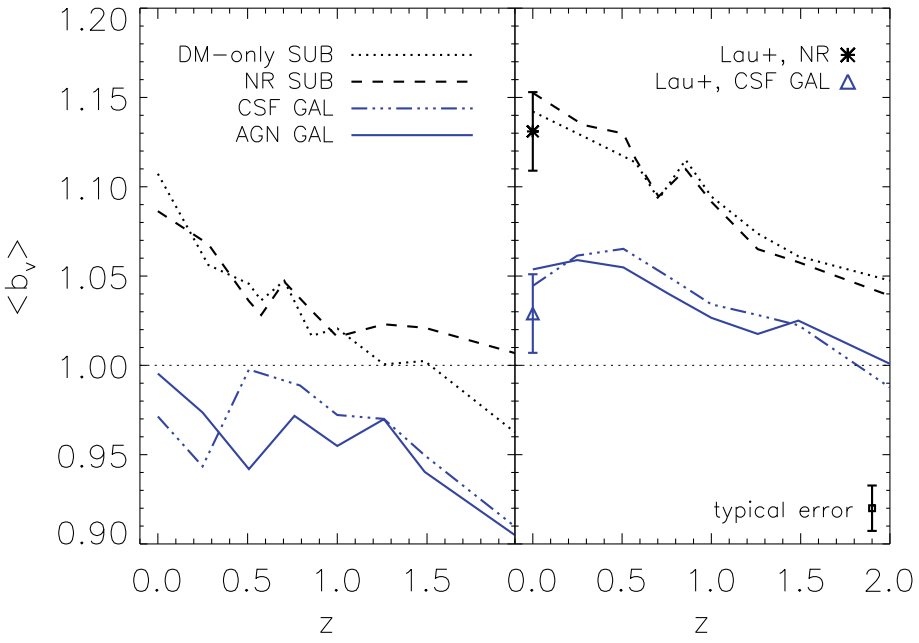

Figure 6.8: Same as Fig. 6.7 but for galaxies rather than substructures.

using substructures and galaxies, reflecting again the importance of the cooling and the feedback processes in the dynamics.

In Fig. 6.7 and 6.8 we also show the values found by Lau et al. (2010). At z = 0, the sample of Lau et al. (2010) and ours have similar mass distributions and there is a good agreement (within the error bars) between their b_v values and ours, separately for the different types of simulations and for the different tracers. The comparison between our data and those in Lau et al. (2010) at $z > 0$ is not shown because it is not straightforward: Lau et al. (2010) follow the same halos at different redshifts by always considering the most massive progenitors of the halos selected at z = 0, whereas we consider all halos above a given mass cut at any given redshift. Taken at face value, the biases they find at higher z are smaller than those we find, and this difference might be related to a strong overcooling present in their simulations, making their subhalos very resistant to tidal disruption.

6.3.3 Dynamical processes in halos

The above results show how the relative kinetic energy content in subhalos (or galaxies) and the diffuse DM component varies with redshift, halo mass, and the type of simulations. Here we provide an interpretation of these results in terms of the dynamical processes that are effective in clusters and groups, i.e. dynamical friction, merging with the central galaxy, tidal disruption, and accretion from the surrounding large-scale structure, and how these processes depend on the physics implemented in the simulations.

A better understanding of the physical cause of the differences in the σ_{1D}-M_{200} relation and of the velocity biases analysed in the two previous sections can be obtained by examining the probability distribution function for the modulus of the velocity of the different tracers. These distributions are shown in Fig. 6.9 for the CSF and AGN simulations, at z = 0 and 1.26, separately for the low- and high-mass samples.

The velocity distribution of DM particles (solid black lines in Fig. 6.9) appears to be single-peaked, but only for the low-mass sample. The DM particle velocity distribution for the high-mass sample is flat-topped and sometimes double-peaked. These features, present in all the different types of simulations, appear to be more pronounced for the velocity distributions of subhalos (dashed red lines) and galaxies (dotted blue lines), and depend on the physics implemented in the simulations. The difference in the velocity distributions of DM particles, subhalos, and galaxies is at the origin of the velocity biases and the differences in their σ_{1D}-M_{200} relations. Hereafter we interpret the effect of the dynamical processes that shape these velocity distributions.

A flat-topped or double-peaked velocity distribution is the signature of ongoing mergers and infall of matter into the halos, which tends to populate the high-velocity part of the velocity distributions (see, e.g. Diemand et al., 2004; Wang et al., 2005; Wetzel, 2011; Ribeiro et al., 2011). With time, the velocity distribution relaxes via phase-mixing and dynamical relaxation and approaches a single Maxwellian (e.g. Faltenbacher and Diemand, 2006; Lapi and Cavaliere, 2011, and references therein).

The relative importance of the relaxed and unrelaxed velocity distributions depends on how strong the matter infall rate is. Higher-mass halos are dynamically younger, and undergo significant matter infall until more recent times than lower-mass halos (e.g. Lapi and Cavaliere, 2009; Faltenbacher and White, 2010). Hence in higher-mass halos the unrelaxed, high-velocity component is more important than in lower-mass clusters, as we see in Fig. 6.9.

The velocity distributions of subhalo and galaxies is different from those of DM particles, because of additional dynamical processes that leave the DM particle distributions unaffected. One is the dynamical friction, leading to a decrease in the orbital energy, hence to an approach to the cluster centre and a decrease in velocity, eventually followed by merger with the central cluster galaxy (e.g. Boylan-Kolchin et al., 2008; Wetzel and White, 2010). The other process is tidal disruption, caused by the integral of tidal interactions leading to mass losses (e.g. Diemand et al., 2004). These two processes are related. On one hand, dynamical friction becomes ineffective when tidal mass losses become important (e.g. Faltenbacher and Mathews, 2007), because dynamical friction is more effective for more massive objects. On the other hand, tidal mass losses are enhanced by dynamical friction, since they are more effective in slow-moving subhalos (and galaxies) than their fast-moving counterparts (Diemand et al., 2004). Hence dynamical friction is likely to be more effective at the first orbit of a subhalo (or galaxy) (Faltenbacher and Mathews, 2007), while tidal disruption may take several orbits.

Dynamical friction tends to increase the low-velocity tail of the distribution. A possible signature of this effect is visible in the velocity distributions of subhalos and galaxies at high-z in Fig. 6.9. On the other hand, the removal of the slowest subhalos (or galaxies) by tidal disruption or merger with the central galaxy tends to decrease the low-velocity tail of the distribution. This is likely to occur in the relaxed component of the global velocity distribution, since subhalos (and galaxies) in the relaxed component have spent more time orbiting their parent halos than the recently infallen, unrelaxed population. The resulting velocity distribution will then appear to be double peaked, one low-velocity peak being due to the relaxed component, depopulated by tidal stripping, and another high-velocity peak due to the infalling population, that has not yet experienced significant tidal mass losses. This is particularly evident in higher-mass halos, in which the infall rate is higher (at given z) than in lower-mass halos. The resulting asymmetric velocity distribution is visible in Fig. 6.9 (dashed red and dotted blue lines).

These processes are dependent on the physical processes and feedback implemented in the simulations. In fact in Fig. 6.9 one can note that the velocity distributions of galaxies and subhalos in the CSF simulation sets are both closer to the velocity distributions of DM particles, than the corresponding ones in the AGN simulation sets. This occurs because baryon cooling tends to make galaxies and subhalos more resistant against tidal disruption (e.g. Weinberg et al., 2008; Lau et al., 2010). However cooling efficiency is reduced in simulations including AGN feedback thus making halos less compact and galaxies more fragile than in the over-cooled CSF simulations.

Yet another difference is visible in Fig. 6.9, namely the velocity distribution for galaxies in the AGN sets is slightly closer to the distribution of DM particles than that of subhalos. This is due to the different mass limit we use to select galaxies and subhalos (see Sect. 6.2). In our samples, subhalos selected by means of total bound mass are on average objects of higher mass than subhalos selected by means of stellar mass, hence they are subject to stronger dynamical friction, slowing them down and making them more easily subject to tidal disruption. Our result is reminiscent of that of Faltenbacher and Diemand (2006) who found that the velocity distribution of galaxies is quite similar to that of DM particles when selecting objects by their mass at accretion, i.e. before tidal stripping operates, as pointed out also by Lau et al. (2010).

The processes so far discussed provide a frame for a better understanding of Fig. 6.7 and 6.8. At fixed galaxy mass, dynamical friction is more efficient in low-mass clusters and at high redshifts, before tidal stripping decreases galaxy masses. Therefore dynamical friction tends to create a velocity bias < 1 in low mass, high-z systems, while leaving almost unaffected high mass clusters. Tidal stripping is more efficient on slow moving galaxies, which are stripped and eventually disrupted (or removed from a mass-limited sample), and operates at all times. This causes an increase of the bias with time. This has the effect of erasing the initial dynamical-friction bias in low-mass clusters and creating a bias > 1 in high-mass clusters as we approach $z = 0$.

An important rôle in these processes may also be played by galaxy orbits. In Fig. 6.10 we show the velocity anisotropy profiles for the different tracers, in low- and high-mass systems, for z=0 and 1.26. For lack of sufficient number of substructures and galaxies in each system, the profiles for these tracers are computed for stacks of all systems, where substructure and galaxy velocities have been scaled by each system v_{200} before stacking. With this procedure, richer clusters weigh more in the final profile. For the DM particles we are not limited by poor statistics, so we derive the anisotropy profiles individually for each halo, and then take an average. For consistency with what was done for the substructures and galaxies, the average is weighted by the number of substructures present in each cluster. Fig. 6.10 shows that orbits are more radially anisotropic in high-mass than in low-mass systems (as already shown by Wetzel, 2011). Understanding the reason for this difference (and for the redshift evolution clearly visible in the same figure) is beyond the scope of this Thesis, although we suspect that it might be related to the younger dynamical age of higher mass clusters (as suggested by, e.g., Biviano and Poggianti, 2009, and references therein). What is relevant in this context is that galaxies on more radial orbits reach closer to the cluster centre and therefore suffer from stronger tidal

stripping effects. The different orbital anisotropy of galaxies contribute to create a higher velocity bias in high-mass relative to low-mass clusters.

6.4 Discussion and conclusions

We determined the σ_{1D}-M_{200} relation for DM particles, subhalos, and galaxies in cluster- and group-sized halos extracted from ΛCDM cosmological simulations. We analysed four sets of simulations carried out for the same halos: one DM-only, one with non-radiative gas, and another two with gas cooling, star formation and galactic ejecta triggered by SN winds, one of the two also including the effect of AGN feedback.

The main results of our analysis can be summarised as follows.

- We confirm that the $\sigma_{1D} - M_{200}$ relations for the DM particles are consistent with the theoretical expectation from the virial relation, assuming NFW halo mass profiles, with reasonable values of concentration and velocity anisotropy.

- The intercepts at $10^{15}M_{\odot}$ and slopes of the logarithmic σ_{1D}-M_{200} relations derived using subhalos and galaxies as tracers of the potential are always higher than those derived using DM particles. We do not find a significant dependence of the σ_{1D}-M_{200} relations on redshift, but we do find a dependence on the kind of simulation, the radiative ones having a higher value of the normalization.

- The σ_{1D}-M_{200} relations for the DM particles are consistent with those found by Evrard et al. (2008). On the other hand the relations we find for all the tracers are steeper than those derived by Lau et al. (2010). This difference might be caused by the narrower halo mass range explored by Lau et al. (2010).

- The differences in the σ_{1D}-M_{200} relations for the different tracers of the halo gravitational potential and for the different physics implemented are due to dynamical processes taking place in the halos. In fact dynamical friction and tidal disruption act on substructures and galaxies but not on DM particles. Dynamical friction slows down a substructure or a galaxy before it suffers mass loss due to tidal stripping. Dynamical friction is therefore more efficient at high-z. It is also more efficient in lower-mass clusters for given galaxy mass. Tidal stripping, on the other hand, is more efficient in higher-mass

clusters, where galaxies move on more radial orbits (hence with smaller pericenter radii). As a result, velocity biases are created in the substructure and galaxy populations, relative to the DM particles, and these biases are ≤ 1 for low-mass systems and ≥ 1 for high-mass systems, and increasing with time, leading to the observed differences in the σ_{1D}-M_{200} relations of different tracers.

- In order to correctly reproduce such processes, a detailed implementation of the baryonic physics must be used in the simulations. In fact the presence of baryonic matter makes halos more resistant against tidal disruption (e.g. Weinberg et al., 2008). In this way in simulations with cooling and star formation there is a higher fraction of survivors among the slow moving subhalos, reflecting in a lower value of the normalization on the σ_{1D}-M_{200} relation.

- We analysed the scatter in the $\sigma_{1D} - M_{200}$ relation, finding a value of around 5% for DM particles and 12% for substructures and galaxies. The intrinsic scatter, after accountinbg for the statistical errors in the σ_{1D} measurements, appears to be $\lesssim 5\%$, independently of the tracer.

Such a small scatter in the $\sigma_{1D} - M_{200}$ relation potentially makes σ_{1D} a very good proxy for the mass, via inversion of eq. (6.1): $M_{200}/10^{15}M_{\odot} = (\sigma_{1D}/A_{1D})^{(1/\alpha)}/h(z)$. However, A_{1D} and α are significantly different for the different tracers (DM particles, substructures, galaxies). Using the values obtained for one tracer to infer cluster masses from the σ_{1D} of a different tracer can lead to systematic errors of up to $\sim 30\%$. In comparison, the effect of using different baryonic physics for the same tracer has a much smaller effect on the mass estimates obtained from σ_{1D} ($\lesssim 7\%$, see Table 6.2). The presence of scatter, even though small, makes possible the applicability of the scaling relation only in a statistical sense, not for mass estimates of single objects.

The results presented in this chapter show that good knowledge of the $\sigma_{1D} - M_{200}$ relation in 6D phase space is fundamental before one could apply this relation to observational samples. Projection effects and the presence of interlopers can significantly affect the accuracy and reliability of the mass estimate (e.g. Cen, 1997; Biviano et al., 2006). We plan to consider these effects in detail, in a forthcoming work, using simulations with a proper implementation of baryonic physics and galaxies as tracers.

simulation	tracer	$\sigma_{1D} = 300$ km/s	$\sigma_{1D} = 900$ km/s
DM	DM part	0.029	0.774
NR	DM part	0.029	0.760
CSF	DM part	0.028	0.796
AGN	DM part	0.029	0.775
DM	sub	0.027	0.567
NR	sub	0.027	0.552
CSF	sub	0.033	0.679
AGN	sub	0.031	0.633
CSF	gal	0.030	0.671
AGN	gal	0.032	0.665

Table 6.2: Masses (in $10^{15}M_{\odot}$) of clusters at z=0 predicted from the $\sigma_{1D} - M_{200}$ relation for two values of σ_{1D}, 300 m/s and 900 m/s.

6.5 Appendix: plots for other models

In this appendix we report the plots showing the redshift dependence of the slope and the intercept of eq. (6.1) as well as the velocity distributions of the tracers for all simulation sets not already shown before in the main text.

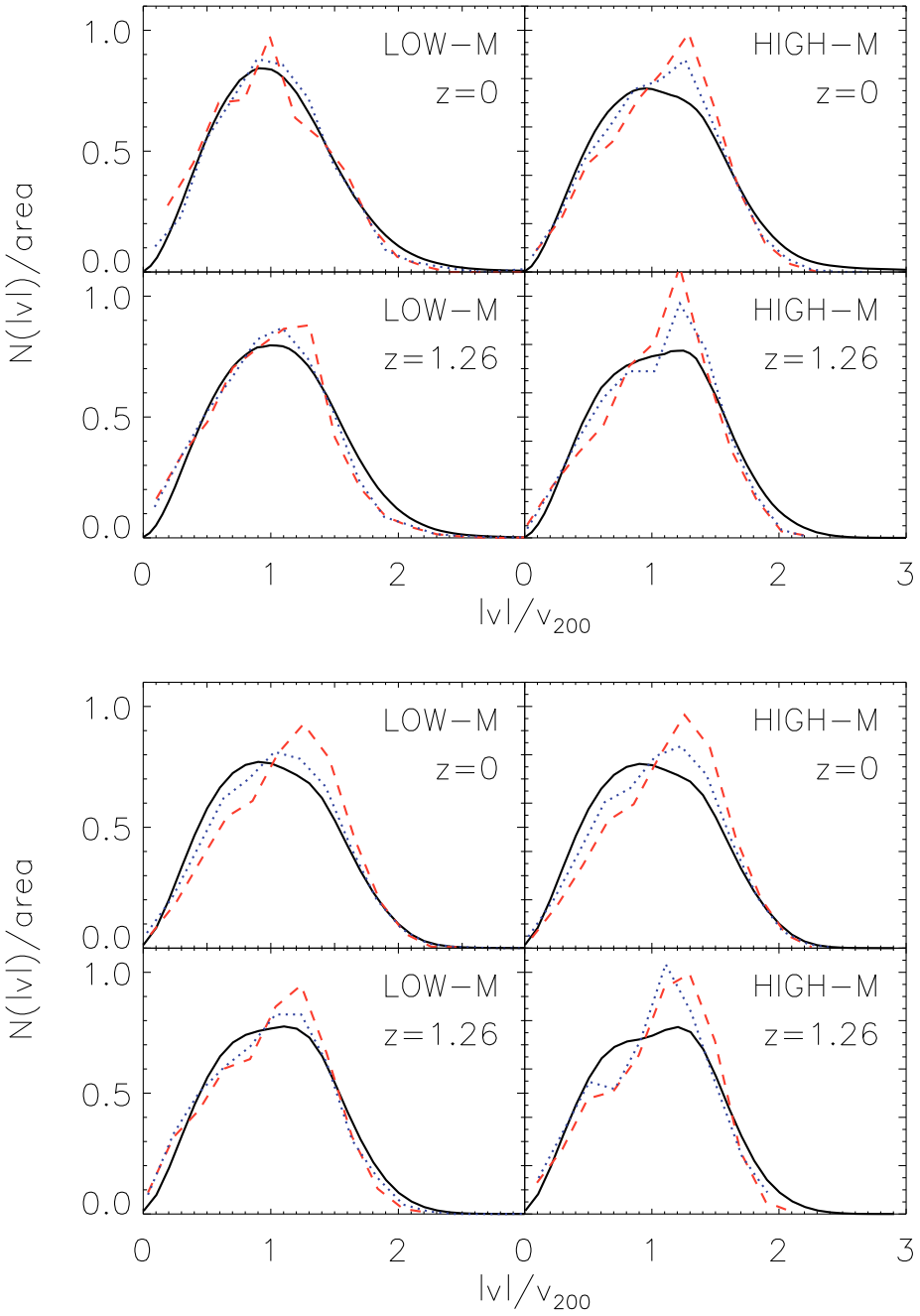

Figure 6.9: *Top panels:* The velocity distributions for the CSF simulations for the low-mass sample (left panels) and the high-mass sample (right panels) at $z = 0$ (top panels) and $z = 1.26$ (bottom panels) for DM particles (solid black lines), subhalos (dashed red lines) and galaxies (dotted blue lines). All distributions are normalised to their integrals. *Bottom panels:* same as top panels but for the AGN simulations.

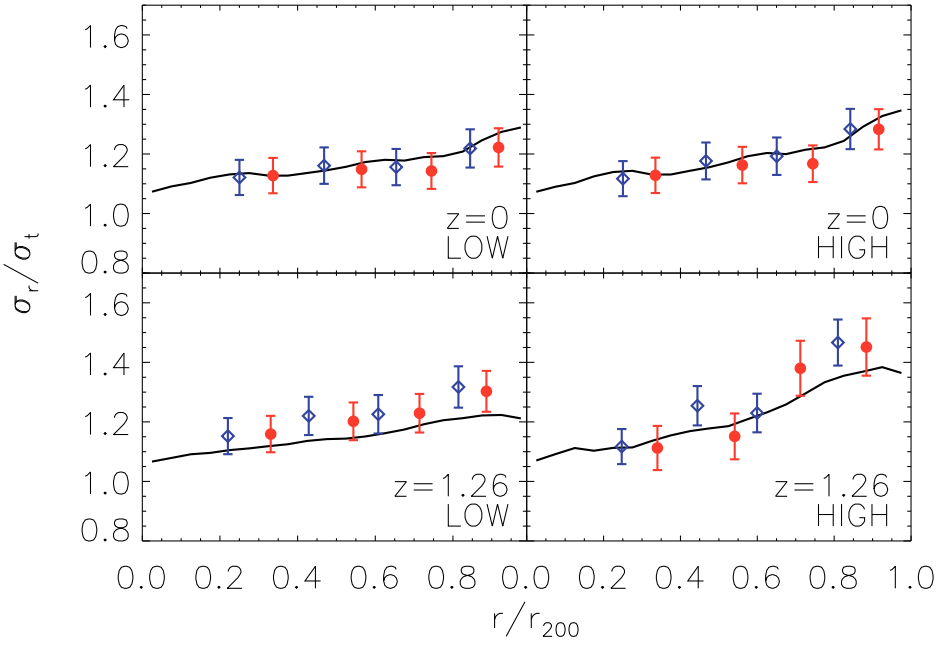

Figure 6.10: Velocity anisotropy as a function of the cluster center, for the AGN set. Top panels refer to z=0, bottom panels to z=1.26. Panels on the left are relative to the low-mass sample, panels on the right to the high-mass sample. Red points refer to the results obtained using subhalos, while blue diamonds using galaxies. The four bins are built in such a way that within each bin there is the same number of objects. Galaxies diamonds have been shifted by -0.05 in redshift for the sake of clarity. The black solid line refers to the results obtained using DM particles.

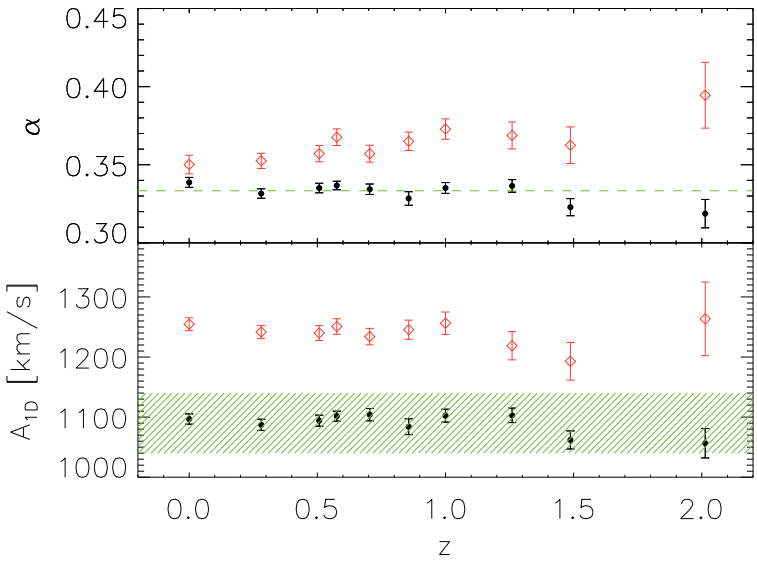

Figure 6.11: Same as Fig. 6.3 for the DM set.

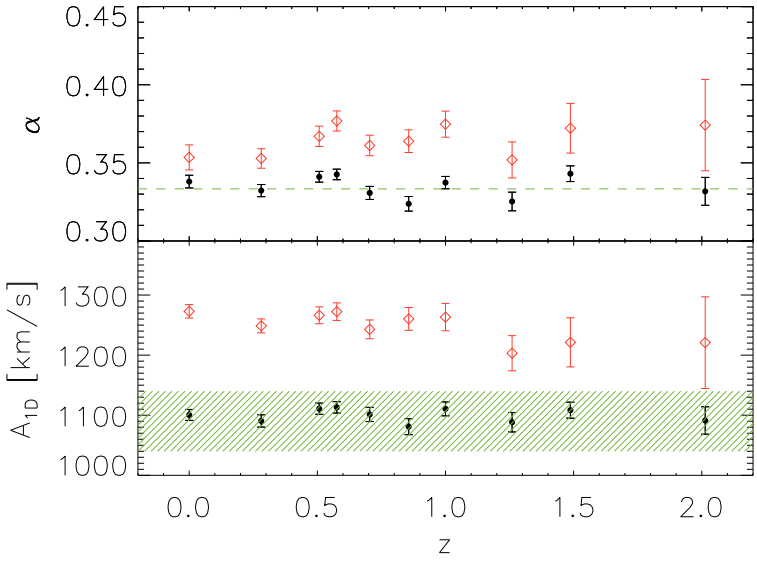

Figure 6.12: Same as Fig. 6.3 for the NR set.

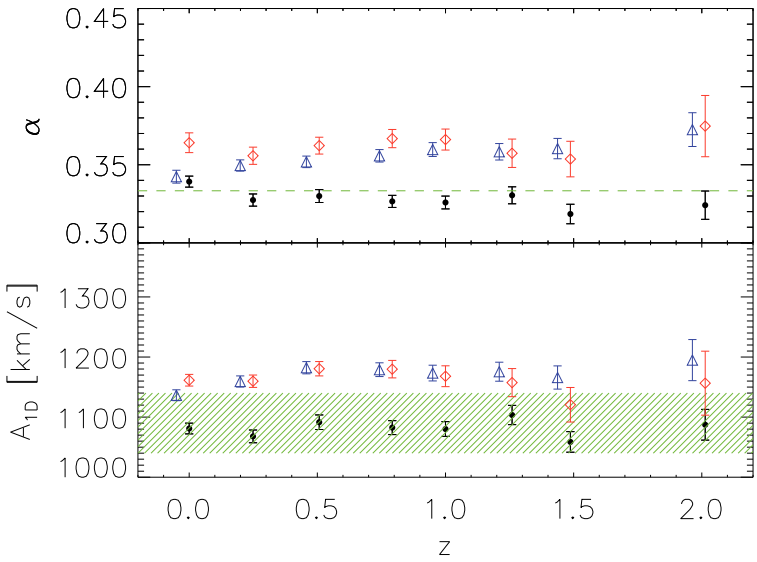

Figure 6.13: Same as Fig. 6.3 for the CSF set.

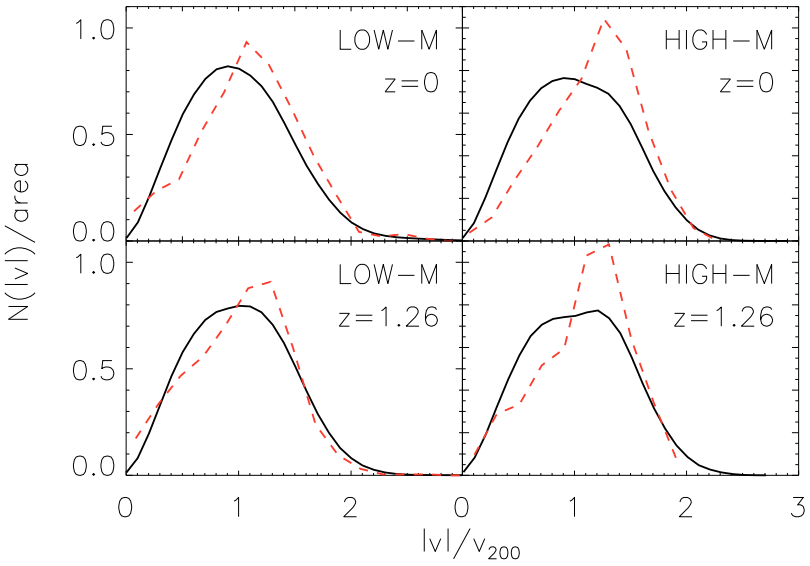

Figure 6.14: Same as Fig. 6.9 for the DM set.

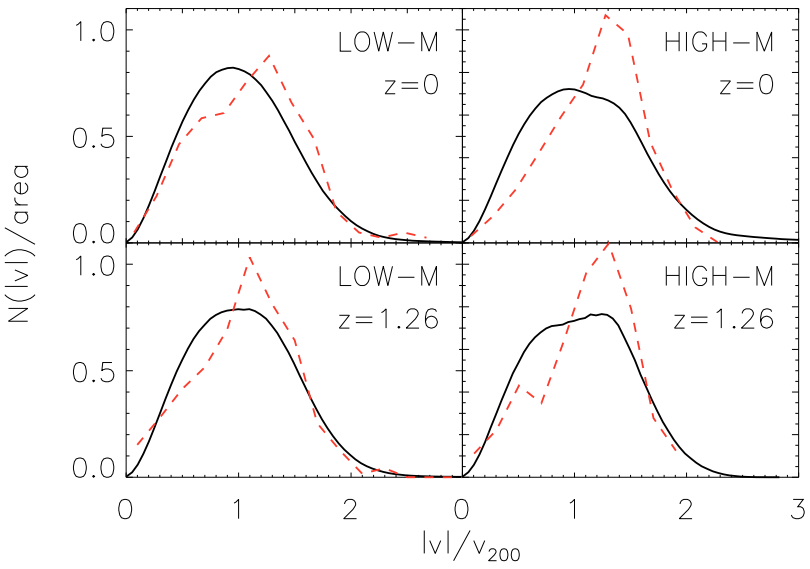

Figure 6.15: Same as Fig. 6.9 for the NR set.

7

Conclusions

The main focus of this Thesis concerns the study of the internal dynamics of galaxy clusters, and the information on the galaxy cluster mass content it can provide. Cluster mass has proven to be an important tool for cosmological studies (see Sect. 2.6), the main problem being that it is not a directly observable quantity. In particular, I have highlighted how the estimates of the mass and the pseudo phase space density profile of galaxy clusters, obtained from dynamical information, are affected when taking into account the presence of baryons and according to the tracer of the gravitational potential adopted.

More in detail, the following aspects are studied and discussed in this Thesis.

Mass, velocity anisotropy and pseudo phase–space density profiles of a nearby cluster

High quality photometric and spectroscopic data are available for a large number of galaxies in the cluster A2142. Taking advantage of these data, we computed the mass and velocity anisotropy profiles for this cluster. The mass profile has been obtained by using three techniques based on the kinematics of member galaxies, namely the caustic method, the method of Dispersion - Kurtosis and MAMPOSSt. The mass profile determinations, as well as the virial values of mass and radius, obtained with the different techniques, are in agreement with each other and with the estimates from X-ray and weak lensing studies. Our final measurement of the cluster mass profile is obtained by averaging the lensing, X-ray and kinematics determinations. The cluster mass profile is well fit by an NFW profile with concen-

tration parameter $c = 4.0 \pm 0.5$.

Through the inversion of the Jeans equation we computed the velocity anisotropy profiles. The populations of red and blue galaxies appear to have different velocity anisotropies, with red galaxies being almost isotropic while blue galaxies are radially anisotropic, with a weak dependence on radius.

The pseudo phase–space density profile $Q(r)$ for the red galaxy population agrees with the theoretical results found in cosmological N–body simulations. The relation between the velocity anisotropy β and the logarithmic slope γ of the density profile matches the theoretical relation only in the inner region when considering the red galaxies. The deviations might be due to the theoretical relations not taking into account the presence of baryons and using DM particles as tracers.

The comparison of the PPSD profile of A2142 with that of another cluster, MACS1206, reveals a different behaviour of the blue galaxy population. MACS1206 presents, in fact, agreement with the theoretical relation also for the blue population. This suggests that the PPSD profile might provide a tool to investigate the dynamical history of galaxy clusters. If a major merging happened recently, the process of violent relaxation should be able to lead also blue galaxies to equilibrium, resulting consequently in a PPSD like the MACS1206's one. On the other hand, if a cluster has not undergone a major merging event since long, then the blue galaxies we observe are those only recently accreted. For this population, the PPSD would then look like the one of A2142.

The role of the tracer and the baryonic physics in the velocity dispersion − mass scaling relation

In Chapter 6 I presented an analysis of the relation between the masses of cluster- and group-sized halos, extracted from ΛCDM cosmological N-body and hydrodynamic simulations, and their velocity dispersions, at different redshifts from $z = 2$ to $z = 0$. The main aim of this analysis is to understand how the implementation of baryonic physics in simulations affects such relation, i.e. to what extent the use of the velocity dispersion as a proxy for cluster mass determination is hampered by the imperfect knowledge of the baryonic physics. In our analysis we use several sets of simulations with different physics implemented: one DM-only simulation, one simulation with non-radiative gas, and two radiative simulations, one of which with feedback from Active Galactic Nuclei. Velocity dispersions are determined using three different tracers, dark matter particles, subhalos, and galaxies.

We confirm that DM particles trace a relation that is fully consistent with the theoretical expectations based on the virial theorem, $\sigma_v \propto M^\alpha$ with $\alpha = 1/3$, and

with previous results presented in the literature. On the other hand, subhalos and galaxies trace steeper relations, with velocity dispersion scaling with mass with $\alpha > 1/3$, and with larger values of the normalization. Such relations imply that galaxies and subhalos have a ~ 10 per cent velocity bias relative to the DM particles, which can be either positive or negative, depending on halo mass, redshift and physics implemented in the simulation.

We explain these differences as due to dynamical processes, namely dynamical friction and tidal disruption, acting on substructures and galaxies, but not on DM particles. These processes appear to have different efficiencies, depending on the halo mass and the importance of gas cooling, and may create a non-trivial dependence of the velocity bias and the σ_{1D}–M_{200} relation on the tracer, the halo mass and its redshift.

These results are relevant in view of the application of velocity dispersion as a proxy for cluster masses in ongoing and future large galaxy redshift surveys.

Future perspectives

Recent studies (see e.g. Saro et al., 2012; Wojtak et al., 2013) have shown that the velocities of DM particles in a cluster are strongly correlated with the triaxiality of a cluster halo. The line of sight velocity dispersion therefore depends on the angle between the line of sight and the halo major axis. If these two directions are aligned, the velocity dispersion appears to be at its maximum value. The minimum value is instead obtained when observing in the direction of the minor axis. Therefore clusters will appear to have a larger kinetic energy content when observed along their major axis, and a smaller one when observed along their minor axis. Translating the kinetic energy content into mass, cluster masses will therefore be over– or under–estimated, depending on their orientation in the space with respect to the observer.

Using hydrodynamical simulations, in order to take into account the possible effect of baryonic physics, it is possible to quantify this effect. Moreover, it is useful to use mock catalogues built by tracing light cones that mimic an observation (see e.g. Merson et al., 2013, for the creation of light cones). In this way it is possible to take into account the projection effects that constitute another important source of scatter in the relation between velocity dispersion and cluster mass. The knowledge of the "true" value of mass in the mock catalogues makes possible to quantify the impact of such phenomena on cluster mass estimate and allows us to characterise their impact on the final mass estimate, providing a powerful tool for the future observations. Galaxies have to be used as tracers of the dynamics

of simulated clusters, rather than DM particles, since the use of the wrong tracer can induce important differences in the kinematics, as we have shown in chapter 6. Furthermore, the impact of a wrong choice of the cluster center, or the presence of merging structures, are expected to significantly affect measurement of total mass and of mass profiles. The idea is to correct the observed velocity dispersion according to the observed shape of the BCG, or using some other observable quantity that bears the information on the shape of the halos (e.g. the projected distribution of cluster members). This work would provide a useful tool for single cluster mass measurement, helping to improve its reliability. Also, in a large survey like Euclid, it could provide a tool for reducing the scatter in the scaling relation between velocity dispersion and mass. In fact clusters are randomly oriented in space, therefore sometimes they will be observed along a direction close to their major axis, and sometimes along a direction close to their minor axis.

For the same reasons, also the PPSD profile is affected by the triaxiality of the halos, and the impact on the observational estimates can be addressed via numerical simulations. Interesting observational perspectives are offered by the Euclid mission.

The studies about the PPSD carried out so far have focused on the DM–only systems. In chapter 6 I showed that the inclusion of baryonic physics in simulations affects the kinematics of galaxies. A first question comes natural: how do baryons affect the PPSD? Of course real systems do have baryons, therefore the study of how this component affects the PPSD profile is the next step in this field. Another result presented in chapter 6 is that galaxies are biased tracers of the internal kinematics. DM particles and galaxies undergo different dynamical processes, causing these two components to behave differently. Therefore the PPSDs computed using different tracers of the internal dynamics are expected to be different. Although the use of DM particles provides full information on the phase space of the system, DM particles are not observable, while galaxies are. Still, the present studies in this field rely on the analysis of the DM particles. Therefore the study of how galaxy kinematics affects the PPSD is a necessary step toward the study of the PPSD in real systems. These issues can be addressed by means of numerical simulations. Using a set of hydrosimulations with different implementation of the baryonic physics would allow us to understand the contribution of the different processes implemented to the dynamics of the systems.

A process that acts in shaping the pseudo phase space density is the merging between galaxy clusters. As seen in Sect. 5.7, from the comparison of the PPSD profiles of two different clusters it appears that the PPSD might provide information about the dynamical state of galaxy clusters, in particular on the time elapsed

since the last major merger event. In fact, these events of merging can settle the equilibrium of the structure via the so–called *violent relaxation*. Blue galaxies, that usually are not expected to constitute a population of relaxed objects, appear to be in equilibrium as well. On the other hand, systems that underwent a major merging long time ago had time to transform blue galaxies into red ones, and the population of blue galaxies is a recently accreted one, not yet in equilibrium. Since merging is a process that influences clusters, inferring the time elapsed since the last significant event of merging would provide a valuable tool to trace the past history of the hierarchical assembly of clusters. Using simulations, it is possible to follow the history of galaxy clusters by building the *merger trees*. In fact the history of each object is stored, and the time elapsed since an event of merging can be easily recovered. In this way it is possible to study how the PPSD changes when a merging event takes place: mass of the merging systems, time since the merging, orbits of galaxies are all quantities that have to be characterized in relation to the change of the PPSD.

Euclid will result very useful for investigating the PPSD profiles of real systems. Accurate estimates on the density profiles on scales larger than $\sim 100\,kpc$ will be obtained thanks to the Euclid high quality images that allow to detect both the strong and the weak lensing signals.

Statistics is the main difference in the approaches adopted in the studies presented in chapters 5 and 6. A high number of spectroscopic data providing a good estimate of the line–of–sight velocity of galaxies is in fact compulsory for studies like the ones we performed on A2142. Such a rich high quality data–set is currently available only for nearby objects.

The CLASH collaboration[1] makes use of the observation of 25 massive galaxy clusters with HST's Wide-field Camera 3 (WFC3) and the Advanced Camera for Surveys (ACS), and has begun a spectroscopic follow-up on 12 of them with the VLT. The sample redshift ranges from $z = 0.15$ up to $z = 0.9$ (with a median of $z \sim 0.4$), covering the mass range $5 - 30 \cdot 10^{14} M_{\odot}$. For one of these clusters, a study on the internal dynamics and the PPSD has already been performed (Biviano et al., 2013). The dynamical analysis will be extended to the other clusters in the near future, providing detailed information although only for few objects.

Specifically projected spectrographs for IR observations (e.g. KMOS[2]) will allow to study the distant Universe, while the development of new spectrographs

[1] http://www.stsci.edu/ postman/CLASH/Home.html
[2] http://www.eso.org/sci/facilities/develop/instruments/kmos.html

able to analyse several sources (MOS: *Multi Object Spectrograph*, e.g. WEAVE[3]) will allow to measure the velocities of cluster galaxies with high precision also in the inner regions of clusters. In this way a detailed study of the internal dynamics of clusters is possible. Precise measurements of the velocity distribution of galaxies is necessary for an accurate analysis of the PPSD profile. The lensing and X–ray analyses also play an important role in this field, as they tighten the constraints of the density profile.

The future directions of development on the study of the internal dynamics of galaxy clusters outlined in this section are meant to investigate important aspects of galaxy clusters, providing an invaluable source of information on the collapse process, allowing to constrain the cosmological framework as well as to better understand the processes that affect the formation and evolution of galaxies.

[3]http://www.ing.iac.es/weave/index.html

Bibliography

G. O. Abell. The Distribution of Rich Clusters of Galaxies. *ApJS*, 3:211, May 1958. doi: 10.1086/190036.

H. Akamatsu, A. Hoshino, Y. Ishisaki, T. Ohashi, K. Sato, Y. Takei, and N. Ota. X-Ray Study of the Outer Region of Abell 2142 with Suzaku. *PASJ*, 63:1019, November 2011.

S. W. Allen, A. E. Evrard, and A. B. Mantz. Cosmological Parameters from Observations of Galaxy Clusters. *ARAA*, 49:409–470, September 2011. doi: 10.1146/annurev-astro-081710-102514.

AMI Consortium, C. Rodríguez-Gonzálvez, T. W. Shimwell, M. L. Davies, F. Feroz, T. M. O. Franzen, K. J. B. Grainge, M. P. Hobson, N. Hurley-Walker, A. N. Lasenby, M. Olamaie, G. Pooley, R. D. E. Saunders, A. M. M. Scaife, M. P. Schammel, P. F. Scott, D. J. Titterington, and E. M. Waldram. Detailed Sunyaev-Zel'dovich study with AMI of 19 LoCuSS galaxy clusters: masses and temperatures out to the virial radius. *MNRAS*, 425:162–203, September 2012. doi: 10.1111/j.1365-2966.2012.21419.x.

S. Andreon, E. Puddu, R. de Propris, and J.-C. Cuillandre. Galaxy evolution in the high-redshift, colour-selected cluster RzCS 052 at z = 1.02. *MNRAS*, 385:979–985, April 2008. doi: 10.1111/j.1365-2966.2008.12890.x.

M. Arnaud and A. E. Evrard. The L_X-T relation and intracluster gas fractions of X-ray clusters. *MNRAS*, 305:631–640, May 1999. doi: 10.1046/j.1365-8711.1999.02442.x.

M. Arnaud, E. Pointecouteau, and G. W. Pratt. Calibration of the galaxy cluster M{500}-Y{X} relation with XMM-Newton. *A&A*, 474:L37–L40, November 2007. doi: 10.1051/0004-6361:20078541.

S. Arnouts, D. Schiminovich, O. Ilbert, L. Tresse, B. Milliard, M. Treyer, S. Bardelli, T. Budavari, T. K. Wyder, E. Zucca, O. Le Fèvre, D. C. Martin, G. Vettolani, C. Adami, M. Arnaboldi, T. Barlow, L. Bianchi, M. Bolzonella, D. Bottini, Y.-I. Byun, A. Cappi, S. Charlot, T. Contini, J. Donas, K. Forster, S. Foucaud, P. Franzetti, P. G. Friedman, B. Garilli, I. Gavignaud, L. Guzzo, T. M. Heckman, C. Hoopes, A. Iovino, P. Jelinsky, V. Le Brun, Y.-W. Lee, D. Maccagni, B. F. Madore, R. Malina, B. Marano, C. Marinoni, H. J. McCracken, A. Mazure, B. Meneux, R. Merighi, P. Morrissey, S. Neff, S. Paltani, R. Pellò, J. P. Picat, A. Pollo, L. Pozzetti, M. Radovich, R. M. Rich, R. Scaramella, M. Scodeggio, M. Seibert, O. Siegmund, T. Small, A. S. Szalay, B. Welsh, C. K. Xu, G. Zamorani, and A. Zanichelli. The GALEX VIMOS-VLT Deep Survey Measurement of the Evolution of the 1500 Å Luminosity Function. *ApJ*, 619:L43–L46, January 2005. doi: 10.1086/426733.

N. A. Bahcall, T. A. McKay, J. Annis, R. S. J. Kim, F. Dong, S. Hansen, T. Goto, J. E. Gunn, C. Miller, R. C. Nichol, M. Postman, D. Schneider, J. Schroeder, W. Voges, J. Brinkmann, and M. Fukugita. A Merged Catalog of Clusters of Galaxies from Early Sloan Digital Sky Survey Data. *ApJS*, 148:243–274, October 2003. doi: 10.1086/377167.

M. L. Balogh, J. F. Navarro, and S. L. Morris. The Origin of Star Formation Gradients in Rich Galaxy Clusters. *ApJ*, 540:113–121, September 2000. doi: 10.1086/309323.

M. L. Balogh, F. R. Pearce, R. G. Bower, and S. T. Kay. Revisiting the cosmic cooling crisis. *MNRAS*, 326:1228–1234, October 2001. doi: 10.1111/j.1365-8711.2001.04667.x.

R. Barrena, M. Ramella, W. Boschin, M. Nonino, A. Biviano, and E. Mediavilla. VGCF detection of galaxy systems at intermediate redshifts. *A&A*, 444:685–695, December 2005. doi: 10.1051/0004-6361:20053449.

M. Bartelmann, M. Limousin, M. Meneghetti, and R. Schmidt. Internal Cluster Structure. *Springer Space Science Reviews*, 177:3–29, August 2013. doi: 10.1007/s11214-013-9977-6.

T.C. Beers, K. Flynn, and K. Gebhardt. Measures of location and scale for velocities in clusters of galaxies - A robust approach. *aj*, 100:32–46, 1990. doi: 10.1086/115487.

A. A. Berlind, J. Frieman, D. H. Weinberg, M. R. Blanton, M. S. Warren, K. Abazajian, R. Scranton, D. W. Hogg, R. Scoccimarro, N. A. Bahcall, J. Brinkmann, J. R. Gott, III, S. J. Kleinman, J. Krzesinski, B. C. Lee, C. J. Miller, A. Nitta, D. P. Schneider, D. L. Tucker, I. Zehavi, and SDSS Collaboration. Percolation Galaxy Groups and Clusters in the SDSS Redshift Survey: Identification, Catalogs, and the Multiplicity Function. *ApJS*, 167:1–25, November 2006. doi: 10.1086/508170.

M. Bernardi, J. B. Hyde, R. K. Sheth, C. J. Miller, and R. C. Nichol. The Luminosities, Sizes, and Velocity Dispersions of Brightest Cluster Galaxies: Implications for Formation History. *AJ*, 133:1741–1755, April 2007. doi: 10.1086/511783.

J. Binney and G. A. Mamon. M/L and velocity anisotropy from observations of spherical galaxies, or must M87 have a massive black hole. *MNRAS*, 200:361–375, July 1982.

J. Binney and S. Tremaine. *Galactic Dynamics*. Princeton University Press, 1987.

J. Binney and S. Tremaine. *Galactic Dynamics: (Second Edition)*. Princeton Series in Astrophysics. Princeton University Press, 2011. ISBN 9781400828722.

A. Biviano. Galaxy systems in the optical and infrared. *ArXiv e-prints*, November 2008.

A. Biviano and M. Girardi. The Mass Profile of Galaxy Clusters out to ˜2r_{200}. *ApJ*, 585:205–214, March 2003. doi: 10.1086/345893.

A. Biviano and P. Katgert. The eso nearby abell cluster survey. *A&A*, 424(3):779–791, 2004.

A. Biviano and B. M. Poggianti. The orbital velocity anisotropy of cluster galaxies: evolution. *A&A*, 501(2):419–427, 2009.

A. Biviano, P. Katgert, T. Thomas, and C. Adami. The ESO Nearby Abell Cluster Survey. XI. Segregation of cluster galaxies and subclustering. *A&A*, 387:8–25, May 2002. doi: 10.1051/0004-6361:20020340.

A. Biviano, G. Murante, S. Borgani, A. Diaferio, K. Dolag, and M. Girardi. On the efficiency and reliability of cluster mass estimates based on member galaxies. *A&A*, 456:23–36, September 2006. doi: 10.1051/0004-6361:20064918.

A. Biviano, P. Rosati, I. Balestra, A. Mercurio, M. Girardi, M. Nonino, C. Grillo, M. Scodeggio, D. Lemze, D. Kelson, K. Umetsu, M. Postman, A. Zitrin, O. Czoske, S. Ettori, A. Fritz, M. Lombardi, C. Maier, E. Medezinski, S. Mei, V. Presotto, V. Strazzullo, P. Tozzi, B. Ziegler, M. Annunziatella, M. Bartelmann, N. Benitez, L. Bradley, M. Brescia, T. Broadhurst, D. Coe, R. Demarco, M. Donahue, H. Ford, R. Gobat, G. Graves, A. Koekemoer, U. Kuchner, P. Melchior, M. Meneghetti, J. Merten, L. Moustakas, E. Munari, E. Regős, B. Sartoris, S. Seitz, and W. Zheng. CLASH-VLT: The mass, velocity-anisotropy, and pseudo-phase-space density profiles of the z = 0.44 galaxy cluster MACS J1206.2-0847. *A&A*, 558:A1, October 2013. doi: 10.1051/0004-6361/201321955.

H. Boehringer and N. Werner. X-ray Spectroscopy of Galaxy Clusters. *ArXiv e-prints*, July 2009.

H. Böhringer, G. W. Pratt, M. Arnaud, S. Borgani, J. H. Croston, T. J. Ponman, S. Ameglio, R. F. Temple, and K. Dolag. Substructure of the galaxy clusters in the REXCESS sample: observed statistics and comparison to numerical simulations. *A&A*, 514:A32, May 2010. doi: 10.1051/0004-6361/200913911.

A. Bonafede, K. Dolag, F. Stasyszyn, G. Murante, and S. Borgani. A non-ideal magnetohydrodynamic GADGET: simulating massive galaxy clusters. *MNRAS*, 418:2234–2250, December 2011. doi: 10.1111/j.1365-2966.2011.19523.x.

J. R. Bond, S. Cole, G. Efstathiou, and N. Kaiser. Excursion set mass functions for hierarchical Gaussian fluctuations. *ApJ*, 379:440–460, October 1991. doi: 10.1086/170520.

S. Borgani. Cosmology with Clusters of Galaxies. In M. Plionis, O. López-Cruz, and D. Hughes, editors, *A Pan-Chromatic View of Clusters of Galaxies and the Large-Scale Structure*, volume 740 of *Lecture Notes in Physics, Berlin Springer Verlag*, page 287, 2008. doi: 10.1007/978-1-4020-6941-3_9.

S. Borgani and A. Kravtsov. Cosmological simulations of galaxy clusters. *ArXiv e-prints*, June 2009.

S. Borgani and A. Kravtsov. Cosmological simulations of galaxy clusters. *Adv. Sci. Letters*, 4:204–227, June 2011.

S. Borgani, G. Murante, V. Springel, A. Diaferio, K. Dolag, L. Moscardini, G. Tormen, L. Tornatore, and P. Tozzi. X-ray properties of galaxy clusters and groups

from a cosmological hydrodynamical simulation. *MNRAS*, 348:1078–1096, March 2004. doi: 10.1111/j.1365-2966.2004.07431.x.

R. G. Bower, J. R. Lucey, and R. S. Ellis. Precision Photometry of Early Type Galaxies in the Coma and Virgo Clusters - a Test of the Universality of the Colour / Magnitude Relation - Part Two - Analysis. *MNRAS*, 254:601, February 1992.

R. G. Bower, F. J. Castander, R. S. Ellis, W. J. Couch, and H. Boehringer. A dynamical study of optically selected distant clusters. *MNRAS*, 291:353, November 1997.

M. Boylan-Kolchin, C.-P. Ma, and E. Quataert. Dynamical friction and galaxy merging time-scales. *MNRAS*, 383:93–101, January 2008. doi: 10.1111/j.1365-2966.2007.12530.x.

G. L. Bryan and M. L. Norman. Statistical Properties of X-Ray Clusters: Analytic and Numerical Comparisons. *ApJ*, 495:80–+, March 1998. doi: 10.1086/305262.

K. Bundy, R. S. Ellis, C. J. Conselice, J. E. Taylor, M. C. Cooper, C. N. A. Willmer, B. J. Weiner, A. L. Coil, K. G. Noeske, and P. R. M. Eisenhardt. The Mass Assembly History of Field Galaxies: Detection of an Evolving Mass Limit for Star-Forming Galaxies. *ApJ*, 651:120–141, November 2006. doi: 10.1086/507456.

A. Burkert. The Structure of Dark Matter Halos in Dwarf Galaxies. *ApJ*, 447:L25, July 1995. doi: 10.1086/309560.

H. Butcher and A. Oemler, Jr. The evolution of galaxies in clusters. I - ISIT photometry of C1 0024+1654 and 3C 295. *ApJ*, 219:18–30, January 1978. doi: 10.1086/155751.

H. V. Capelato, D. Gerbal, E. Salvador-Sole, G. Mathez, A. Mazure, and H. Sol. On the luminosity-segregation in rich clusters of galaxies Application to Coma. *ApJ*, 241:521–527, October 1980. doi: 10.1086/158366.

J. E. Carlstrom, G. P. Holder, and E. D. Reese. Cosmology with the Sunyaev-Zel'dovich Effect. *ARAA*, 40:643–680, 2002. doi: 10.1146/annurev.astro.40.060401.093803.

R. Cen. Toward understanding galaxy clusters and their constituents: Projection effects on velocity dispersion, x-ray emission, mass estimates, gas fraction, and substructure. *ApJ*, 485:39–+, August 1997.

G. Chabrier. Galactic Stellar and Substellar Initial Mass Function. *PASP*, 115:763–795, July 2003. doi: 10.1086/376392.

S. Chandrasekhar. Dynamical Friction. I. General Considerations: the Coefficient of Dynamical Friction. *ApJ*, 97:255, March 1943. doi: 10.1086/144517.

C. Chiappini, F. Matteucci, and R. Gratton. The Chemical Evolution of the Galaxy: The Two-Infall Model. *ApJ*, 477:765, March 1997. doi: 10.1086/303726.

M. Cirasuolo, J. Afonso, R. Bender, P. Bonifacio, C. Evans, L. Kaper, E. Oliva, L. Vanzi, M. Abreu, E. Atad-Ettedgui, C. Babusiaux, F. E. Bauer, P. Best, N. Bezawada, I. R. Bryson, A. Cabral, K. Caputi, M. Centrone, F. Chemla, A. Cimatti, M.-R. Cioni, G. Clementini, J. Coelho, E. Daddi, J. S. Dunlop, S. Feltzing, A. Ferguson, H. Flores, A. Fontana, J. Fynbo, B. Garilli, A. M. Glauser, I. Guinouard, J.-F. Hammer, P. R. Hastings, H.-J. Hess, R. J. Ivison, P. Jagourel, M. Jarvis, G. Kauffman, A. Lawrence, D. Lee, G. Li Causi, S. Lilly, D. Lorenzetti, R. Maiolino, F. Mannucci, R. McLure, D. Minniti, D. Montgomery, B. Muschielok, K. Nandra, R. Navarro, P. Norberg, L. Origlia, N. Padilla, J. Peacock, F. Pedicini, L. Pentericci, J. Pragt, M. Puech, S. Randich, A. Renzini, N. Ryde, M. Rodrigues, F. Royer, R. Saglia, A. Sánchez, H. Schnetler, D. Sobral, R. Speziali, S. Todd, E. Tolstoy, M. Torres, L. Venema, F. Vitali, M. Wegner, M. Wells, V. Wild, and G. Wright. MOONS: a multi-object optical and near-infrared spectrograph for the VLT. In *Society of Photo-Optical Instrumentation Engineers (SPIE) Conference Series*, volume 8446 of *Society of Photo-Optical Instrumentation Engineers (SPIE) Conference Series*, September 2012. doi: 10.1117/12.925871.

D. Clowe and P. Schneider. Wide field weak lensing observations of A1835 and A2204. *A&A*, 395:385–397, November 2002. doi: 10.1051/0004-6361:20021137.

D. Clowe, A. Gonzalez, and M. Markevitch. Weak-Lensing Mass Reconstruction of the Interacting Cluster 1E 0657-558: Direct Evidence for the Existence of Dark Matter. *ApJ*, 604:596–603, April 2004. doi: 10.1086/381970.

J. D. Cohn and M. White. Dark matter halo abundances, clustering and assembly histories at high redshift. *MNRAS*, 385:2025–2033, April 2008. doi: 10.1111/j.1365-2966.2008.12972.x.

P. Coles, A. L. Melott, and S. F. Shandarin. Testing approximations for non-linear gravitational clustering. *MNRAS*, 260:765–776, February 1993.

L. L. Cowie, A. Songaila, E. M. Hu, and J. G. Cohen. New Insight on Galaxy Formation and Evolution From Keck Spectroscopy of the Hawaii Deep Fields. *AJ*, 112:839, September 1996. doi: 10.1086/118058.

A. C. Crook, J. P. Huchra, N. Martimbeau, K. L. Masters, T. Jarrett, and L. M. Macri. Groups of Galaxies in the Two Micron All Sky Redshift Survey. *ApJ*, 655:790–813, February 2007. doi: 10.1086/510201.

J. H. Croston, M. Arnaud, E. Pointecouteau, and G. W. Pratt. An improved deprojection and PSF-deconvolution technique for galaxy-cluster X-ray surface-brightness profiles. *A&A*, 459:1007–1019, December 2006. doi: 10.1051/0004-6361:20065795.

H. H. Crowl, J. D. P. Kenney, J. H. van Gorkom, and B. Vollmer. Dense Cloud Ablation and Ram Pressure Stripping of the Virgo Spiral NGC 4402. *AJ*, 130:65–72, July 2005. doi: 10.1086/430526.

W. Cui, S. Borgani, K. Dolag, G. Murante, and L. Tornatore. The effects of baryons on the halo mass function. *MNRAS*, 423:2279–2287, July 2012. doi: 10.1111/j.1365-2966.2012.21037.x.

W. Cui, G. M. P. Monaco, S. Borgani, G. L. Granato, M. Killedar, G. De Lucia, V. Presotto, and K. Dolag. Characterizing Diffused Stellar Light in simulated galaxy clusters. *ArXiv e-prints*, October 2013.

C. Da Rocha, B. L. Ziegler, and C. Mendes de Oliveira. Intragroup diffuse light in compact groups of galaxies - II. HCG 15, 35 and 51. *MNRAS*, 388:1433–1443, August 2008. doi: 10.1111/j.1365-2966.2008.13500.x.

S. De Grandi and S. Molendi. Temperature Profiles of Nearby Clusters of Galaxies. *ApJ*, 567:163–177, March 2002. doi: 10.1086/338378.

W. Dehnen and D. E. McLaughlin. Dynamical insight into dark matter haloes. *MNRAS*, 363:1057–1068, November 2005. doi: 10.1111/j.1365-2966.2005.09510.x.

H. Dejonghe and D. Merritt. Inferring the mass of spherical stellar systems from velocity moments. *ApJ*, 391:531–549, June 1992. doi: 10.1086/171368.

R. den Hartog and P. Katgert. On the dynamics of the cores of galaxy clusters. *MNRAS*, 279:349–388, March 1996.

A. Diaferio. Mass estimation in the outer regions of galaxy clusters. *MNRAS*, 309: 610–622, November 1999. doi: 10.1046/j.1365-8711.1999.02864.x.

A. Diaferio and M. J. Geller. Infall Regions of Galaxy Clusters. *ApJ*, 481:633, May 1997. doi: 10.1086/304075.

J. Diemand, B. Moore, and J. Stadel. Velocity and spatial biases in cold dark matter subhalo distributions. *MNRAS*, 352:535–546, 2004.

K. Dolag, S. Borgani, G. Murante, and V. Springel. Substructures in hydrodynamical cluster simulations. *MNRAS*, 399:497–514, October 2009. doi: 10.1111/j.1365-2966.2009.15034.x.

A. Donnarumma, S. Ettori, M. Meneghetti, R. Gavazzi, B. Fort, L. Moscardini, A. Romano, L. Fu, F. Giordano, M. Radovich, R. Maoli, R. Scaramella, and J. Richard. Abell 611. II. X-ray and strong lensing analyses. *A&A*, 528:A73, April 2011. doi: 10.1051/0004-6361/201014120.

A. Dressler, A. Oemler, Jr., W. J. Couch, I. Smail, R. S. Ellis, A. Barger, H. Butcher, B. M. Poggianti, and R. M. Sharples. Evolution since Z = 0.5 of the Morphology-Density Relation for Clusters of Galaxies. *ApJ*, 490:577, December 1997. doi: 10.1086/304890.

P.-A. Duc and F. Bournaud. Tidal Debris from High-Velocity Collisions as Fake Dark Galaxies: A Numerical Model of VIRGOHI 21. *ApJ*, 673:787–797, February 2008. doi: 10.1086/524868.

A. R. Duffy, J. Schaye, S. T. Kay, and C. Dalla Vecchia. Dark matter halo concentrations in the wilkinson microwave anisotropy probe year 5 cosmology. *MNRAS*, 390:L64–L68, October 2008.

D. J. Eisenstein and W. Hu. Baryonic Features in the Matter Transfer Function. *ApJ*, 496:605, March 1998. doi: 10.1086/305424.

V. R. Eke, S. Cole, and C. S. Frenk. Cluster evolution as a diagnostic for Omega. *MNRAS*, 282:263–280, September 1996.

V. R. Eke, C. M. Baugh, S. Cole, C. S. Frenk, P. Norberg, J. A. Peacock, I. K. Baldry, J. Bland-Hawthorn, T. Bridges, R. Cannon, M. Colless, C. Collins, W. Couch, G. Dalton, R. de Propris, S. P. Driver, G. Efstathiou, R. S. Ellis, K. Glazebrook, C. Jackson, O. Lahav, I. Lewis, S. Lumsden, S. Maddox, D. Madgwick, B. A.

Peterson, W. Sutherland, and K. Taylor. Galaxy groups in the 2dFGRS: the group-finding algorithm and the 2PIGG catalogue. *MNRAS*, 348:866–878, March 2004. doi: 10.1111/j.1365-2966.2004.07408.x.

O. Esquivel and B. Fuchs. Dynamical friction force exerted on spherical bodies. *MNRAS*, 378:1191–1195, July 2007.

S. Ettori. The generalized scaling relations for X-ray galaxy clusters: the most powerful mass proxy. *MNRAS*, 435:1265–1277, October 2013. doi: 10.1093/mnras/stt1368.

S. Ettori, S. De Grandi, and S. Molendi. Gravitating mass profiles of nearby galaxy clusters and relations with X-ray gas temperature, luminosity and mass. *A&A*, 391:841–855, September 2002a. doi: 10.1051/0004-6361:20020905.

S. Ettori, A. C. Fabian, S. W. Allen, and R. M. Johnstone. Deep inside the core of Abell 1795: the Chandra view. *MNRAS*, 331:635–648, April 2002b. doi: 10.1046/j.1365-8711.2002.05212.x.

S. Ettori, F. Gastaldello, A. Leccardi, S. Molendi, M. Rossetti, D. Buote, and M. Meneghetti. Mass profiles and c-M_{DM} relation in X-ray luminous galaxy clusters. *A&A*, 524:A68, December 2010. doi: 10.1051/0004-6361/201015271.

S. Ettori, E. Rasia, D. Fabjan, S. Borgani, and K. Dolag. Pointing to the minimum scatter: the generalized scaling relations for galaxy clusters. *MNRAS*, 420:2058–2063, March 2012. doi: 10.1111/j.1365-2966.2011.20318.x.

A. E. Evrard, T. J. MacFarland, H. M. P. Couchman, J. M. Colberg, N. Yoshida, S. D. M. White, A. Jenkins, C. S. Frenk, F. R. Pearce, J. A. Peacock, and P. A. Thomas. Galaxy Clusters in Hubble Volume Simulations: Cosmological Constraints from Sky Survey Populations. *ApJ*, 573:7–36, July 2002. doi: 10.1086/340551.

A. E. Evrard, J. Bialek, M. Busha, M. White, S. Habib, K. Heitmann, M. Warren, E. Rasia, G. Tormen, L. Moscardini, C. Power, A. R. Jenkins, L. Gao, C. S. Frenk, V. Springel, S. D. M. White, and J. Diemand. Virial Scaling of Massive Dark Matter Halos: Why Clusters Prefer a High Normalization Cosmology. *ApJ*, 672:122–137, January 2008. doi: 10.1086/521616.

D. Fabjan, S. Borgani, L. Tornatore, A. Saro, G. Murante, and K. Dolag. Simulating the effect of active galactic nuclei feedback on the metal enrichment of galaxy

clusters. *MNRAS*, 401:1670–1690, January 2010. doi: 10.1111/j.1365-2966.2009.15794.x.

D. Fabjan, S. Borgani, E. Rasia, A. Bonafede, K. Dolag, G. Murante, and L. Tornatore. X-ray mass proxies from hydrodynamic simulations of galaxy clusters - I. *MNRAS*, 416:801–816, September 2011. doi: 10.1111/j.1365-2966.2011.18497.x.

A. Faltenbacher and J. Diemand. Velocity distributions in clusters of galaxies. *MNRAS*, 369:1698–1702, July 2006. doi: 10.1111/j.1365-2966.2006.10421.x.

A. Faltenbacher and W. G. Mathews. The concentration-velocity dispersion relation in galaxy groups. *MNRAS*, 375:313–323, February 2007. doi: 10.1111/j.1365-2966.2006.11295.x.

A. Faltenbacher and S. D. M. White. Assembly Bias and the Dynamical Structure of Dark Matter Halos. *ApJ*, 708:469–473, January 2010. doi: 10.1088/0004-637X/708/1/469.

A. Faltenbacher, A. V. Kravtsov, D. Nagai, and S. Gottlöber. Supersonic motions of galaxies in clusters. *MNRAS*, 358:139–148, March 2005.

G. J. Ferland, K. T. Korista, D. A. Verner, J. W. Ferguson, J. B. Kingdon, and E. M. Verner. CLOUDY 90: Numerical Simulation of Plasmas and Their Spectra. *PASP*, 110:761–778, July 1998. doi: 10.1086/316190.

F. Fontanot, G. De Lucia, P. Monaco, R. S. Somerville, and P. Santini. The many manifestations of downsizing: hierarchical galaxy formation models confront observations. *MNRAS*, 397:1776–1790, August 2009. doi: 10.1111/j.1365-2966.2009.15058.x.

Y. Fujita. Quantitative Estimates of Environmental Effects on the Star Formation Rate of Disk Galaxies in Clusters of Galaxies. *ApJ*, 509:587–594, December 1998. doi: 10.1086/306518.

L. Gao, J. F. Navarro, S. Cole, C. S. Frenk, S. D. M. White, V. Springel, A. Jenkins, and A. F. Neto. The redshift dependence of the structure of massive Λ cold dark matter haloes. *MNRAS*, 387:536–544, June 2008.

G. Gavazzi, D. Pierini, and A. Boselli. The phenomenology of disk galaxies. *A&A*, 312:397–408, August 1996.

K. Gebhardt, C. Pryor, T. B. Williams, and J. E. Hesser. Fabry-Perot measurements of the dynamics of globular cluster cores: M15 (NGC 7078). *AJ*, 107:2067–2076, June 1994. doi: 10.1086/117017.

M. J. Geller and J. P. Huchra. Groups of galaxies. III - The CfA survey. *ApJS*, 52: 61–87, June 1983. doi: 10.1086/190859.

M. J. Geller, A. Diaferio, and M. J. Kurtz. The Mass Profile of the Coma Galaxy Cluster. *ApJ*, 517:L23–L26, May 1999. doi: 10.1086/312024.

M. J. Geller, A. Diaferio, K. J. Rines, and A. L. Serra. Measuring the Mass Distribution in Galaxy Clusters. *ApJ*, 764:58, February 2013. doi: 10.1088/0004-637X/764/1/58.

S. P. D. Gill et al. The evolution of substructure – ii. linking dynamics to environment. *MNRAS*, 351(2):410–422, 2004.

S. Giodini, L. Lovisari, E. Pointecouteau, S. Ettori, T. H. Reiprich, and H. Hoekstra. Scaling Relations for Galaxy Clusters: Properties and Evolution. *Springer Space Science Reviews*, 177:247–282, August 2013. doi: 10.1007/s11214-013-9994-5.

M. Girardi, G. Giuricin, F. Mardirossian, M. Mezzetti, and W. Boschin. Optical Mass Estimates of Galaxy Clusters. *ApJ*, 505:74–95, September 1998. doi: 10.1086/306157.

M. D. Gladders and H. K. C. Yee. A New Method For Galaxy Cluster Detection. I. The Algorithm. *AJ*, 120:2148–2162, October 2000. doi: 10.1086/301557.

O. Y. Gnedin. Tidal Effects in Clusters of Galaxies. *ApJ*, 582:141–161, January 2003. doi: 10.1086/344636.

F. Governato, A. Babul, T. Quinn, P. Tozzi, C. M. Baugh, N. Katz, and G. Lake. Properties of galaxy clusters: mass and correlation functions. *MNRAS*, 307:949–966, August 1999. doi: 10.1046/j.1365-8711.1999.02706.x.

M. A. K. Gross, R. S. Somerville, J. R. Primack, J. Holtzman, and A. Klypin. Cold dark matter variant cosmological models - I. Simulations and preliminary comparisons. *MNRAS*, 301:81–94, November 1998. doi: 10.1046/j.1365-8711.1998.01998.x.

J. E. Gunn and J. R. Gott, III. On the Infall of Matter Into Clusters of Galaxies and Some Effects on Their Evolution. *ApJ*, 176:1, August 1972. doi: 10.1086/151605.

F. Haardt and P. Madau. Radiative Transfer in a Clumpy Universe. II. The Ultraviolet Extragalactic Background. *ApJ*, 461:20, April 1996. doi: 10.1086/177035.

F. Haardt and P. Madau. Modelling the UV/X-ray cosmic background with CUBA. In D. M. Neumann & J. T. V. Tran, editor, *Clusters of Galaxies and the High Redshift Universe Observed in X-rays*, 2001.

S. H. Hansen and B. Moore. A universal density slope Velocity anisotropy relation for relaxed structures. *New Astronomy*, 11:333–338, March 2006. doi: 10.1016/j.newast.2005.09.001.

E. R. Harrison and T. W. Noonan. Interpretation of extragalactic redshifts. *ApJ*, 232:18, August 1979. doi: 10.1086/157260.

J. P. Henry. X-Ray Temperatures for the Extended Medium-Sensitivity Survey High-Redshift Cluster Sample: Constraints on Cosmology and the Dark Energy Equation of State. *ApJ*, 609:603–616, July 2004. doi: 10.1086/421336.

L. Hernquist. An analytical model for spherical galaxies and bulges. *ApJ*, 356:359–364, June 1990. doi: 10.1086/168845.

A. K. Hicks, E. Ellingson, H. Hoekstra, and H. K. C. Yee. Multiwavelength Mass Comparisons of the z˜0.3 CNOC Cluster Sample. *ApJ*, 652:232–248, November 2006. doi: 10.1086/508138.

M. Hirschmann, K. Dolag, A. Saro, S. Borgani, and A. Burkert. Cosmological simulations of black hole growth: AGN luminosities and downsizing. *ArXiv e-prints*, August 2013.

H. Hoekstra. How well can we determine cluster mass profiles from weak lensing? *MNRAS*, 339:1155–1162, March 2003.

H. Hoekstra. Weak gravitational lensing. *ArXiv e-prints*, December 2013.

H. Hoekstra, M. Bartelmann, H. Dahle, H. Israel, M. Limousin, and M. Meneghetti. Masses of Galaxy Clusters from Gravitational Lensing. *Springer Space Science Reviews*, 177:75–118, August 2013. doi: 10.1007/s11214-013-9978-5.

J. P. Huchra and M. J. Geller. Groups of galaxies. I - Nearby groups. *ApJ*, 257:423–437, June 1982. doi: 10.1086/160000.

A. Jenkins, C. S. Frenk, S. D. M. White, J. M. Colberg, S. Cole, A. E. Evrard, H. M. P. Couchman, and N. Yoshida. The mass function of dark matter haloes. *MNRAS*, 321:372–384, February 2001. doi: 10.1046/j.1365-8711.2001.04029.x.

O. Johnson, P. Best, D. Zaritsky, D. Clowe, A. Aragón-Salamanca, C. Halliday, P. Jablonka, B. Milvang-Jensen, R. Pelló, B. M. Poggianti, G. Rudnick, R. Saglia, L. Simard, and S. White. The X-ray properties of optically selected z ¿ 0.6 clusters in the European Southern Observatory Distant Cluster Survey. *MNRAS*, 371: 1777–1792, October 2006. doi: 10.1111/j.1365-2966.2006.10796.x.

N. Kaiser. Evolution and clustering of rich clusters. *MNRAS*, 222:323–345, September 1986.

N. Kaiser and G. Squires. Mapping the dark matter with weak gravitational lensing. *ApJ*, 404:441–450, February 1993. doi: 10.1086/172297.

P. Katgert, A. Mazure, J. Perea, R. den Hartog, M. Moles, O. Le Fevre, P. Dubath, P. Focardi, G. Rhee, B. Jones, E. Escalera, A. Biviano, D. Gerbal, and G. Giuricin. The ESO Nearby Abell Cluster Survey. I. Description of the dataset and definition of physical systems. *A&A*, 310:8–30, June 1996.

P. Katgert, A. Mazure, R. den Hartog, C. Adami, A. Biviano, and J. Perea. The ESO Nearby Abell Cluster Survey. V. The catalogue: Contents and instructions for use. *A&AS*, 129:399–412, April 1998. doi: 10.1051/aas:1998399.

P. Katgert, A. Biviano, and A. Mazure. The eso nearby abell cluster survey. xii. the mass and mass-to-light ratio profiles of rich clusters. *ApJ*, 2004.

N. Katz, D. H. Weinberg, and L. Hernquist. Cosmological Simulations with TreeSPH. *ApJS*, 105:19, July 1996. doi: 10.1086/192305.

C. S. Kochanek, M. White, J. Huchra, L. Macri, T. H. Jarrett, S. E. Schneider, and J. Mader. Clusters of Galaxies in the Local Universe. *ApJ*, 585:161–181, March 2003. doi: 10.1086/345896.

B. P. Koester, T. A. McKay, J. Annis, R. H. Wechsler, A. Evrard, L. Bleem, M. Becker, D. Johnston, E. Sheldon, R. Nichol, C. Miller, R. Scranton, N. Bahcall, J. Barentine, H. Brewington, J. Brinkmann, M. Harvanek, S. Kleinman, J. Krzesinski, D. Long, A. Nitta, D. P. Schneider, S. Sneddin, W. Voges, and D. York. A MaxBCG Catalog of 13,823 Galaxy Clusters from the Sloan Digital Sky Survey. *ApJ*, 660:239–255, May 2007. doi: 10.1086/509599.

E. Komatsu, K. M. Smith, J. Dunkley, C. L. Bennett, B. Gold, G. Hinshaw, N. Jarosik, D. Larson, M. R. Nolta, L. Page, D. N. Spergel, M. Halpern, R. S. Hill, A. Kogut, M. Limon, S. S. Meyer, N. Odegard, G. S. Tucker, J. L. Weiland, E. Wollack, and E. L. Wright. Seven-year Wilkinson Microwave Anisotropy Probe (WMAP) Observations: Cosmological Interpretation. *ApJS*, 192:18, February 2011. doi: 10.1088/0067-0049/192/2/18.

A. V. Kravtsov and S. Borgani. Formation of Galaxy Clusters. *ARAA*, 50:353–409, September 2012. doi: 10.1146/annurev-astro-081811-125502.

A. V. Kravtsov, A. Vikhlinin, and D. Nagai. A New Robust Low-Scatter X-Ray Mass Indicator for Clusters of Galaxies. *ApJ*, 650:128–136, October 2006. doi: 10.1086/506319.

P. Kroupa. On the variation of the initial mass function. *MNRAS*, 322:231–246, April 2001. doi: 10.1046/j.1365-8711.2001.04022.x.

A. Lapi and A. Cavaliere. Dark matter equilibria in galaxies and galaxy systems. *ApJ*, 692(1):174, 2009.

A. Lapi and A. Cavaliere. Self-similar Dynamical Relaxation of Dark Matter Halos in an Expanding Universe. *ApJ*, 743:127, December 2011. doi: 10.1088/0004-637X/743/2/127.

E. T. Lau, D. Nagai, and A. V. Kravtsov. Effects of Baryon Dissipation on the Dark Matter Virial Scaling Relation. *ApJ*, 708:1419–1425, January 2010. doi: 10.1088/0004-637X/708/2/1419.

R. Laureijs, J. Amiaux, S. Arduini, J. . Augueres, J. Brinchmann, R. Cole, M. Cropper, C. Dabin, L. Duvet, A. Ealet, and et al. *Euclid Definition Study Report*. October 2011.

D. Lemze, R. Wagner, Y. Rephaeli, S. Sadeh, M. L. Norman, R. Barkana, T. Broadhurst, H. Ford, and M. Postman. Profiles of Dark Matter Velocity Anisotropy in Simulated Clusters. *ApJ*, 752:141, June 2012. doi: 10.1088/0004-637X/752/2/141.

A. Lewis and S. Bridle. Cosmological parameters from cmb and other data: A monte carlo approach. *Phys. Rev. D*, 66(10):103511, November 2002. doi: 10.1103/PhysRevD.66.103511.

M. Limousin, J. P. Kneib, S. Bardeau, P. Natarajan, O. Czoske, I. Smail, H. Ebeling, and G. P. Smith. Truncation of galaxy dark matter halos in high density environments. *A&A*, 461:881–891, January 2007.

M. Limousin, A. Morandi, M. Sereno, M. Meneghetti, S. Ettori, M. Bartelmann, and T. Verdugo. The Three-Dimensional Shapes of Galaxy Clusters. *Springer Space Science Reviews*, 177:155–194, August 2013. doi: 10.1007/s11214-013-9980-y.

Y.-T. Lin and J. J. Mohr. K-band Properties of Galaxy Clusters and Groups: Brightest Cluster Galaxies and Intracluster Light. *ApJ*, 617:879–895, December 2004. doi: 10.1086/425412.

C. Lobo, A. Biviano, F. Durret, D. Gerbal, O. Le Fevre, A. Mazure, and E. Slezak. Environmental effects on the Coma cluster luminosity function. *A&A*, 317:385–392, January 1997.

E. L. Łokas. Dark matter distribution in dwarf spheroidal galaxies. *MNRAS*, 333: 697–708, July 2002. doi: 10.1046/j.1365-8711.2002.05457.x.

E. L. Łokas and G. A. Mamon. Properties of spherical galaxies and clusters with an NFW density profile. *MNRAS*, 321:155–166, February 2001. doi: 10.1046/j.1365-8711.2001.04007.x.

E. L. Łokas and G. A. Mamon. Dark matter distribution in the Coma cluster from galaxy kinematics: breaking the mass-anisotropy degeneracy. *MNRAS*, 343:401–412, August 2003. doi: 10.1046/j.1365-8711.2003.06684.x.

A. D. Ludlow, J. F. Navarro, V. Springel, M. Vogelsberger, J. Wang, S. D. M. White, A. Jenkins, and C. S. Frenk. Secondary infall and the pseudo-phase-space density profiles of cold dark matter haloes. *MNRAS*, 406:137–146, July 2010. doi: 10.1111/j.1365-2966.2010.16678.x.

A. D. Ludlow, J. F. Navarro, S. D. M. White, M. Boylan-Kolchin, V. Springel, A. Jenkins, and C. S. Frenk. The density and pseudo-phase-space density profiles of cold dark matter haloes. *MNRAS*, 415:3895–3902, August 2011. doi: 10.1111/j.1365-2966.2011.19008.x.

A. D. Ludlow, J. F. Navarro, M. Boylan-Kolchin, P. E. Bett, R. E. Angulo, M. Li, S. D. M. White, C. Frenk, and V. Springel. The mass profile and accretion history of cold dark matter haloes. *MNRAS*, 432:1103–1113, June 2013. doi: 10.1093/mnras/stt526.

Z. Lukić, K. Heitmann, S. Habib, S. Bashinsky, and P. M. Ricker. The Halo Mass Function: High-Redshift Evolution and Universality. *ApJ*, 671:1160–1181, December 2007. doi: 10.1086/523083.

A. Maeder and G. Meynet. Grids of evolutionary models from 0.85 to 120 solar masses - Observational tests and the mass limits. *A&A*, 210:155–173, February 1989.

S. Mahajan, G. A. Mamon, and S. Raychaudhury. The velocity modulation of galaxy properties in and near clusters: quantifying the decrease in star formation in backsplash galaxies. *MNRAS*, 416:2882–2902, October 2011. doi: 10.1111/j.1365-2966.2011.19236.x.

A. Mahdavi, H. Hoekstra, A. Babul, C. Bildfell, T. Jeltema, and J. P. Henry. Joint Analysis of Cluster Observations. II. Chandra/XMM-Newton X-Ray and Weak Lensing Scaling Relations for a Sample of 50 Rich Clusters of Galaxies. *ApJ*, 767: 116, April 2013. doi: 10.1088/0004-637X/767/2/116.

M. A. G. Maia, L. N. da Costa, and D. W. Latham. A catalog of southern groups of galaxies. *ApJS*, 69:809–829, April 1989. doi: 10.1086/191328.

G. A. Mamon. Are cluster ellipticals the products of mergers? *ApJ*, 401:L3–L6, December 1992. doi: 10.1086/186656.

G. A. Mamon and E. L. Łokas. Dark matter in elliptical galaxies - II. Estimating the mass within the virial radius. *MNRAS*, 363:705–722, November 2005a. doi: 10.1111/j.1365-2966.2005.09400.x.

G. A. Mamon, E. Łokas, A. Dekel, F. Stoehr, and T. J. Cox. Kinematical and Dynamical Modeling of Elliptical Galaxies. In G. A. Mamon, F. Combes, C. Deffayet, and B. Fort, editors, *EAS Publications Series*, volume 20 of *EAS Publications Series*, pages 139–148, 2006. doi: 10.1051/eas:2006061. arXiv:astro-ph/0601345.

G. A. Mamon, A. Biviano, and G. Murante. The universal distribution of halo interlopers in projected phase space. Bias in galaxy cluster concentration and velocity anisotropy? *A&A*, 520:A30, October 2010.

G. A. Mamon, A. Biviano, and G. Boué. MAMPOSSt: Modelling Anisotropy and Mass Profiles of Observed Spherical Systems - I. Gaussian 3D velocities. *MNRAS*, 429:3079–3098, March 2013. doi: 10.1093/mnras/sts565.

Gary A. Mamon and Ewa L. Łokas. Dark matter in elliptical glaxies: Ii. estimating the mass within the virial radius. *MNRAS*, 363:705–722, November 2005b.

M. Markevitch. The L X-T Relation and Temperature Function for Nearby Clusters Revisited. *ApJ*, 504:27, September 1998. doi: 10.1086/306080.

M. Markevitch, T. J. Ponman, P. E. J. Nulsen, M. W. Bautz, D. J. Burke, L. P. David, D. Davis, R. H. Donnelly, W. R. Forman, C. Jones, J. Kaastra, E. Kellogg, D.-W. Kim, J. Kolodziejczak, P. Mazzotta, A. Pagliaro, S. Patel, L. Van Speybroeck, A. Vikhlinin, J. Vrtilek, M. Wise, and P. Zhao. Chandra Observation of Abell 2142: Survival of Dense Subcluster Cores in a Merger. *ApJ*, 541:542–549, October 2000. doi: 10.1086/309470.

D. P. Marrone, G. P. Smith, N. Okabe, M. Bonamente, J. E. Carlstrom, T. L. Culverhouse, M. Gralla, C. H. Greer, N. Hasler, D. Hawkins, R. Hennessy, M. Joy, J. W. Lamb, E. M. Leitch, R. Martino, P. Mazzotta, A. Miller, T. Mroczkowski, S. Muchovej, T. Plagge, C. Pryke, A. J. R. Sanderson, M. Takada, D. Woody, and Y. Zhang. LoCuSS: The Sunyaev-Zel'dovich Effect and Weak-lensing Mass Scaling Relation. *ApJ*, 754:119, August 2012. doi: 10.1088/0004-637X/754/2/119.

C. L. Martin. Properties of Galactic Outflows: Measurements of the Feedback from Star Formation. *ApJ*, 513:156–160, March 1999. doi: 10.1086/306863.

J.-C. Mauduit and G. A. Mamon. Suppressed radio emission in supercluster galaxies: enhanced ram pressure in merging clusters? *A&A*, 475:169–185, November 2007. doi: 10.1051/0004-6361:20077721.

J.-C. Mauduit and G. A. Mamon. Erratum: Suppressed radio emission in supercluster galaxies: enhanced ram pressure in merging clusters? *A&A*, 499:45–46, May 2009. doi: 10.1051/0004-6361/20077721e.

B. J. Maughan. The L_X-Y_X Relation: Using Galaxy Cluster X-Ray Luminosity as a Robust, Low-Scatter Mass Proxy. *ApJ*, 668:772–780, October 2007. doi: 10.1086/520831.

I. G. McCarthy, C. S. Frenk, A. S. Font, C. G. Lacey, R. G. Bower, N. L. Mitchell, M. L. Balogh, and T. Theuns. Ram pressure stripping the hot gaseous haloes of galaxies in groups and clusters. *MNRAS*, 383:593–605, January 2008. doi: 10.1111/j.1365-2966.2007.12577.x.

M. Meneghetti, E. Rasia, J. Merten, F. Bellagamba, S. Ettori, P. Mazzotta, K. Dolag, and S. Marri. Weighing simulated galaxy clusters using lensing and X-ray. *A&A*, 514:A93, May 2010. doi: 10.1051/0004-6361/200913222.

M. R. Merrifield and S. M. Kent. Fourth moments and the dynamics of spherical systems. *AJ*, 99:1548–1557, May 1990. doi: 10.1086/115438.

D. Merritt. Distribution functions for spherical galaxies. *MNRAS*, 214:25P–28P, June 1985.

A. I. Merson, C. M. Baugh, J. C. Helly, V. Gonzalez-Perez, S. Cole, R. Bielby, P. Norberg, C. S. Frenk, A. J. Benson, R. G. Bower, C. G. Lacey, and C. d. P. Lagos. Lightcone mock catalogues from semi-analytic models of galaxy formation - I. Construction and application to the BzK colour selection. *MNRAS*, 429:556–578, February 2013. doi: 10.1093/mnras/sts355.

H. Mo, F. van den Bosch, and S. White. *Galaxy Formation and Evolution*. Galaxy Formation and Evolution. Cambridge University Press, 2010. ISBN 9780521857932.

B. Moore, G. Lake, T. Quinn, and J. Stadel. On the survival and destruction of spiral galaxies in clusters. *MNRAS*, 304:465–474, April 1999. doi: 10.1046/j.1365-8711.1999.02345.x.

S. M. Moran, R. S. Ellis, T. Treu, G. P. Smith, R. M. Rich, and I. Smail. A Wide-Field Survey of Two z ˜ 0.5 Galaxy Clusters: Identifying the Physical Processes Responsible for the Observed Transformation of Spirals into S0s. *ApJ*, 671:1503–1522, December 2007. doi: 10.1086/522303.

A. Morandi, S. Ettori, and L. Moscardini. X-ray and Sunyaev-Zel'dovich scaling relations in galaxy clusters. *MNRAS*, 379:518–534, August 2007. doi: 10.1111/j.1365-2966.2007.11882.x.

M. J. Mortonson, W. Hu, and D. Huterer. Simultaneous falsification of ΛCDM and quintessence with massive, distant clusters. *Phys. Rev. D*, 83(2):023015, January 2011. doi: 10.1103/PhysRevD.83.023015.

C. Moss and R. J. Dickens. Redshifts of galaxies in the cluster Abell 262, and in the region of the Pisces group /centred on NGC 383/. *MNRAS*, 178:701–715, March 1977.

P. M. Motl, E. J. Hallman, J. O. Burns, and M. L. Norman. The Integrated Sunyaev-Zeldovich Effect as a Superior Method for Measuring the Mass of Clusters of Galaxies. *ApJ*, 623:L63–L66, April 2005. doi: 10.1086/430144.

J. C. Muñoz-Cuartas, A. V. Macciò, S. Gottlöber, and A. A. Dutton. The redshift evolution of Λ cold dark matter halo parameters: concentration, spin and shape. *MNRAS*, 411:584–594, February 2011. doi: 10.1111/j.1365-2966.2010.17704.x.

E. Munari, A. Biviano, S. Borgani, G. Murante, and D. Fabjan. The relation between velocity dispersion and mass in simulated clusters of galaxies: dependence on the tracer and the baryonic physics. *MNRAS*, 430:2638–2649, April 2013a. doi: 10.1093/mnras/stt049.

E. Munari, A. Biviano, and G. Mamon. Mass, velocity anisotropy and pseudo phase space density profiles of Abell 2142. *ArXiv e-prints*, November 2013b.

D. Nagai, A. Vikhlinin, and A. V. Kravtsov. Testing X-Ray Measurements of Galaxy Clusters with Cosmological Simulations. *ApJ*, 655:98–108, January 2007. doi: 10.1086/509868.

P. Natarajan, J.-P. Kneib, and I. Smail. Evidence for tidal stripping of dark matter halos in massive cluster lenses. *ApJ*, 580:L11–L15, November 2002.

J. F. Navarro, C. S. Frenk, and S. D. M. White. The structure of cold dark matter halos. *ApJ*, 462:563–575, May 1996.

J. F. Navarro, C. S. Frenk, and S. D. M. White. A Universal Density Profile from Hierarchical Clustering. *ApJ*, 490:493, December 1997. doi: 10.1086/304888.

J. F. Navarro, E. Hayashi, C. Power, A. R. Jenkins, C. S. Frenk, S. D. M. White, V. Springel, J. Stadel, and T. R. Quinn. The inner structure of ΛCDM haloes - III. Universality and asymptotic slopes. *MNRAS*, 349:1039–1051, April 2004. doi: 10.1111/j.1365-2966.2004.07586.x.

J. F. Navarro, A. Ludlow, V. Springel, J. Wang, M. Vogelsberger, S. D. M. White, A. Jenkins, C. S. Frenk, and A. Helmi. The diversity and similarity of simulated cold dark matter haloes. *MNRAS*, 402:21–34, February 2010. doi: 10.1111/j.1365-2966.2009.15878.x.

P. E. J. Nulsen, S. L. Powell, and A. Vikhlinin. Model-independent X-ray Mass Determinations. *ApJ*, 722:55–64, October 2010. doi: 10.1088/0004-637X/722/1/55.

N. Okabe and K. Umetsu. Subaru Weak Lensing Study of Seven Merging Clusters: Distributions of Mass and Baryons. *PASJ*, 60:345–, April 2008.

L. F. Olsen, M. Scodeggio, L. da Costa, C. Benoist, E. Bertin, E. Deul, T. Erben, M. D. Guarnieri, R. Hook, M. Nonino, I. Prandoni, R. Slijkhuis, A. Wicenec, and R. Wichmann. ESO imaging survey. II. Searching for distant clusters of galaxies. *A&A*, 345:681–690, May 1999.

L. P. Osipkov. Spherical systems of gravitating bodies with an ellipsoidal velocity distribution. *Soviet Astronomy Letters*, 5:42–44, 1979.

J. P. F. Osmond and T. J. Ponman. The GEMS project: X-ray analysis and statistical properties of the group sample. *MNRAS*, 350:1511–1535, June 2004. doi: 10.1111/j.1365-2966.2004.07742.x.

M. S. Owers, P. E. J. Nulsen, and W. J. Couch. Minor Merger-induced Cold Fronts in Abell 2142 and RXJ1720.1+2638. *ApJ*, 741:122, November 2011. doi: 10.1088/0004-637X/741/2/122.

P. Padovani and F. Matteucci. Stellar Mass Loss in Elliptical Galaxies and the Fueling of Active Galactic Nuclei. *ApJ*, 416:26, October 1993. doi: 10.1086/173212.

J.A. Peacock. *Cosmological Physics*. Cambridge Astrophysics Series. Cambridge University Press, 1999. ISBN 9780521422703.

K. A. Pimbblet, I. Smail, A. C. Edge, E. O'Hely, W. J. Couch, and A. I. Zabludoff. The Las Campanas/Anglo-Australian Telescope Rich Cluster Survey - III. Spectroscopic studies of X-ray bright galaxy clusters at z˜ 0.1. *MNRAS*, 366:645–666, February 2006. doi: 10.1111/j.1365-2966.2005.09892.x.

Planck collaboration, P. A. R. Ade, N. Aghanim, C. Armitage-Caplan, M. Arnaud, M. Ashdown, F. Atrio-Barandela, J. Aumont, C. Baccigalupi, A. J. Banday, and et al. Planck 2013 results. XV. CMB power spectra and likelihood. *ArXiv e-prints*, March 2013.

Planck Collaboration, P. A. R. Ade, N. Aghanim, C. Armitage-Caplan, M. Arnaud, M. Ashdown, F. Atrio-Barandela, J. Aumont, C. Baccigalupi, A. J. Banday, and et al. Planck 2013 results. XVI. Cosmological parameters. *ArXiv e-prints*, March 2013.

S. Planelles, S. Borgani, D. Fabjan, M. Killedar, G. Murante, G. L. Granato, C. Ragone-Figueroa, and K. Dolag. On the role of AGN feedback on the thermal and chemodynamical properties of the hot intra-cluster medium. *ArXiv e-prints*, November 2013.

E. Pointecouteau, M. Arnaud, and G. W. Pratt. The structural and scaling properties of nearby galaxy clusters. I. The universal mass profile. *A&A*, 435:1–7, May 2005. doi: 10.1051/0004-6361:20042569.

P. Popesso, A. Biviano, H. Böhringer, and M. Romaniello. RASS-SDSS galaxy cluster survey. V. The X-ray-underluminous Abell clusters. *A&A*, 461:397–410, January 2007. doi: 10.1051/0004-6361:20054493.

L. Portinari, C. Chiosi, and A. Bressan. Galactic chemical enrichment with new metallicity dependent stellar yields. *A&A*, 334:505–539, June 1998.

M. Postman and M. J. Geller. The morphology-density relation - The group connection. *ApJ*, 281:95–99, June 1984. doi: 10.1086/162078.

M. Postman, L. M. Lubin, J. E. Gunn, J. B. Oke, J. G. Hoessel, D. P. Schneider, and J. A. Christensen. The Palomar Distant Clusters Survey. I. The Cluster Catalog. *AJ*, 111:615, February 1996. doi: 10.1086/117811.

M. Postman, M. Franx, N. J. G. Cross, B. Holden, H. C. Ford, G. D. Illingworth, T. Goto, R. Demarco, P. Rosati, J. P. Blakeslee, K.-V. Tran, N. Benítez, M. Clampin, G. F. Hartig, N. Homeier, D. R. Ardila, F. Bartko, R. J. Bouwens, L. D. Bradley, T. J. Broadhurst, R. A. Brown, C. J. Burrows, E. S. Cheng, P. D. Feldman, D. A. Golimowski, C. Gronwall, L. Infante, R. A. Kimble, J. E. Krist, M. P. Lesser, A. R. Martel, S. Mei, F. Menanteau, G. R. Meurer, G. K. Miley, V. Motta, M. Sirianni, W. B. Sparks, H. D. Tran, Z. I. Tsvetanov, R. L. White, and W. Zheng. The Morphology-Density Relation in z ˜ 1 Clusters. *ApJ*, 623:721–741, April 2005. doi: 10.1086/428881.

M. Postman, D. Coe, N. Benítez, L. Bradley, T. Broadhurst, M. Donahue, H. Ford, O. Graur, G. Graves, S. Jouvel, A. Koekemoer, D. Lemze, E. Medezinski, A. Molino, L. Moustakas, S. Ogaz, A. Riess, S. Rodney, P. Rosati, K. Umetsu, W. Zheng, A. Zitrin, M. Bartelmann, R. Bouwens, N. Czakon, S. Golwala, O. Host, L. Infante, S. Jha, Y. Jimenez-Teja, D. Kelson, O. Lahav, R. Lazkoz, D. Maoz, C. McCully, P. Melchior, M. Meneghetti, J. Merten, J. Moustakas, M. Nonino, B. Patel, E. Regös, J. Sayers, S. Seitz, and A. Van der Wel. The Cluster Lensing

and Supernova Survey with Hubble: An Overview. *ApJS*, 199:25, April 2012. doi: 10.1088/0067-0049/199/2/25.

G. W. Pratt, J. H. Croston, M. Arnaud, and H. Böhringer. Galaxy cluster X-ray luminosity scaling relations from a representative local sample (REXCESS). *A&A*, 498:361–378, May 2009. doi: 10.1051/0004-6361/200810994.

W. H. Press and P. Schechter. Formation of Galaxies and Clusters of Galaxies by Self-Similar Gravitational Condensation. *ApJ*, 187:425–438, February 1974. doi: 10.1086/152650.

M. Ramella, G. Zamorani, E. Zucca, G. M. Stirpe, G. Vettolani, C. Balkowski, A. Blanchard, A. Cappi, V. Cayatte, G. Chincarini, C. Collins, L. Guzzo, H. MacGillivray, D. Maccagni, S. Maurogordato, R. Merighi, M. Mignoli, A. Pisani, D. Proust, and R. Scaramella. The ESO slice project (ESP) galaxy redshift survey VI. Groups of galaxies. *A&A*, 342:1–14, February 1999.

M. Ramella, W. Boschin, D. Fadda, and M. Nonino. Finding galaxy clusters using Voronoi tessellations. *A&A*, 368:776–786, March 2001. doi: 10.1051/0004-6361:20010071.

M. Ramella, A. Biviano, A. Pisani, J. Varela, D. Bettoni, W. J. Couch, M. D'Onofrio, A. Dressler, G. Fasano, P. Kjørgaard, M. Moles, E. Pignatelli, and B. M. Poggianti. Substructures in WINGS clusters. *A&A*, 470:39–51, July 2007. doi: 10.1051/0004-6361:20077245.

E. Rasia, S. Ettori, L. Moscardini, P. Mazzotta, S. Borgani, K. Dolag, G. Tormen, L. M. Cheng, and A. Diaferio. Systematics in the X-ray cluster mass estimators. *MNRAS*, 369:2013–2024, July 2006. doi: 10.1111/j.1365-2966.2006.10466.x.

E. Rasia, P. Mazzotta, A. Evrard, M. Markevitch, K. Dolag, and M. Meneghetti. Scaling Relation in Two Situations of Extreme Mergers. *ApJ*, 729:45, March 2011. doi: 10.1088/0004-637X/729/1/45.

E. Rasia, M. Meneghetti, R. Martino, S. Borgani, A. Bonafede, K. Dolag, S. Ettori, D. Fabjan, C. Giocoli, P. Mazzotta, J. Merten, M. Radovich, and L. Tornatore. Lensing and x-ray mass estimates of clusters (simulations). *New Journal of Physics*, 14(5):055018, May 2012. doi: 10.1088/1367-2630/14/5/055018.

D. Reed, J. Gardner, T. Quinn, J. Stadel, M. Fardal, G. Lake, and F. Governato. Evolution of the mass function of dark matter haloes. *MNRAS*, 346:565–572, December 2003. doi: 10.1046/j.1365-2966.2003.07113.x.

D. S. Reed, R. Bower, C. S. Frenk, A. Jenkins, and T. Theuns. The halo mass function from the dark ages through the present day. *MNRAS*, 374:2–15, January 2007. doi: 10.1111/j.1365-2966.2006.11204.x.

T. H. Reiprich and H. Böhringer. The Mass Function of an X-Ray Flux-limited Sample of Galaxy Clusters. *ApJ*, 567:716–740, March 2002. doi: 10.1086/338753.

A. L. B. Ribeiro, P. A. A. Lopes, and M. Trevisan. Non-Gaussian velocity distributions - the effect on virial mass estimates of galaxy groups. *MNRAS*, 413:L81–L85, May 2011. doi: 10.1111/j.1745-3933.2011.01038.x.

K. Rines, M. J. Geller, and A. Diaferio. Comparison of Hectospec Virial Masses with Sunyaev-Zel'Dovich Effect Measurements. *ApJ*, 715:L180–L184, June 2010. doi: 10.1088/2041-8205/715/2/L180.

P. Rosati, S. Borgani, and C. Norman. The Evolution of X-ray Clusters of Galaxies. *ARAA*, 40:539–577, 2002. doi: 10.1146/annurev.astro.40.120401.150547.

M. Rossetti, D. Eckert, S. De Grandi, F. Gastaldello, S. Ghizzardi, E. Roediger, and S. Molendi. Abell 2142 at large scales: An extreme case for sloshing? *A&A*, May 2013. in press, arXiv:1305.2420.

E. E. Salpeter. The Luminosity Function and Stellar Evolution. *ApJ*, 121:161, January 1955. doi: 10.1086/145971.

C. L. Sarazin. *X-ray emission from clusters of galaxies*. 1988.

A. Saro, G. Bazin, J. Mohr, and K. Dolag. Toward Unbiased Galaxy Cluster Masses from Line of Sight Velocity Dispersions. *ArXiv e-prints*, March 2012.

B. Sartoris. *Study of structure formation and evolution in non-standard cosmological models*. PhD thesis, Universitá degli Studi di Trieste, 2012.

E. Scannapieco, J. Silk, and R. Bouwens. AGN Feedback Causes Downsizing. *ApJ*, 635:L13–L16, December 2005. doi: 10.1086/499271.

P. Schechter. An analytic expression for the luminosity function for galaxies. *ApJ*, 203:297–306, January 1976. doi: 10.1086/154079.

C. Seitz and P. Schneider. Steps towards nonlinear cluster inversion through gravitational distortions II. Generalization of the Kaiser and Squires method. *A&A*, 297:287, May 1995.

A. L. Serra and A. Diaferio. Identification of Members in the Central and Outer Regions of Galaxy Clusters. *ApJ*, 768:116, May 2013. doi: 10.1088/0004-637X/768/2/116.

A. L. Serra, A. Diaferio, G. Murante, and S. Borgani. Measuring the escape velocity and mass profiles of galaxy clusters beyond their virial radius. *MNRAS*, 412: 800–816, April 2011. doi: 10.1111/j.1365-2966.2010.17946.x.

R. K. Sheth and G. Tormen. Large-scale bias and the peak background split. *MNRAS*, 308:119–126, September 1999. doi: 10.1046/j.1365-8711.1999.02692.x.

R. K. Sheth, H. J. Mo, and G. Tormen. Ellipsoidal collapse and an improved model for the number and spatial distribution of dark matter haloes. *MNRAS*, 323:1–12, May 2001. doi: 10.1046/j.1365-8711.2001.04006.x.

D. Sijacki, V. Springel, T. Di Matteo, and L. Hernquist. A unified model for AGN feedback in cosmological simulations of structure formation. *MNRAS*, 380:877–900, September 2007. doi: 10.1111/j.1365-2966.2007.12153.x.

I. Smail, A. C. Edge, R. S. Ellis, and R. D. Blandford. A statistical analysis of the galaxy populations of distant luminous X-ray clusters. *MNRAS*, 293:124, January 1998. doi: 10.1046/j.1365-8711.1998.2932124.x.

G. P. Smith, J.-P. Kneib, I. Smail, P. Mazzotta, H. Ebeling, and O. Czoske. A Hubble Space Telescope lensing survey of X-ray luminous galaxy clusters - IV. Mass, structure and thermodynamics of cluster cores at z= 0.2. *MNRAS*, 359:417–446, May 2005a. doi: 10.1111/j.1365-2966.2005.08911.x.

G. P. Smith, T. Treu, R. S. Ellis, S. M. Moran, and A. Dressler. Evolution since z = 1 of the Morphology-Density Relation for Galaxies. *ApJ*, 620:78–87, February 2005b. doi: 10.1086/426930.

J. M. Solanes and E. Salvador-Sole. Analytical anisotropic models of clusters of galaxies. *A&A*, 234:93–98, August 1990.

V. Springel. The cosmological simulation code GADGET-2. *MNRAS*, 364:1105–1134, December 2005. doi: 10.1111/j.1365-2966.2005.09655.x.

V. Springel and L. Hernquist. The history of star formation in a Λ cold dark matter universe. *MNRAS*, 339:312–334, February 2003. doi: 10.1046/j.1365-8711.2003.06207.x.

V. Springel, N. Yoshida, and S. D. M. White. Gadget: a code for collisionless and gasdynamical cosmological simulations. *New Astronomy*, 6:79–117, 2001.

V. Springel, T. Di Matteo, and L. Hernquist. Modelling feedback from stars and black holes in galaxy mergers. *MNRAS*, 361:776–794, August 2005a. doi: 10.1111/j.1365-2966.2005.09238.x.

V. Springel, S. D. M. White, A. Jenkins, C. S. Frenk, N. Yoshida, L. Gao, J. Navarro, R. Thacker, D. Croton, J. Helly, J. A. Peacock, S. Cole, P. Thomas, H. Couchman, A. Evrard, J. Colberg, and F. Pearce. Simulations of the formation, evolution and clustering of galaxies and quasars. *Nature*, 435:629–636, June 2005b. doi: 10.1038/nature03597.

R. Stanek, D. Rudd, and A. E. Evrard. The effect of gas physics on the halo mass function. *MNRAS*, 394:L11–L15, March 2009. doi: 10.1111/j.1745-3933.2008.00597.x.

V. Strazzullo, R. Gobat, E. Daddi, M. Onodera, M. Carollo, M. Dickinson, A. Renzini, N. Arimoto, A. Cimatti, A. Finoguenov, and R.-R. Chary. Galaxy Evolution in Overdense Environments at High Redshift: Passive Early-type Galaxies in a Cluster at z ˜ 2. *ApJ*, 772:118, August 2013. doi: 10.1088/0004-637X/772/2/118.

M. F. Struble. Alignment statistics of clusters with their brightest members at bright and faint isophotes. *ApJ*, 317:668–671, June 1987. doi: 10.1086/165311.

R. S. Sutherland and M. A. Dopita. Cooling functions for low-density astrophysical plasmas. *ApJS*, 88:253–327, September 1993. doi: 10.1086/191823.

J. E. Taylor and J. F. Navarro. The Phase-Space Density Profiles of Cold Dark Matter Halos. *ApJ*, 563:483–488, December 2001. doi: 10.1086/324031.

J. Tinker, A. V. Kravtsov, A. Klypin, K. Abazajian, M. Warren, G. Yepes, S. Gottlöber, and D. E. Holz. Toward a Halo Mass Function for Precision Cosmology: The Limits of Universality. *ApJ*, 688:709–728, December 2008. doi: 10.1086/591439.

O. Tiret, F. Combes, G. W. Angus, B. Famaey, and H. S. Zhao. Velocity dispersion around ellipticals in MOND. *A&A*, 476:L1–L4, December 2007. doi: 10.1051/0004-6361:20078569.

G. Tormen, F. R. Bouchet, and S. D. M. White. The structure and dynamical evolution of dark matter haloes. *MNRAS*, 286:865–884, April 1997.

L. Tornatore, S. Borgani, K. Dolag, and F. Matteucci. Chemical enrichment of galaxy clusters from hydrodynamical simulations. *MNRAS*, 382:1050–1072, December 2007. doi: 10.1111/j.1365-2966.2007.12070.x.

T. Treu, R. S. Ellis, T. X. Liao, and P. G. van Dokkum. Keck Spectroscopy of Distant GOODS Spheroidal Galaxies: Downsizing in a Hierarchical Universe. *ApJ*, 622: L5–L8, March 2005. doi: 10.1086/429374.

D. L. Tucker, A. Oemler, Jr., Y. Hashimoto, S. A. Shectman, R. P. Kirshner, H. Lin, S. D. Landy, P. L. Schechter, and S. S. Allam. Loose Groups of Galaxies in the Las Campanas Redshift Survey. *ApJS*, 130:237–265, October 2000. doi: 10.1086/317348.

K. Umetsu, M. Birkinshaw, G.-C. Liu, J.-H. P. Wu, E. Medezinski, T. Broadhurst, D. Lemze, A. Zitrin, P. T. P. Ho, C.-W. L. Huang, P. M. Koch, Y.-W. Liao, K.-Y. Lin, S. M. Molnar, H. Nishioka, F.-C. Wang, P. Altamirano, C.-H. Chang, S.-H. Chang, S.-W. Chang, M.-T. Chen, C.-C. Han, Y.-D. Huang, Y.-J. Hwang, H. Jiang, M. Kesteven, D. Y. Kubo, C.-T. Li, P. Martin-Cocher, P. Oshiro, P. Raffin, T. Wei, and W. Wilson. Mass and Hot Baryons in Massive Galaxy Clusters from Subaru Weak-Lensing and AMiBA Sunyaev-Zel'Dovich Effect Observations. *ApJ*, 694: 1643–1663, April 2009. doi: 10.1088/0004-637X/694/2/1643.

K. Umetsu, E. Medezinski, M. Nonino, J. Merten, A. Zitrin, A. Molino, C. Grillo, M. Carrasco, M. Donahue, A. Mahdavi, D. Coe, M. Postman, A. Koekemoer, N. Czakon, J. Sayers, T. Mroczkowski, S. Golwala, P. M. Koch, K.-Y. Lin, S. M. Molnar, P. Rosati, I. Balestra, A. Mercurio, M. Scodeggio, A. Biviano, T. Anguita, L. Infante, G. Seidel, I. Sendra, S. Jouvel, O. Host, D. Lemze, T. Broadhurst, M. Meneghetti, L. Moustakas, M. Bartelmann, N. Benítez, R. Bouwens, L. Bradley, H. Ford, Y. Jiménez-Teja, D. Kelson, O. Lahav, P. Melchior, J. Moustakas, S. Ogaz, S. Seitz, and W. Zheng. CLASH: Mass Distribution in and around MACS J1206.2-0847 from a Full Cluster Lensing Analysis. *ApJ*, 755:56, August 2012. doi: 10.1088/0004-637X/755/1/56.

F. C. van den Bosch. The universal mass accretion history of cold dark matter haloes. *MNRAS*, 331:98–110, March 2002.

R. P. van der Marel, J. Magorrian, R. G. Carlberg, H. K. C. Yee, and E. Ellingson. The velocity and mass distribution of clusters of galaxies from the cnoc1 cluster redshift survey. *AJ*, 119:2038–2052, May 2000. doi: 10.1086/301351.

E. van Uitert, H. Hoekstra, T. Schrabback, D. G. Gilbank, M. D. Gladders, and H. K. C. Yee. Constraints on the shapes of galaxy dark matter haloes from weak gravitational lensing. *A&A*, 545:A71, September 2012. doi: 10.1051/0004-6361/201219295.

M. Vogelsberger, R. Mohayaee, and S. D. M. White. Non-spherical similarity solutions for dark halo formation. *MNRAS*, 414:3044–3051, July 2011. doi: 10.1111/j.1365-2966.2011.18605.x.

L. M. Voigt and A. C. Fabian. Galaxy cluster mass profiles. *MNRAS*, 368:518–533, May 2006. doi: 10.1111/j.1365-2966.2006.10199.x.

H. Y. Wang, Y. P. Jing, S. Mao, and X. Kang. The phase-space distribution of infalling dark matter subhaloes. *MNRAS*, 364:424–432, December 2005. doi: 10.1111/j.1365-2966.2005.09543.x.

J. Wang and S. D. M. White. Are mergers responsible for universal halo properties? *MNRAS*, 396:709–717, June 2009. doi: 10.1111/j.1365-2966.2009.14755.x.

M. S. Warren, K. Abazajian, D. E. Holz, and L. Teodoro. Precision Determination of the Mass Function of Dark Matter Halos. *ApJ*, 646:881–885, August 2006. doi: 10.1086/504962.

D. H. Weinberg, S. Colombi, R. Davé, and N. Katz. Baryon Dynamics, Dark Matter Substructure, and Galaxies. *ApJ*, 678:6–21, May 2008. doi: 10.1086/524646.

A. R. Wetzel. On the orbits of infalling satellite haloes. *MNRAS*, 412:49–58, March 2011. doi: 10.1111/j.1365-2966.2010.17877.x.

A. R. Wetzel and M. White. What determines satellite galaxy disruption? *MNRAS*, 403:1072–1088, April 2010. doi: 10.1111/j.1365-2966.2009.16191.x.

M. White et al. The clustering of massive galaxies at z ˜ 0.5 from the first semester of boss data. *ApJ*, 728:126, February 2011.

S. D. M. White. Dynamical friction in spherical clusters. *MNRAS*, 174:19–28, January 1976.

B. C. Whitmore, D. M. Gilmore, and C. Jones. What determines the morphological fractions in clusters of galaxies? *ApJ*, 407:489–509, April 1993. doi: 10.1086/172531.

R. P. C. Wiersma, J. Schaye, and B. D. Smith. The effect of photoionization on the cooling rates of enriched, astrophysical plasmas. *MNRAS*, 393:99–107, February 2009. doi: 10.1111/j.1365-2966.2008.14191.x.

M. J. Williams, M. Bureau, and M. Cappellari. The Tully-Fisher relations of early-type spiral and S0 galaxies. *MNRAS*, 409:1330–1346, December 2010. doi: 10.1111/j.1365-2966.2010.17406.x.

R. Wojtak and E. L. Łokas. Mass profiles and galaxy orbits in nearby galaxy clusters from the analysis of the projected phase space. *MNRAS*, 408:2442–2456, November 2010. doi: 10.1111/j.1365-2966.2010.17297.x.

R. Wojtak, E. L. Łokas, G. A. Mamon, S. Gottlöber, A. Klypin, and Y. Hoffman. The distribution function of dark matter in massive haloes. *MNRAS*, 388:815–828, August 2008. doi: 10.1111/j.1365-2966.2008.13441.x.

R. Wojtak, S. Gottlöber, and A. Klypin. Orbital anisotropy in cosmological haloes revisited. *MNRAS*, 434:1576–1585, September 2013. doi: 10.1093/mnras/stt1113.

S.-J. Xue, Y.-H. Zhang, and J.-S. Chen. ROSAT/ASCA Observations of a Serendipitous BL Lacertae Object PKS 2316-423: The Variable High-Energy Tail of Synchrotron Radiation. *ApJ*, 538:121–126, July 2000. doi: 10.1086/309111.

Y. B. Zel'dovich. Fragmentation of a homogeneous medium under the action of gravitation. *Astrophysics*, 6:164–174, April 1970. doi: 10.1007/BF01007263.

Y.-Y. Zhang, N. Okabe, A. Finoguenov, G. P. Smith, R. Piffaretti, R. Valdarnini, A. Babul, A. E. Evrard, P. Mazzotta, A. J. R. Sanderson, and D. P. Marrone. LoCuSS: A Comparison of Cluster Mass Measurements from XMM-Newton and Subaru: Testing Deviation from Hydrostatic Equilibrium and Non-thermal Pressure Support. *ApJ*, 711:1033–1043, March 2010. doi: 10.1088/0004-637X/711/2/1033.

F. Zwicky. Die Rotverschiebung von extragalaktischen Nebeln. *Helvetica Physica Acta*, 6:110–127, 1933.

Tu prova ad avere un mondo nel cuore
e non riesci ad esprimerlo con le parole

Fabrizio De André